Time Domain Surface Integral Equation Solvers for Quantum Corrected Electromagnetic Analysis of Plasmonic Nanostructures

Dissertation by

İsmail Enes Uysal

In Partial Fulfillment of the Requirements

For the Degree of

Doctor of Philosophy

King Abdullah University of Science and Technology

Thuwal, Kingdom of Saudi Arabia

October, 2016

EXAMINATION COMMITTEE PAGE

The dissertation of İsmail Enes Uysal is approved by the examination committee

Committee Chairperson: Hakan Bağcı
Committee Members: Boon Ooi, Udo Schwingenschlögl, Shanker Balasubramaniam

ABSTRACT

Time Domain Surface Integral Equation Solvers for Quantum Corrected Electromagnetic Analysis of Plasmonic Nanostructures

İsmail Enes Uysal

Plasmonic structures are utilized in many applications ranging from bio-medicine to solar energy generation and transfer. Numerical schemes capable of solving equations of classical electrodynamics have been the method of choice for characterizing scattering properties of such structures. However, as dimensions of these plasmonic structures reduce to nanometer scale, quantum mechanical effects start to appear. These effects cannot be accurately modeled by available classical numerical methods. One of these quantum effects is the tunneling, which is observed when two structures are located within a sub-nanometer distance of each other. At these small distances electrons "jump" from one structure to another and introduce a path for electric current to flow. Classical equations of electrodynamics and the schemes used for solving them do not account for this additional current path. This limitation can be lifted by introducing an auxiliary tunnel with material properties obtained using quantum models and applying a classical solver to the structures connected by this auxiliary tunnel. Early work on this topic focused on quantum models that are generated using a simple one-dimensional wave function to find the tunneling probability and assume a simple Drude model for the permittivity of the tunnel. These tunnel models are then used together with a classical frequency domain solver.

In this thesis, a time domain surface integral equation solver for quantum corrected analysis of transient plasmonic interactions is proposed. This solver has several advantages: (i) As opposed to frequency domain solvers, it provides results at

a broad band of frequencies with a single simulation. (ii) As opposed to differential equation solvers, it only discretizes surfaces (reducing number of unknowns), enforces the radiation condition implicitly (increasing the accuracy), and allows for time step selection independent of spatial discretization (increasing efficiency). The quantum model of the tunnel is obtained using density functional theory (DFT) computations, which account for the atomic structure of materials. Accuracy and applicability of this (quantum corrected) time domain surface integral equation solver will be shown by numerical examples.

TABLE OF CONTENTS

LIST OF FIGURES

Chapter 1

Introduction

1.1 Introduction

Plasmonic nanostructures are indispensible components of electromagnetic and optical systems developed for many applications ranging from bio-medicine to solar energy generation and transportation [1–3]. The proper operation of these systems/devices relies on generation of highly-localized electromagnetic fields induced on the boundary between the plasmonic nanostructure (typically made of metals) and the surrounding dielectric medium. The characteristics of these plasmonic fields depend on the shape of the nanostructure, the type of the metal it is made of, and dielectric permittivity of the surrounding medium [1]. Consequently, to be able to generate the desired field characteristics, tools capable of characterizing plasmonic interactions on arbitrarily shaped structures are called for [1, 4]. This device characterization required by design frameworks can be done experimentally or numerically. Numerical characterization has several advantages over its experimental counterpart: (i) After the initial code development, it requires less human effort to carry out the characterization process. (ii) Cost of experiments is typically higher than cost of running simulations on computers/clusters. Also, it should be noted here that a typical design process does not rely on only experiments or only numerical simulations. Oftentimes they complement each other, where experiments follow numerical simulations, which provide an initial insight to the physical mechanisms behind the operation of the device being designed.

Existing numerical schemes, which are developed for characterizing plasmonic interactions, solve Maxwell equations with classical boundary conditions and constitutive relations [4]. However, as the dimensions of the structures reduce to few nanometers or below, quantum mechanical effects start to appear rendering the solution of Maxwell equations with classical constitutive relations inaccurate. This is due to the fact that, at the atomic level, approximation of a structure by a simple geometry with sharp boundaries/surfaces and localized material properties is not accurate. One of the most prominent quantum effects is the tunneling, which is observed when two structures are located within a sub-nanometer distance of each other. At these small distances electrons "jump" from one structure to the other and introduce an additional path for the electric current to flow. Classical constitutive relations do not account for this additional current path. To overcome this problem, one can employ a full quantum mechanical modeling approach, such as the time dependent density functional theory [5], on the whole geometry, but oftentimes this is not possible because of the high computational cost. Hybrid methods lower the computational cost by utilizing quantum mechanical modeling only on the tunnel while solving classical equations of electrodynamics on the rest of the structure [6]. This hybrid approach first finds the tunneling probability of an electron between two nanostructures by solving a one-dimensional (1D) quantum problem; then the tunneling probability is used to calculate the effective conductivity and permittivity of a fictitious material that would act as the tunnel between the two nanostructures. At the final stage, the nanostructures and the auxiliary tunnel are characterized together as one structure by solving Maxwell equations with classical constitutive relations.

The work presented in this thesis uses a similar approach for numerical characterization of plasmonic nanostructures with quantum tunneling effects. The novelty of this work is two fold: (i) It uses a time domain surface integral equation (TD-SIE) solver [7] to analyze classical plasmonic interactions on nanostructures, and (ii)

the material properties of the auxiliary tunnel accounting for the quantum effects is obtained using the density functional theory computations [8, 9]. The following two sections of this chapter discuss the advantages/disadvantages of these two approaches and compare them (qualitatively) to the several methods existing in literature.

1.2 Numerical Methods for Analyzing Plasmonic Interactions

Numerical schemes developed for analyzing plasmonic field interactions can be grouped into two: differential and integral equation solvers [4]. Differential equation solvers, which include, finite difference time domain (FDTD) scheme and finite element method (FEM), directly solve Maxwell equations in time or frequency domain. FDTD is easier to implement but oftentimes its accuracy is limited by the zeroth or the first order approximations used in the discretization of the derivatives [10], which results in significant numerical dispersion errors especially for electrically large structures [11]. Additionally, structures are discretized using cubic/rectangular elements reducing the accuracy of geometry representation [10]. FEM does not suffer from these drawbacks but like FDTD, it requires truncation of unbounded physical domain (where the structures reside) into a bounded computation domain using approximate absorbing boundary conditions [12], which reduces the accuracy of the solution especially in time domain under resonance conditions [13]. More importantly, both FDTD and FEM require volumetric discretization of the structures. To accurately capture the exponentially decaying behavior of plasmonic fields in the vicinity of the metal/dielectric interfaces, the density of these volumetric discretization has to be significantly increased. This leads to an increased number of degrees of freedom to be solved for and consequently increases the computational cost.

The bottlenecks described above can be avoided by utilizing surface integral equation solvers. These numerical schemes use electromagnetic equivalence principle to

convert (differential) Maxwell equations into surface integral equations enforced on interfaces where the material properties have discontinuities [14]. This approach has two fundamental advantages: (i) Equivalence principle allows for representation of three-dimensional (3D) volumetric scatterers in terms of currents defined on two-dimensional (2D) surfaces enclosing the scatterers. This means that the dimension of the space to be discretized is reduced to two from three decreasing computational cost significantly especially in the presence of plasmonic fields. (ii) Fields generated by the equivalent currents are represented in terms of the Green functions of the unbounded media with material properties of the scatterers and the background. Use of Green function implicitly enforces the radiation condition and removes the need for approximate domain truncation techniques called for by FDTD and FEM schemes. Also, it eliminates the errors due to numerical phase dispersion.

Indeed, thanks to the advantages listed above, use of surface integral equation (SIE) solvers for analyzing plasmonic field interactions on arbitrarily shaped structures has recently increased [15–19]. But these solvers have been developed for only frequency domain (FD), where sources and induced currents and fields are assumed to be time harmonic. This results in two limitations: (i) FD-SIE solvers cannot be applied in scattering problems where the material properties are functions of field values, e.g., Kerr-nonlinear materials [20]. (ii) FD-SIE solver has to be executed many times at different frequencies to obtain broadband results or compute transient field interactions (after application of an inverse Fourier transform) [21]. These limitations can be overcome through the use of time domain surface integral equation (TD-SIE) solvers. Indeed, one of the goals of the work described in this thesis is to formulate and implement a TD-SIE solver for efficiently and accurately analyzing transient plasmonic field interactions on nanostructures.

1.3 Time Domain Surface Integral Equation Solvers for Analyzing Plasmonic Field Interactions

TD-SIE solvers have long been used for analyzing electromagnetic field interactions on perfect electrically conducting (PEC) scatterers and dielectric objects with non-dispersive material properties [22–25]. However, despite their advantages, TD-SIE solvers have not been used for analyzing scattering from objects with dispersive material properties, with only one exception [26], which makes use of finite difference delay modeling (FDDM) or convolution quadrature techniques [27]. This can be attributed to challenges: (i) For media with dispersive material properties, time domain Green function does not have a closed-form analytical expression. Note that for non-dispersive media Green function is simply a Dirac delta function in space and time variables. Similarly, dispersive dielectric permittivity does not have closed form expression in time domain unless one of the simplified models, such as Drude or Drude-Lorentz [28], are used. (ii) Because both the Green function and material properties are dispersive, scattered field computations require evaluation of double temporal convolution. Schemes to discretize this double convolution have never been investigated. (iii) The dispersive Green function has an infinite tail in time domain, significantly increasing the computational cost of temporal convolutions mentioned in (ii). But this cost can be significantly reduced by using the recently developed plane wave time domain (PWTD) [25, 29] and blocked fast Fourier transform (FFT)-based schemes [30]. The TD-SIE solvers [26, 31], which make use of FDDM or CQ techniques [27], formulate and discretize the SIEs in the Laplace domain, approximate the Laplace domain parameter s in the z-domain using a finite difference scheme, and finally convert the resulting system into time domain through the inverse z-transform. Since the SIE is constructed in the Laplace domain, these TD-SIE solvers do not face the challenges (i) and (ii) listed above. But they still require a fast method to efficiently compute (discretized) temporal convolutions after conversion into time

domain. This could similarly be remedied by FFT-based schemes [25, 30, 32–34].

In this work, a different approach is used. The TD-SIE is constructed directly in the time domain and temporal samples of the dispersive Green function and permittivity are obtained using separate inverse Fourier transforms applied to their frequency domain representations. The first part of this thesis, which is focused on formulation and implementation of this TD-SIE solver addresses the challenges described in (i) and (ii) above. More specifically,

- The well-known frequency domain Poggio-Miller-Chan-Harrington-Wu-Tsai-SIE (FD-PMCHWT-SIE) [35,36] is reformulated in time domain to account for scatterers with lossy and dispersive material properties (Chapters 2 and 3).

- A numerical scheme to compute samples of the dispersive medium's time domain Green function and dielectric permittivity from their frequency domain samples is developed (Chapter 3).

- A numerical scheme to convert the double temporal convolution into a double discrete summation, where the inner summation corresponds to the convolution of the Green function and temporal basis function, is developed (Chapters 2 and 3).

1.4 Modeling Quantum Tunneling Effects

As mentioned above, when the dimensions of the structures being analyzed are reduced to nanometer scales, quantum mechanical effects start to appear. One of these effects is the electron tunneling which generates an auxiliary current path between two structures that are located within a few nanometers of each other. Numerical schemes designed to solve Maxwell equations with classical constitutive relations do not account for this additional current path. To overcome this problem, hybrid approaches, which are termed "quantum corrected models" have been developed [6,37]. Quantum-corrected analysis assumes that, due to the electron jump, a conductive auxiliary tunnel is generated between two structures. The complex permittivity of

this tunnel is represented using a Drude model with two parameters: plasma and damping frequencies. Plasma frequency of the tunnel is assumed to be same as that of structures being "connected" by the tunnel. To compute the damping frequency, first the tunneling probability of an electron is obtained by solving a 1D problem between two semi-infinite planar surfaces made of the material of the structures being connected by the tunnel. Then, this tunneling probability is used for computing the conductivity of the tunnel, which consequently provides a value for the damping frequency. At the final stage of the analysis, plasmonic field interactions on the structures and the tunnel connecting them are analyzed using a FD-SIE solver. The second part of the work described in this thesis, proposes to improve the accuracy of the quantum correction model briefly described above. More specifically,

- Complex permittivity of the tunnel is obtained from density functional theory computations, which account for the atomic structure of the material and inter-band and intra-band contributions of electrons to the permittivity (Chapter 4).

- The material properties of the tunnel is "converted" into time domain (see previous section) and incorporated within the TD-SIE solver described in Chapters 2 and 3.

Chapter 2

TD-SIE Solver for Analyzing Scattering from Dissipative Media

2.1 Introduction

This chapter describes a time domain surface integral equation (TD-SIE) solver developed for analyzing transient electromagnetic interactions on dissipative (lossy) scatterers. Even though permittivity of a lossy scatterer does not change with frequency, the presence of a finite conductivity make its response to electromagnetic excitation dispersive. Consequently time domain formulation of scattering has to account for a Green function and permittivity with infinite temporal tails. These characteristics are shared by plasmonic scatterers where permittivity is a more complicated function of frequency. Consequently, the TD-SIE solver described in this chapter can be considered as a preliminary version of the one developed for computing transient electromagnetic interaction on plasmonic scatterers as explained in Chapter 3.

The first TD-SIE solver [38] for lossy dielectric scatterers was constructed by coupling four TD-SIE (in tangential and normal components of the fields) on the interface between the lossy scatterer and the lossless background medium. Because of the "operator scaling" introduced in these TD-SIEs to eliminate a temporal convolution, this scheme cannot be directly applied to scatterers with volumes of different conductivity. In [39], a scheme for solving the electric field SIE enforced on interfaces between volumes of different conductivity is proposed. But this scheme suffers from the problem of interior resonances when one of the volumes is lossless [21].

In this work, a more general TD-SIE solver is proposed for characterizing transient electromagnetic interactions on lossy dielectrics. This scheme solves the time domain Poggio-Miller-Chan-Harrington-Wu-Tsai-SIE (TD-PMCHWT-SIE) for the tangential components of the electric and magnetic fields on the interfaces between (lossy) dielectric volumes. The unknowns are approximated using the Rao-Wilton-Glisson (RWG) basis functions [40] in space and Lagrange polynomials [23] in time. Inserting these approximations into the TD-PMCHWT-SIE and Galerking testing the resulting equation at discrete times yield a system of equations [41]. This system is solved by marching on-in-time (MOT) scheme. This scheme is distinguished from other TD-SIE solvers developed for lossy scatterers in two ways: (i) The proposed MOT scheme can directly be applied to scatterers with volumes of different conductivity and does not have the interior resonance problem (incase any one of the volumes is lossless) since it uses the PMCHWT formulation. (ii) The TD-PMCHWT-SIE has a convolution term that involves the complex permittivity's inverse Fourier transform, Green function, and charge density. This term is discretized into a double discrete summation where the inner summation corresponds to the convolution of the Green function and basis functions. The multipliers in the outer summation depend only on the conductivity and permittivity, therefore they are pre-computed per medium without introducing any significant computational burden. For unaccelerated MOT schemes, the multipliers in the outer summation are simply combined with the matrix entries resulting from the convolution of the Green function and basis functions. For fast Fourier transform (FFT) or plane wave time domain (PWTD) accelerated MOT schemes [25,29], the outer summation is computed efficiently using blocked-FFTs [30].

The rest of this chapter is organized as follows: Section 2.2 describes the formulation and discretization of the equation underlying the proposed solver. It specifically focuses on the computation of the additional convolutions arising due to the fact that the scatterers is dissipative. Section 2.3 provides numerical results demonstrating

the accuracy and applicability of the proposed solver. Finally, Section 2.4 provides a summary of the chapter.

2.2 Formulation

2.2.1 TD-PMCHWT-SIE

Let $V = \bigcup_{p=0}^{M} V_p$ represent the total volume of a composite scatterer consisting of M number of isotropic, homogeneous, and conductive regions. Volume, permittivity, permeability, and conductivity of these regions are denoted by V_p, ε_p, μ_p, and σ_p, respectively. The surface of interface between regions p and q is represented by S_{pq}, $p, q = 1, ..., N$, $p \neq q$, and $\hat{\mathbf{n}}_{pq}(\mathbf{r})$ is the unit normal vector on S_{pq} pointing towards V_p. Note that $S_{pq} = S_{qp}$ and $\hat{\mathbf{n}}_{pq}(\mathbf{r}) = -\hat{\mathbf{n}}_{qp}(\mathbf{r})$. Let $\mathbf{E}_p^{\text{inc}}(\mathbf{r}, t)$ and $\mathbf{H}_p^{\text{inc}}(\mathbf{r}, t)$ denote the incident electric and magnetic fields due to a source located in V_p. It is assumed that $\mathbf{E}_p^{\text{inc}}(\mathbf{r}, t)$ and $\mathbf{H}_p^{\text{inc}}(\mathbf{r}, t)$ are zero $\forall \mathbf{r} \in V_p$, $t < 0$ and bandlimited to $f_{\max}$. Upon excitation, equivalent electric and magnetic current densities $\mathbf{J}_{pq}(\mathbf{r}, t)$ and $\mathbf{M}_{pq}(\mathbf{r}, t)$ are induced on S_{pq}. Note that $\mathbf{J}_{pq}(\mathbf{r}, t) = -\mathbf{J}_{qp}(\mathbf{r}, t)$ and $\mathbf{M}_{pq}(\mathbf{r}, t) = -\mathbf{M}_{qp}(\mathbf{r}, t)$. PMCHWT-SIE is obtained using surface equivalence principles and boundary conditions [36]:

$$\begin{aligned}
&\hat{\mathbf{n}}_{pq}(\mathbf{r}) \times \partial_t \mathbf{E}_p^{\text{inc}}(\mathbf{r}, t) + \hat{\mathbf{n}}_{qp}(\mathbf{r}) \times \partial_t \mathbf{E}_q^{\text{inc}}(\mathbf{r}, t) = \\
&- \hat{\mathbf{n}}_{pq}(\mathbf{r}) \times \sum_{p'} [\mathcal{L}_p\{\mathbf{J}_{pp'}(\mathbf{r}, t)\} - \mathcal{K}_p\{\mathbf{M}_{pp'}(\mathbf{r}, t)\}] \\
&- \hat{\mathbf{n}}_{qp}(\mathbf{r}) \times \sum_{q'} [\mathcal{L}_q\{\mathbf{J}_{qq'}(\mathbf{r}, t)\} - \mathcal{K}_q\{\mathbf{M}_{qq'}(\mathbf{r}, t)\}]
\end{aligned} \tag{2.1}$$

$$\begin{aligned}
&\hat{\mathbf{n}}_{pq}(\mathbf{r}) \times \partial_t \mathbf{H}_p^{\text{inc}}(\mathbf{r}, t) + \hat{\mathbf{n}}_{qp}(\mathbf{r}) \times \partial_t \mathbf{H}_q^{\text{inc}}(\mathbf{r}, t) = \\
&- \hat{\mathbf{n}}_{pq}(\mathbf{r}) \times \sum_{p'} [\mathcal{P}_p\{\mathbf{M}_{pp'}(\mathbf{r}, t)\} + \mathcal{K}_p\{\mathbf{J}_{pp'}(\mathbf{r}, t)\}] \\
&- \hat{\mathbf{n}}_{qp}(\mathbf{r}) \times \sum_{q'} [\mathcal{P}_q\{\mathbf{M}_{qq'}(\mathbf{r}, t)\} + \mathcal{K}_q\{\mathbf{J}_{qq'}(\mathbf{r}, t)\}].
\end{aligned} \tag{2.2}$$

The integral operators $\mathcal{L}_p\{\cdot\}$, $\mathcal{K}_p\{\cdot\}$, and $\mathcal{P}_p\{\cdot\}$ are

$$\mathcal{L}_p\{\mathbf{X}_{pp'}(\mathbf{r},t)\} = -\mu_p\mathcal{V}_p\{\partial_t\mathbf{X}_{pp'}(\mathbf{r},t)\} + \frac{1}{\varepsilon_p}\mathcal{Q}_p\{\mathbf{X}_{pp'}(\mathbf{r},t)\} - \mathcal{Q}_p\{\gamma_p(t) * \mathbf{X}_{pp'}(\mathbf{r},t)\} \tag{2.3}$$

$$\mathcal{P}_p\{\mathbf{X}_{pp'}(\mathbf{r},t)\} = -\varepsilon_p\mathcal{V}_p\{\partial_t\mathbf{X}_{pp'}(\mathbf{r},t)\} + \frac{1}{\mu_p}\mathcal{Q}_p\{\mathbf{X}_{pp'}(\mathbf{r},t)\} - \sigma_p\mathcal{V}_p\{\mathbf{X}_{pp'}(\mathbf{r},t)\} \tag{2.4}$$

$$\mathcal{K}_p\{\mathbf{X}_{pp'}(\mathbf{r},t)\} = \nabla \times \mathcal{V}_p\{\mathbf{X}_{pp'}(\mathbf{r},t)\} \tag{2.5}$$

where

$$\mathcal{V}_p\{\mathbf{X}_{pp'}(\mathbf{r},t)\} = \int\limits_{S_{pp'}} g_p(R,t) * \partial_t\mathbf{X}_{pp'}(\mathbf{r}',t)ds' \tag{2.6}$$

$$\mathcal{Q}_p\{\mathbf{X}_{pp'}(\mathbf{r},t)\} = \nabla \int\limits_{S_{pp'}} g_p(R,t) * \nabla' \cdot \mathbf{X}_{pp'}(\mathbf{r}',t)ds'. \tag{2.7}$$

Here, $g_p(R,t)$ is the Green function of the unbounded medium with the same material properties as V_p, $R = |\mathbf{r} - \mathbf{r}'|$ is the distance between the observer and source points $\mathbf{r}$ and $\mathbf{r}'$, and ∂_t and $*$ denote the temporal derivative and convolution, respectively. The Green function $g_p(R,t)$ satisfies wave the equation [42]:

$$\nabla^2 g_p(R,t) + \mu_p\sigma_p\partial_t g_p(R,t) - \frac{1}{c_p^2}\partial_t^2 g_p(R,t) = -4\pi\delta(R)\delta(t) \tag{2.8}$$

and can be obtained in closed-form as

$$g_p(R,t) = \frac{e^{-bt}}{4\pi R}\delta(\tau) + \frac{be^{-bt}}{4\pi c_p}\frac{I_1(ba)}{a}u(\tau). \tag{2.9}$$

Using (2.9), one can easily obtain the spatial derivative of $g_p(R,t)$ in closed form as

$$\frac{\partial g_p(R,t)}{\partial R} = -\frac{e^{-\frac{b}{c_p}R}}{4\pi R}\left\{\frac{\delta(\tau)}{R} + \frac{b\delta(\tau)}{c_p} + \frac{\delta'(\tau)}{c_p}\right\} - \frac{Rbe^{-bt}}{4\pi c_p^2}\left\{\frac{b\delta(\tau)}{2R} - \frac{2I_1(ba)u(\tau)}{a^3 c_p} + \frac{bI_0(ba)u(\tau)}{a^2 c_p}\right\}. \tag{2.10}$$

Here $\tau = t - R/c_p$, $c_p = 1/\sqrt{\varepsilon_p \mu_p}$ is the speed of light, $b = \sigma_p/(2\varepsilon_p)$, $a = \sqrt{t^2 - R^2/c_p^2}$, $I_0(\cdot)$ is the zeroth order modified Bessel function of the first kind $I_1(\cdot)$ is the first order modified Bessel function of the first kind, $\delta(\cdot)$ is the Dirac delta function, $\delta'(\cdot)$ is the derivative of Dirac delta function, and $u(\cdot)$ is the unit step function. In (2.3), $\gamma_p(t)$ is obtained analytically using inverse Fourier transform as

$$\gamma_p(t) = \mathcal{F}^{-1}\left\{\frac{\sigma_p}{\varepsilon_p(\sigma_p + j\omega\varepsilon_p)}\right\} = \frac{\sigma_p}{\varepsilon_p^2} e^{-\frac{\sigma_p t}{\varepsilon_p}} u(t). \tag{2.11}$$

Several observations about the TD-PMCHWT-SIE in (2.1) and (2.2) are in order: (i) Summations over indices p' and q' represent the contribution to the scattered electric and magnetic fields evaluated on S_{pq} from the currents induced on $S_{pp'}$ and $S_{qq'}$ surrounding V_p and V_q, respectively. (ii) Eqs. (2.1) and (2.2) are "scaled" with ∂_t to eliminate a time integral that would be present in the operator $\mathcal{Q}_p\{\cdot\}$. It should be noted here that unlike the scaling factor $\partial_t + \sigma/\varepsilon$ used in SIEs formulated in [25, 38], this operation does not limit the applicability of (2.1) and (2.2) to volumes with the same conductivity. (iii) Discretization of $\mathcal{Q}_p\{\gamma_p(t) * \mathbf{X}_{pp'}(\mathbf{r},t)\}$ in (2.3) requires discretization of two convolutions applied back to back. (iv) If $\sigma_p = 0$, then $g_p(R,t) = \delta(\tau)/(4\pi R)$. Additionally, last terms in (2.3) and (2.4) vanish since $\gamma_p(t) = 0$ and $\sigma_p = 0$. Consequently, the TD-PMCHWT-SIE in (2.1) and (2.2) is reduced to that in [41].

2.2.2 Discretization and MOT Scheme

Equivalent surface current densities are expanded using Rao-Wilton-Glisson (RWG) functions $\mathbf{f}_{e'n'}(\mathbf{r})$ [40] in space, where e' refers to the index of S_{pq} and n' is the index of the basis functions on S_{pq}, and shifted Lagrange interpolation functions $T^{j'}(t) = T(t - j'\Delta t)$ [23] in time:

$$\mathbf{J}_{e'}(\mathbf{r},t) = \sum_{j'=1}^{N_t}\sum_{n'=1}^{N_e} J_{e'n'}^{j'}\mathbf{f}_{e'n'}(\mathbf{r})T^{j'}(t) \tag{2.12}$$

$$\mathbf{M}_{e'}(\mathbf{r},t) = \sum_{j'=1}^{N_t}\sum_{n'=1}^{N_e} M_{e'n'}^{j'}\mathbf{f}_{e'n'}(\mathbf{r})T^{j'}(t). \tag{2.13}$$

Here, $J_{e'n'}^{j'}$ and $M_{e'n'}^{j'}$ are the unknown coefficients, Δt is the time step size, N_e and N_t are the numbers of spatial basis functions on S_{pq} and time steps, respectively. Inserting (2.12) and (2.13) into (2.1) and (2.2) and testing the resulting equations with $\hat{\mathbf{n}}_{pq}(\mathbf{r}) \times \mathbf{f}_{en}(\mathbf{r})\delta(t - j\Delta t)$, $e \in S_{pq}$, $n = 1, ..., N_e$, result in a system of equations:

$$\begin{aligned}
&\sum_{j'=1}^{j}\Bigg\{\sum_{p'}\alpha_{pp'}\sum_{e'\in S_{pp'}}\sum_{n'}[A_{p,en,e'n'}^{j-j'}J_{e'n'}^{j'} - B_{p,en,e'n'}^{j-j'}M_{e'n'}^{j'}] \\
&- \sum_{q'}\alpha_{qq'}\sum_{e'\in S_{qq'}}\sum_{n'}[A_{q,en,e'n'}^{j-j'}J_{e'n'}^{j'} - B_{q,en,e'n'}^{j-j'}M_{e'n'}^{j'}]\Bigg\} \\
&= E_{pq,en}^{j}
\end{aligned} \tag{2.14}$$

$$\begin{aligned}
&\sum_{j'=1}^{j}\Bigg\{\sum_{p'}\alpha_{pp'}\sum_{e'\in S_{pp'}}\sum_{n'}[C_{p,en,e'n'}^{j-j'}M_{e'n'}^{j'} + B_{p,en,e'n'}^{j-j'}J_{e'n'}^{j'}] \\
&- \sum_{q'}\alpha_{qq'}\sum_{e'\in S_{qq'}}\sum_{n'}[C_{q,en,e'n'}^{j-j'}M_{e'n'}^{j'} + B_{q,en,e'n'}^{j-j'}J_{e'n'}^{j'}]\Bigg\} \\
&= H_{pq,en}^{j}
\end{aligned} \tag{2.15}$$

where

$$E^{j}_{pq,en} = -\left\langle \mathbf{f}_{en}(\mathbf{r}), \partial_t \mathbf{E}^{\text{inc}}_{p}(\mathbf{r},t) - \partial_t \mathbf{E}^{\text{inc}}_{q}(\mathbf{r},t) \right\rangle_{t=j\Delta t} \tag{2.16}$$

$$H^{j}_{pq,en} = -\left\langle \mathbf{f}_{en}(\mathbf{r}), \partial_t \mathbf{H}^{\text{inc}}_{p}(\mathbf{r},t) - \partial_t \mathbf{H}^{\text{inc}}_{q}(\mathbf{r},t) \right\rangle_{t=j\Delta t} \tag{2.17}$$

$$A^{j-j'}_{p,en,e'n'} = \left\langle \mathbf{f}_{en}(\mathbf{r}), \mathcal{L}_p\{\mathbf{f}_{e'n'}(\mathbf{r}) T^{j'}(t)\} \right\rangle_{t=j\Delta t} \tag{2.18}$$

$$B^{j-j'}_{p,en,e'n'} = \left\langle \mathbf{f}_{en}(\mathbf{r}), \mathcal{K}_p\{\mathbf{f}_{e'n'}(\mathbf{r}) T^{j'}(t)\} \right\rangle_{t=j\Delta t} \tag{2.19}$$

$$C^{j-j'}_{p,en,e'n'} = \left\langle \mathbf{f}_{en}(\mathbf{r}), \mathcal{P}_p\{\mathbf{f}_{e'n'}(\mathbf{r}) T^{j'}(t)\} \right\rangle_{t=j\Delta t} \tag{2.20}$$

$\langle \mathbf{f}_{en}(\mathbf{r}), \mathbf{X}(\mathbf{r},t) \rangle = \int_{\Delta_{en}} \mathbf{f}_{en}(\mathbf{r}) \cdot \mathbf{X}(\mathbf{r},t) ds$, Δ_{en} is the support of the testing function $\mathbf{f}_{en}(\mathbf{r})$, and $\alpha_{pp'} = \pm 1$ for $p \gtrless p'$. Eqs. (2.14) and (2.15) are brought into a form that can be solved using the well-known MOT scheme [41]:

$$\bar{\bar{Z}}_0 \bar{I}_j = \bar{V}_j - \sum_{j'=1}^{j-1} \bar{\bar{Z}}_{j-j'} \bar{I}_{j'} \tag{2.21}$$

where, $\bar{I}_j$ and $\bar{V}_j$ are $N \times 1$ vectors storing the unknown coefficients and tested fields at time step j and $\bar{\bar{Z}}_{j-j'}$ are the $N \times N$ MOT matrices. Here, $N = 2\sum_{e \in S_{pq}} N_e$ and $\bar{V}_j$ and $\bar{\bar{Z}}_{j-j'}$ are constructed by combining the vector and matrix elements in (2.16)-(2.17) and (2.18)-(2.20), respectively.

2.2.3 Time Domain Green Function and Temporal Convolutions

The Green function in (2.9) and the derivative of the Green function in (2.10) has to be evaluated for each distance R and that is computationally expensive. One way to avoid this computation is to build up a table [39] for a set of equally spaced distances $\{R_1, R_2, ..., R_{max}\}$ with steps of ΔR and compute the Green function and its derivative only for these distances. Then, for any distance R, the Green function and its derivative are evaluated by using linear interpolation and the table. Here,

the tables for the Green function and its derivative constructed by analytic formulas in (2.9) and (2.10) evaluating the associated Bessel functions. Note that accelerated schemes [43, 44] to compute Green function can be used instead of tables.

The scheme described above requires two types of convolutions to be computed at $t = j\Delta t$ the testing points.

Type-1 Convolutions: Convolutions of $g_p(R,t)$ with $\mathbf{f}_{e'n'}(\mathbf{r})T^{j'}(t)$ and $\nabla\cdot\mathbf{f}_{e'n'}(\mathbf{r})T^{j'}(t)$, (i.e., $\mathcal{V}_p\{\mathbf{f}_{e'n'}(\mathbf{r})T^{j'}(t)\}_{t=j\Delta t}$ and $\mathcal{Q}_p\{\mathbf{f}_{e'n'}(\mathbf{r})T^{j'}(t)\}_{t=j\Delta t}$). Methods to efficiently compute these convolutions are proposed in [39, 44] and are not described here.

Type-2 Convolutions: Convolution of $g_p(R,t)$ with $\gamma_p(t) * \nabla\cdot\mathbf{f}_{e'n'}(\mathbf{r})T^{j'}(t)$ (i.e., $\mathcal{Q}_p\{\gamma_p(t) * \mathbf{f}_{e'n'}(\mathbf{r})T^{j'}(t)\}_{t=j\Delta t}$). The method to compute this convolution is one of the contributions of the work described in this chapter. This method represents

$$\begin{aligned}&\mathcal{Q}_p\{\gamma_p(t) * \mathbf{f}_{e'n'}(\mathbf{r})T^{j'}(t)\}_{t=j\Delta t} \\ &= \left\{\nabla \int\limits_{\Delta_{e'n'}} g_p(R,t) * \gamma_p(t) * \nabla'\cdot\mathbf{f}_{e'n'}(\mathbf{r}')T^{j'}(t)ds'\right\}_{t=j\Delta t}\end{aligned} \tag{2.22}$$

in terms of $\mathcal{Q}_p\{\mathbf{f}_{e'n'}(\mathbf{r})T^{j'}(t)\}_{t=j\Delta t}$ (type-1 convolution), which can be computed efficiently using existing methods [39, 44]. To this end, first, the auxiliary function $F_p^{j'}(t) = \gamma_p(t) * T^{j'}(t)$ is approximated using

$$F_p^{j'}(t) = \sum_{l'=1}^{N_t} \tilde{F}_p^{j'l'} T^{l'}(t) \tag{2.23}$$

where $\tilde{F}_p^{j'l'} = F_p^{j'}(l'\Delta t) = \gamma_p(t) * T^{j'}(t)\big|_{t=l'\Delta t}$ are

$$\begin{aligned}\tilde{F}_p^{j'l'} &= \int\limits_{\max([l'-j'-d]\Delta t,0)}^{(l'-j'+1)\Delta t} \gamma_p(t')T([l'-j']\Delta t - t')dt' \\ &= \int\limits_{-\Delta t}^{\min(l'-j',d)\Delta t} \gamma_p([l'-j']\Delta t - \tilde{t})T(\tilde{t})d\tilde{t} = \tilde{F}_p^{l'-j'}.\end{aligned} \tag{2.24}$$

Here, $[-\Delta t, d\Delta t]$ and d are the support and order of $T(t)$, respectively. In (2.24) notation representing $F_p^{j'}(l'\Delta t)$ is changed to $\tilde{F}_p^{l'-j'}$ because they depend only on $l'-j'$. Note that $\tilde{F}_p^{l'-j'}=0$ for $j'\geq l'+1$. For $d=4$ [33], the integral in (2.24) is given by

$$\begin{aligned}
\tilde{F}_p^0 =&[Y(e^{-y}-1)-12y+24y^2-22y^3+12y^4]x \qquad (2.25)\\
\tilde{F}_p^1 =&[Y(e^{-2y}-5e^{-y}+4)+36y-60y^2+36y^3]x\\
\tilde{F}_p^2 =&[Y(e^{-3y}-5e^{-2y}+10e^{-y}-6)-36y+48y^2-18y^3]x\\
\tilde{F}_p^3 =&[Y(e^{-4y}-5e^{-3y}+10e^{-2y}-10e^{-y}+4)\\
&+12y-12y^2+4y^3]x\\
\tilde{F}_p^4 =&Y(e^{-y}-1)^5x\\
\tilde{F}_p^k =&e^{-y}\tilde{F}_p^{k-1}, k>4
\end{aligned}$$

where, $y=\Delta t\sigma_p/\varepsilon_p$, $x=\varepsilon_p^3/(12\Delta t^4\sigma_p^4)$, and $Y=-12+18y-11y^2+3y^3$. Inserting (2.23) into (2.22) yields

$$\begin{aligned}
&\mathcal{Q}_p\{\gamma_p(t)*\mathbf{f}_{e'n'}(\mathbf{r})T^{j'}(t)\}_{t=j\Delta t} \qquad (2.26)\\
&=\sum_{l'=1}^{j}\tilde{F}_p^{l'-j'}\left\{\nabla\int\limits_{\Delta_{e'n'}} g_p(R,t)*\nabla'\cdot\mathbf{f}_{e'n'}(\mathbf{r}')T^{l'}(t)ds'\right\}_{t=j\Delta t}\\
&=\sum_{l'=1}^{j}\tilde{F}_p^{l'-j'}\mathcal{Q}_p\{\mathbf{f}_{e'n'}(\mathbf{r})T^{l'}(t)\}_{t=j\Delta t}.
\end{aligned}$$

This shows that the computation of type-2 convolution $\mathcal{Q}_p\{\gamma_p(t)*\mathbf{f}_{e'n'}(\mathbf{r})T^{j'}(t)\}_{t=j\Delta t}$ is reduced to that of type-1 convolution $\mathcal{Q}_p\{\mathbf{f}_{e'n'}(\mathbf{r})T^{l'}(t)\}_{t=j\Delta t}$. Finally, contribution

from fully tested $\mathcal{Q}_p\{\gamma_p(t) * \mathbf{f}_{e'n'}(\mathbf{r})T^{j'}(t)\}$ to $\bar{\bar{Z}}_{j-j'}$ is expressed as

$$\left\langle \mathbf{f}_{en}(\mathbf{r}), \mathcal{Q}_p\{\gamma_p(t) * \mathbf{f}_{e'n'}(\mathbf{r})T^{j'}(t)\}\right\rangle\Big|_{t=j\Delta t} \tag{2.27}$$
$$= \sum_{l'=1}^{j} \left\langle \mathbf{f}_{en}(\mathbf{r}), \mathcal{Q}_p\{\mathbf{f}_{e'n'}(\mathbf{r})T^{l'}(t)\}\right\rangle_{t=j\Delta t} \tilde{F}_p^{l'-j'}.$$

Comments Several comments about the discretization scheme described above are in order: (i) Convolution in (2.24) depends only on ε_p and σ_p, therefore $\tilde{F}_p^{l'-j'}$ are computed and stored per volume. (ii) The cost of evaluating $\tilde{F}_p^{l'-j'}$ is negligible when compared to that of type-1 convolutions. For unaccelerated MOT schemes, the discrete sum in (2.27) is directly incorporated into the MOT matrices $\bar{\bar{Z}}_{j-j'}$ in (2.21) with almost no additional cost on computing $\bar{\bar{Z}}_{j-j'}$. The cost of time-marching stays exactly the same. (iii) For FFT or PWTD-accelerated MOT schemes [25, 29], the discrete summation $\sum_{j'=1}^{l'-1} \tilde{F}_p^{l'-j'} J_{e'n'}^{j'}$ that is present on the right-hand-side of (2.21) can be computed efficiently during time marching using blocked FFTs [30].

2.3 Numerical Results

In this section, the accuracy and the applicability of the proposed TD-PMCHWT-SIE solver are demonstrated via analysis of transient scattering from dielectric objects residing in free space. In all examples, the electric field of the incident plane wave is given by $\mathbf{E}_0^{\text{inc}}(\mathbf{r}, t) = \hat{\mathbf{x}}G(t-\hat{\mathbf{z}}\cdot\mathbf{r}/c_0)$, where $G(t) = \cos(2\pi f_0[t-t_0])\exp(-[t-t_0]^2/2\sigma^2)$ is a Gaussian pulse with modulation frequency f_0, duration $\sigma = 3/(2\pi f_{\text{bw}})$, bandwidth f_{bw}, and delay $t_0 = 7.5\sigma$. Excitation exists only in free space denoted as dielectric volume with $p = 0$. The first example is a layered sphere with inner and outer radius of 0.5 m. The relative permittivity and conductivity in the core and layer are 1.5 and 0.003 S/m and 1.3 and 0.001 S/m. For this simulation, $f_0 = 100$ MHz, $f_{\text{bw}} = 75$ MHz, $N = 6054$, $d = 4$, $N_t = 2000$, and $\Delta t = 0.1905$ ns. Fig. 2.1 plots the coefficients of two basis functions approximating electric and magnetic current densities. Results

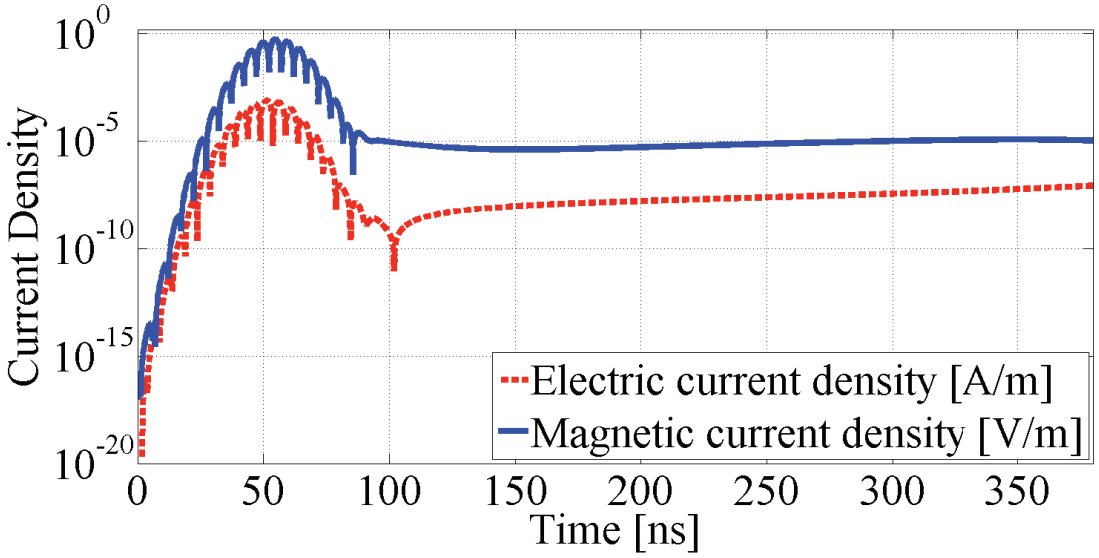

Figure 2.1: Coefficients of two basis functions approximating electric and magnetic current densities.

are stable for the duration of simulation. Fig. 2.2 compares radar cross section (RCS) results obtained from the MOT solution for $\phi = 0°$ and $0° \leq \theta < 180°$ at 50 MHz and 150 MHz to those obtained using Mie series. Results agree very well.

The second example is a six layer Luneburg lens [45]. Thicknesses, permittivities, and conductivities of the layers (from inner to outer) are { 0.39, 0.16, 0.13, 0.10, 0.10, 0.12 } mm, $\{1.92, 1.77, 1.62, 1.46, 1.31, 1.05\}$, and $\{0.096, 0.082,\ 0.071, 0.048, 0.035, 0\}$ S/m, respectively. For this simulation, $f_0 = 80$ GHz, $f_{\text{bw}} = 50$ GHz, $N = 7662$, $d = 4$, $N_t = 1000$, and $\Delta t = 0.2564$ ps. Fig. 3 compares RCS results obtained from the MOT and a frequency domain volume integral equation (FD-VIE) solutions for $\phi = 0°$ and $0° \leq \theta < 180°$ at 60 GHz and 100 GHz. Results agree very well.

2.4 Conclusion

In this chapter, a TD-PMCHWT-SIE for analyzing transient electromagnetic wave interactions on conductive dielectric scatterers and its solution by MOT scheme are described. The resulting solver, unlike previously developed schemes, allows for scatterers with multiple volumes of different conductivity with almost no increase in the

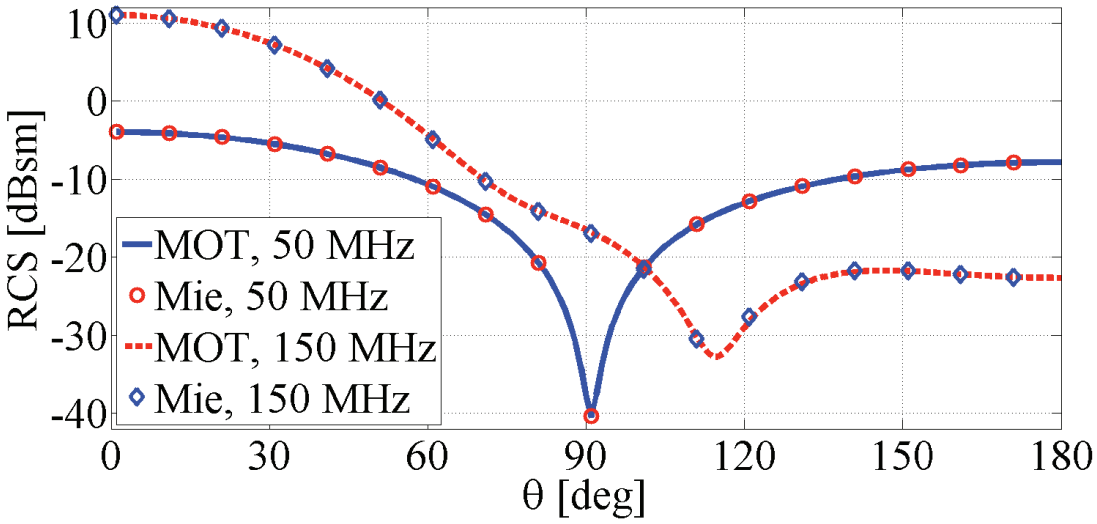

Figure 2.2: RCS obtained from the MOT and Mie-series solutions for $\phi = 0°$ and $0° \leq \theta < 180°$ at 50 MHz and 150 MHz.

computational cost. The accuracy and applicability of the solver is demonstrated by numerical examples. Extension of this scheme into dispersive plasmonic media is detailed in the next chapter.

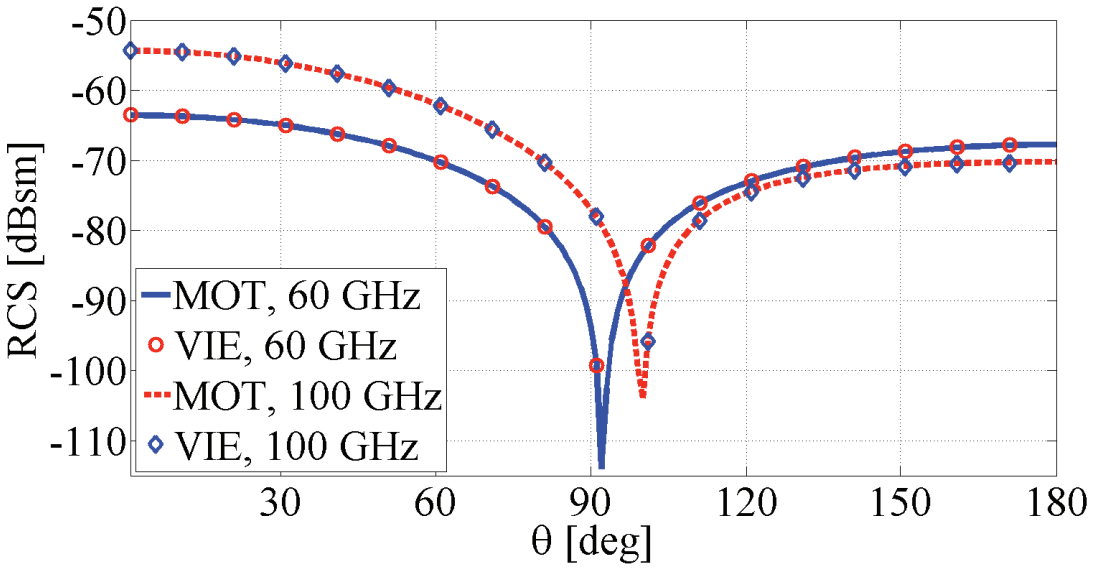

Figure 2.3: RCS obtained from the MOT and FD-VIE solutions for $\phi = 0°$ and $0° \leq \theta < 180°$ at 60 GHz and 100 GHz.

Chapter 3

TD-SIE Solver for Analyzing Scattering from Plasmonic Nanostructures

3.1 Introduction

Metallic nanostructures support surface plasmon modes upon illumination by electromagnetic fields at optical frequencies [1]. These modes significantly enhance scattering from nanostructures in the near- and far-field regions [1], enabling their use in various applications, such as design of nanoantennas for bio-chemical sensing [2], sub-wavelength waveguides for telecommunication [3], and ring-resonators for integrated compact optical components [46]. Characteristics of these plasmon modes, such as resonance frequency, propagation distance, amplitude decay rate, depend on the nanostructure's material properties, shape, and size as well as the material properties of the background medium where the nanostructure resides [1]. Therefore, simulation tools, which are capable of characterizing plasmonic field interactions on arbitrarily shaped geometries with certain material properties, have to be utilized to design a plasmonic nanostructure with desired field patterns in the near- and far-field regions.

Simulation tools implemented to analyze plasmonic field interactions make use of finite difference time domain (FDTD) schemes [47–49], finite element method (FEM) [50], discrete dipole approximation (DDA) [51], or surface integral equation (SIE) solvers [15–19]. Among these methods, FDTD is the most frequently used one due to its simplicity in formulation and implementation. However, FDTD (like any

other differential equation based solver such as FEM) requires volumetric discretizations of the plasmonic nanostructure and the surrounding medium. This becomes inefficient considering the fact that exponentially decaying behavior of the plasmonic fields could only be accurately captured using very small discretization elements especially in the vicinity of metal/dielectric interfaces. Also, the unbounded surrounding medium has to be truncated into a (bounded) computational domain [10]. This is achieved by using absorbing boundary conditions, which approximate field behavior at infinity. This approximation introduces significant errors especially while analyzing resonant phenomena requiring long durations of simulations [52]. Additionally, FDTD suffers from numerical dispersion introduced by finite difference approximations used for discretizing time and space derivatives. This produces additional error in the solution for electrically large objects and possibly leads to unphysical effects [11].

On the contrary, SIE solvers [15–19] only discretize the surfaces of the nanostructures (the dimension of the discretization domain is reduced to two from three - in comparison with FDTD and FEM) and the solution automatically satisfies the radiation condition (the field behavior at infinity is accurately captured without the need for approximate absorbing boundary conditions). However, use of SIE solvers for characterizing plasmonic field interactions has been limited to frequency domain. Consequently, these solvers cannot be used when material properties are functions of fields, such Kerr nonlinear materials [20, 28] and they have to be executed many times (one execution per frequency) to obtain broadband results, which are typically needed for designing plasmonic devices/system expected to operate over the support of multiple resonances.

These disadvantages can be overcome through formulation and implementation of SIE solvers for characterizing transient plasmonic field interactions. Time domain SIE (TD-SIE) solvers have long been used for analyzing electromagnetic field interactions on perfect electrically conducting (PEC) scatterers and dielectric objects with non-

dispersive material properties [22–25, 29–33, 53–55]. However, despite the advantages of using TD-SIE solvers have not been used for analyzing scattering from objects with dispersive material properties, with only one exception [26], which makes use of finite difference delay modeling (FDDM) or convolution quadrature (CQ) techniques [27]. This can be attributed to the following challenges: (i) For dispersive media, the dielectric permittivity does not have a closed-form expression in time domain unless one of the simplified models, such as Drude or Drude-Lorentz [28], is used. Consequently, the time domain Green function also does not have a closed-form expression. (ii) Because both the permittivity and the Green function are dispersive, scattered field computations require evaluation of additional convolutions between the permittivity, the Green function, and the equivalent currents. Schemes for discretizing these additional convolutions have never been formulated or implemented. (iii) The dispersive Green function has an infinite tail in time domain, which significantly increases the computational cost of the convolutions mentioned in (ii) [25, 29, 30, 33]. But this cost can be significantly reduced by using the recently developed fast Fourier transform (FFT)-based schemes [25, 30, 33, 34].

The TD-SIE solvers [26, 31], which make use of FDDM or CQ techniques [27], formulate and discretize the SIEs in the Laplace domain, approximate the Laplace domain parameter s in the z-domain using a finite difference scheme, and finally convert the resulting system into time domain through the inverse z-transform. Since the SIE is constructed in the Laplace domain, these TD-SIE solvers do not face the challenges (i) and (ii) listed above. But they still require a fast method to efficiently compute (discretized) temporal convolutions after conversion into time domain. This could similarly be remedied by FFT-based schemes [25, 30, 32–34].

In this work, a different approach is used. The TD-SIE is constructed directly in the time domain and temporal samples of the dispersive Green function and permittivity are obtained using separate inverse Fourier transforms applied to their fre-

quency domain representations. More specifically, the well-known frequency domain Poggio-Miller-Chan-Harrington-Wu-Tsai surface integral equation (FD-PMCHWT-SIE) [35,36] is extended in time domain to account for scatterers with dispersive material properties, more specifically plasmonic structures. The time domain PMCHWT-SIE (TD-PMCHWT-SIE) is solved using the well-known marching on-in-time (MOT) scheme [22–25, 29, 30, 32, 33, 53–55]. The MOT scheme expands the electric and magnetic current densities, which are introduced on the surfaces of the nanostructures, using Rao-Wilton-Glisson (RWG) [40] and polynomial basis functions [23,33] in space and time, respectively. Inserting this expansion into the TD-PMCHWT-SIE and Galerkin-testing the resulting equation at discrete times yield a system of equations that is solved for the current expansion coefficients by marching in time. The additional convolutions are converted into a double discrete summation, where the inner summation corresponds to the discretized convolution of the Green function and temporal basis function [56] [addressing the challenge (ii) above]. The temporal samples of the time domain dielectric permittivity and Green function, which are required by this MOT discretization procedure, are obtained numerically from their frequency domain samples [addressing the challenge (i) above]. This is achieved by representing the frequency domain Green function and permittivity in terms of a summation of weighted rational functions. The weighting coefficients are found by applying the fast relaxed vector fitting (FRVF) scheme to the frequency domain samples [57–59]. Time domain functions are then obtained by analytically computing the inverse Fourier transform of the summation.

The rest of this chapter is organized as follows: Section 3.2 describes the formulation and discretization of the TD-PMCHWT-SIE solver. Section 3.3 provides numerical results demonstrating the accuracy and applicability of the proposed solver. Finally, Section 3.4 gives a summary of the chapter.

3.2 Formulation

3.2.1 TD-PMCHWT-SIE

Let V_1 denote the volume of the plasmonic nanostructure with time dependent permittivity $\varepsilon_1(t)$ and constant permeability μ_1. Assume that the nanostructure resides in a non-dispersive unbounded background medium denoted by V_0. Constant permittivity and permeability in V_0 are represented by ε_0 and μ_0, respectively. Let S denote the surface enclosing V_1. An electromagnetic wave with electric and magnetic field intensities, $\mathbf{E}^{\text{inc}}(\mathbf{r},t)$ and $\mathbf{H}^{\text{inc}}(\mathbf{r},t)$, excites the nanostructure. It is assumed that $\mathbf{E}^{\text{inc}}(\mathbf{r},t) \approx 0$ and $\mathbf{H}^{\text{inc}}(\mathbf{r},t) \approx 0$, $\forall \mathbf{r} \in V_1$ and $t < 0$, and they are essentially band limited to $f_{\max}$. Using the surface equivalence principle [14] and the boundary conditions on S, the time derivative of the TD-PMCHWT-SIE is constructed as [55]

$$\hat{\mathbf{n}}(\mathbf{r}) \times \partial_t \mathbf{E}^{\text{inc}}(\mathbf{r},t) = -\hat{\mathbf{n}}(\mathbf{r}) \times [\partial_t \mathbf{E}_0^{\text{sca}}(\mathbf{r},t) - \partial_t \mathbf{E}_1^{\text{sca}}(\mathbf{r},t)] \tag{3.1}$$

$$\hat{\mathbf{n}}(\mathbf{r}) \times \partial_t \mathbf{H}^{\text{inc}}(\mathbf{r},t) = -\hat{\mathbf{n}}(\mathbf{r}) \times [\partial_t \mathbf{H}_0^{\text{sca}}(\mathbf{r},t) - \partial_t \mathbf{H}_1^{\text{sca}}(\mathbf{r},t)]. \tag{3.2}$$

Here, $\hat{\mathbf{n}}(\mathbf{r})$ is the unit normal vector at $\mathbf{r} \in S$, which is pointing towards V_0, and $\mathbf{E}_p^{\text{sca}}(\mathbf{r},t)$ and $\mathbf{H}_p^{\text{sca}}(\mathbf{r},t)$ are the scattered electric and magnetic field intensities in V_p, $p \in \{0,1\}$. $\mathbf{E}_p^{\text{sca}}(\mathbf{r},t)$ and $\mathbf{H}_p^{\text{sca}}(\mathbf{r},t)$ are expressed in terms of equivalent electric and magnetic current densities, $\mathbf{J}(\mathbf{r},t)$ and $\mathbf{M}(\mathbf{r},t)$, which are introduced on S using the surface equivalence principle:

$$\partial_t \mathbf{E}_0^{\text{sca}}(\mathbf{r},t) = -\mathcal{L}_0\{\mu_0 \mathbf{J}(\mathbf{r},t)\} + \mathcal{Q}_0\{\varepsilon_0^{-1} \mathbf{J}(\mathbf{r},t)\} - \mathcal{K}_0\{\mathbf{M}(\mathbf{r},t)\} \tag{3.3}$$

$$\partial_t \mathbf{H}_0^{\text{sca}}(\mathbf{r},t) = -\mathcal{L}_0\{\varepsilon_0 \mathbf{M}(\mathbf{r},t)\} + \mathcal{Q}_0\{\mu_0^{-1} \mathbf{M}(\mathbf{r},t)\} + \mathcal{K}_0\{\mathbf{J}(\mathbf{r},t)\} \tag{3.4}$$

$$\partial_t \mathbf{E}_1^{\text{sca}}(\mathbf{r},t) = \mathcal{L}_1\{\mu_1 \mathbf{J}(\mathbf{r},t)\} - \mathcal{Q}_1\{\bar{\varepsilon}_1(t) * \mathbf{J}(\mathbf{r},t)\} + \mathcal{K}_1\{\mathbf{M}(\mathbf{r},t)\} \tag{3.5}$$

$$\partial_t \mathbf{H}_1^{\text{sca}}(\mathbf{r},t) = \mathcal{L}_1\{\varepsilon_1(t) * \mathbf{M}(\mathbf{r},t)\} - \mathcal{Q}_1\{\mu_1^{-1}\mathbf{M}(\mathbf{r},t)\} - \mathcal{K}_1\{\mathbf{J}(\mathbf{r},t)\}. \tag{3.6}$$

In Eqs. (3.3)-(3.6), the integral operators $\mathcal{L}_p\{\cdot\}$, $\mathcal{Q}_p\{\cdot\}$, and $\mathcal{K}_p\{\cdot\}$ are given by

$$\mathcal{L}_p\{\mathbf{X}(\mathbf{r},t)\} = \int_S g_p(R,t) * \partial_t^2 \mathbf{X}(\mathbf{r}',t)ds' \tag{3.7}$$

$$\mathcal{Q}_p\{\mathbf{X}(\mathbf{r},t)\} = \nabla \int_S g_p(R,t) * \nabla' \cdot \mathbf{X}(\mathbf{r}',t)ds' \tag{3.8}$$

$$\mathcal{K}_p\{\mathbf{X}(\mathbf{r},t)\} = \nabla \times \int_S g_p(R,t) * \partial_t \mathbf{X}(\mathbf{r}',t)ds'. \tag{3.9}$$

Here, $g_p(R,t)$ is the Green function of the unbounded medium that has the same permittivity and permeability as V_p, $R = |\mathbf{r} - \mathbf{r}'|$ is the distance between source and observation points, $\mathbf{r}'$ and $\mathbf{r}$, '$*$' denotes temporal convolution, and $\bar{\varepsilon}_1(t)$ is the time domain inverse permittivity in V_1.

3.2.2 Time Domain Permittivity

Time domain permittivity and inverse permittivity of the plasmonic nanostructure, $\varepsilon_1(t)$ and $\bar{\varepsilon}_1(t)$, are obtained by inverse Fourier transforming their frequency domain counterparts, $\varepsilon_1(\omega)$ and $1/\varepsilon_1(\omega)$, respectively:

$$\varepsilon_1(t) = \mathfrak{F}^{-1}\{\varepsilon_1(\omega)\} \tag{3.10}$$

$$\bar{\varepsilon}_1(t) = \mathfrak{F}^{-1}\{\bar{\varepsilon}_1(\omega)\} = \mathfrak{F}^{-1}\{1/\varepsilon_1(\omega)\}. \tag{3.11}$$

Here, it is assumed that frequency samples of $\varepsilon_1(\omega)$ and $\bar{\varepsilon}_1(\omega)$, i.e., $\varepsilon_1(\omega_i)$ and $\bar{\varepsilon}_1(\omega_i)$, $i = 1, ..., N_\omega^{\text{VF}}$, where $\omega_i \in 2\pi[f_{\min}^{\text{VF}}, f_{\max}^{\text{VF}}]$, are available from tabulated experimental data, such those provided for silver and gold in [60] and [61]. Using the FRVF scheme [57–59] (see Appendix) on $\varepsilon_1(\omega_i)$ and $\bar{\varepsilon}_1(\omega_i)$, one can approximate $\varepsilon_1(\omega)$ and

$\bar{\varepsilon}_1(\omega)$ as

$$\varepsilon_1(\omega) - \varepsilon_1^{\infty} \approx \sum_{m=1}^{N_{\mathrm{p}}^{\mathrm{VF}}} \frac{b_m^{\epsilon}}{\mathrm{j}\omega + a_m^{\epsilon}} \tag{3.12}$$

$$\bar{\varepsilon}_1(\omega) - \frac{1}{\varepsilon_1^{\infty}} \approx \sum_{m=1}^{N_{\mathrm{p}}^{\mathrm{VF}}} \frac{b_m^{\bar{\epsilon}}}{\mathrm{j}\omega + a_m^{\bar{\epsilon}}} \tag{3.13}$$

where $\mathrm{j} = \sqrt{-1}$ is the imaginary number and $\varepsilon_1^{\infty} = 1$ is the high frequency limit of $\varepsilon_1(\omega)$ as $\omega \to \infty$. $\{a_m^{\epsilon}, b_m^{\epsilon}\}$ and $\{a_m^{\bar{\epsilon}}, b_m^{\bar{\epsilon}}\}$ are the pole/residue pairs obtained by applying the FRVF scheme to $\varepsilon_1(\omega_i)$ and $\bar{\varepsilon}_1(\omega_i)$. Inverse Fourier transforming Eqs. (3.12) and (3.13) yields

$$\varepsilon_1(t) \approx \varepsilon_1^{\infty}\delta(t) + \sum_{m=1}^{N_{\mathrm{p}}^{\mathrm{VF}}} b_m^{\epsilon} u(t) e^{-a_m^{\epsilon} t} = \varepsilon_1^{\infty}\delta(t) + \gamma_1(t) \tag{3.14}$$

$$\bar{\varepsilon}_1(t) \approx \frac{1}{\varepsilon_1^{\infty}}\delta(t) + \sum_{m=1}^{N_{\mathrm{p}}^{\mathrm{VF}}} b_m^{\bar{\epsilon}} u(t) e^{-a_m^{\bar{\epsilon}} t} = \frac{1}{\varepsilon_1^{\infty}}\delta(t) + \bar{\gamma}_1(t) \tag{3.15}$$

where $\delta(\cdot)$ and $u(\cdot)$ are the Dirac delta and the unit step functions, respectively. It should be noted here that the causality of $\varepsilon_1(t)$ and $\bar{\varepsilon}_1(t)$ is ensured by enforcing $a_m^{\epsilon} > 0$ and $a_m^{\bar{\epsilon}} > 0$ during the execution of the FRVF scheme.

3.2.3 Time Domain Green Function

The integral operators $\mathcal{L}_p\{\cdot\}$, $\mathcal{Q}_p\{\cdot\}$, and $\mathcal{K}_p\{\cdot\}$ present in Eqs. (3.3)-(3.6) and given by Eqs. (3.7)-(3.9) require $g_p(R,t)$ and its derivative with respect to R, $\partial_R g_p(R,t)$, [due to the presence of the curl operation in (3.9)] to be known. For $p = 0$ (in the background medium), since ε_0 and μ_0 are simply constants, $g_0(R,t) = \delta(t - R/c_0)/(4\pi R)$ and $\partial_R g_0(R,t) = -\delta'(t - R/c_0)/(4\pi c_0 R) + \delta(t - R/c_0)/(4\pi R^2)$ [42]. Here, $c_0 = 1/\sqrt{\varepsilon_0\mu_0}$ is the speed of light in the background medium and $\delta'(\cdot)$ is the derivative of the Dirac delta function with respect to its argument. On the other hand, for $p = 1$, general analytical expressions for $g_1(R,t)$ and $\partial_R g_1(R,t)$ are

not immediately available due to the dependence of $\varepsilon_1(t)$ on time. This can be explained by the fact that, for the dispersive $\varepsilon_1(\omega)$, the inverse Fourier transform of the frequency domain Green function $g_1(R,\omega) = e^{-\mathrm{j}k_1 R}/(4\pi R)$, may not exist in closed-form. Note that, here, $k_1 = \omega\sqrt{\varepsilon_1(\omega)\mu_1}$ is the complex wave number in V_1 . To overcome this problem and obtain expressions for $g_1(R,t)$ and $\partial_R g_1(R,t)$, the FRVF scheme is used in the same way as it is used to obtain the expressions of $\varepsilon_1(t)$ and $\bar{\varepsilon}_1(t)$ in Section 3.2.2. However, a naive application of the FRVF scheme to the samples of $g_1(R,\omega)$ and $\partial_R g_1(R,\omega)$ does not yield accurate representations for $g_1(R,t)$ and $\partial_R g_1(R,t)$. Singular term $1/(4\pi R)$ (corresponding to a Dirac delta function in time) and phase $e^{\mathrm{j}\omega R/c_1}$, $c_1 = 1/\sqrt{\varepsilon_1^{\infty}\mu_1}$ (corresponding to a delay in time) are first extracted from $g_1(R,\omega)$. Then, the FRVF scheme is applied to the samples of the remaining function at $\omega_i \in 2\pi[f_{\min}^{\mathrm{VF}}, f_{\max}^{\mathrm{VF}}]$, $i = 1, ..., N_{\omega}^{\mathrm{VF}}$ to yield

$$e^{\mathrm{j}\omega R/c_1}\left[g_1(R,\omega) - \frac{e^{-\mathrm{j}\omega R/c_1}}{4\pi R}\right] = \frac{e^{-\mathrm{j}(k_1 R - \omega R/c_1)} - 1}{4\pi R} \approx d^{\mathrm{g}}(R) + \sum_{m=1}^{N_{\mathrm{p}}^{\mathrm{VF}}} \frac{b_m^{\mathrm{g}}(R)}{j\omega + a_m^{\mathrm{g}}(R)}. \tag{3.16}$$

Here, $\{a_m^{\mathrm{g}}(R), b_m^{\mathrm{g}}(R)\}$ are the pole/residue pairs and $d^{\mathrm{g}}(R)$ is the constant term (with respect to frequency dependence) generated by the FRVF scheme. Note that $a_m^{\mathrm{g}}(R)$, $b_m^{\mathrm{g}}(R)$, and $d^{\mathrm{g}}(R)$ are functions of R. Using (3.16), one can write

$$g_1(R,\omega) \approx e^{-\mathrm{j}\omega R/c_1}\left[\frac{1}{4\pi R} + d^{\mathrm{g}}(R) + \sum_{m=1}^{N_{\mathrm{p}}^{\mathrm{VF}}} \frac{b_m^{\mathrm{g}}(R)}{j\omega + a_m^{\mathrm{g}}(R)}\right]. \tag{3.17}$$

Inverse Fourier transforming (3.17) yields

$$g_1(R,t) \approx \frac{\delta(\tau_1)}{4\pi R} + d^{\mathrm{g}}(R)\delta(\tau_1) + \sum_{m=1}^{N_{\mathrm{p}}^{\mathrm{VF}}} b_m^{\mathrm{g}}(R)u(\tau_1)e^{-a_m^{\mathrm{g}}(R)\tau_1}. \tag{3.18}$$

where $\tau_1 = t - R/c_1$ is the delay representing the time retardation due to the finite speed of light. A similar method is used to obtain an expression for $\partial_R g_1(R,t)$ from the samples of $\partial_R g_1(R,\omega)$. Note that $\partial_R g_1(R,\omega) = -e^{-\mathrm{j}k_1 R}/(4\pi R)\,[\mathrm{j}k_1 + 1/R]$. Extracting the singularity and the phase, and applying FRVF scheme to the samples of the remaining function at $\omega_i \in 2\pi[f_{\min}^{\mathrm{VF}}, f_{\max}^{\mathrm{VF}}]$, $i = 1, ..., N_\omega^{\mathrm{VF}}$ yield

$$
\begin{aligned}
&e^{\mathrm{j}\omega R/c_1}\left[\partial_R g_1(R,\omega) + \left(\frac{\mathrm{j}\omega}{c_1 R} + \frac{1}{R^2}\right)\frac{e^{-\mathrm{j}\omega R/c_1}}{4\pi}\right] = \\
&-\frac{e^{-\mathrm{j}(k_1 R - \omega R/c_1)}}{4\pi}\left(\frac{\mathrm{j}k_1}{R} + \frac{1}{R^2}\right) + \frac{1}{4\pi R^2} + \frac{\mathrm{j}\omega}{4\pi c_1 R} \\
&\approx d^{\mathrm{gR}}(R) + j\omega f^{\mathrm{gR}}(R) + \sum_{m=1}^{N_{\mathrm{p}}^{\mathrm{VF}}} \frac{b_m^{\mathrm{gR}}(R)}{j\omega + a_m^{\mathrm{gR}}(R)}.
\end{aligned}
\tag{3.19}
$$

Here, $\{a_m^{\mathrm{gR}}(R), b_m^{\mathrm{gR}}(R)\}$ are the pole/residue pairs, $d^{\mathrm{gR}}(R)$ is the constant term (with respect to frequency dependence) and $f^{\mathrm{gR}}(R)$ is the coefficient of the linear term generated by the FRVF scheme. Using (3.19), one can write

$$
\begin{aligned}
\partial_R g_1(R,\omega) \approx e^{-\mathrm{j}\omega R/c_1}\Bigg[&\mathrm{j}\omega\left(f^{\mathrm{gR}}(R) - \frac{1}{4\pi c_1 R}\right) \\
&+ d^{\mathrm{gR}}(R) - \frac{1}{4\pi R^2} + \sum_{m=1}^{N_{\mathrm{p}}^{\mathrm{VF}}} \frac{b_m^{\mathrm{gR}}(R)}{\mathrm{j}\omega + a_m^{\mathrm{gR}}(R)}\Bigg].
\end{aligned}
\tag{3.20}
$$

Inverse Fourier transforming (3.20) yields

$$
\begin{aligned}
\partial_R g_1(R,t) \approx{}& \delta'(\tau_1)\left(f^{\mathrm{gR}}(R) - \frac{1}{4\pi c_1 R}\right) \\
&+ \delta(\tau_1)\left(d^{\mathrm{gR}}(R) - \frac{1}{4\pi R^2}\right) + \sum_{m=1}^{N_{\mathrm{p}}^{\mathrm{VF}}} b_m^{\mathrm{gR}}(R) u(\tau_1) e^{-a_m^{\mathrm{gR}}(R)\tau_1}.
\end{aligned}
\tag{3.21}
$$

One could assume $\partial_R g_1(R,t)$ could be directly obtained by taking the derivative of (3.18) with respect to R, but this is not possible since the coefficients $a_m^{\mathrm{gR}}(R)$, $b_m^{\mathrm{gR}}(R)$, $d^{\mathrm{gR}}(R)$, and $f^{\mathrm{gR}}(R)$ depend on R and are obtained numerically using the

FRVF (i.e., they do not have closed-form expressions). Also, the causality of $g_1(R,t)$ and $\partial_R g_1(R,t)$ is ensured by enforcing $a_m^{\mathrm{g}}(R) > 0$ and $a_m^{\mathrm{gR}}(R) > 0$ during the execution of the FRVF scheme.

3.2.4 Discretization and MOT Scheme

To numerically solve the TD-PMCHWT-SIE in Eqs. (3.1) and (3.2), first S is discretized into triangular patches. Then $\mathbf{J}(\mathbf{r},t)$ and $\mathbf{M}(\mathbf{r},t)$ are expanded in space and time as

$$\mathbf{J}(\mathbf{r},t) = \sum_{j'=1}^{N_{\mathrm{t}}} \sum_{n'=1}^{N_{\mathrm{s}}} J_{n'}(j'\Delta t)\mathbf{f}_{n'}(\mathbf{r})T_{j'}(t) = \sum_{j'=1}^{N_{\mathrm{t}}} \sum_{n'=1}^{N_{\mathrm{s}}} \{\bar{I}_{j'}^{\mathrm{J}}\}_{n'}\mathbf{f}_{n'}(\mathbf{r})T_{j'}(t) \tag{3.22}$$

$$\mathbf{M}(\mathbf{r},t) = \sum_{j'=1}^{N_{\mathrm{t}}} \sum_{n'=1}^{N_{\mathrm{s}}} M_{n'}(j'\Delta t)\mathbf{f}_{n'}(\mathbf{r})T_{j'}(t) = \sum_{j'=1}^{N_{\mathrm{t}}} \sum_{n'=1}^{N_{\mathrm{s}}} \{\bar{I}_{j'}^{\mathrm{M}}\}_{n'}\mathbf{f}_{n'}(\mathbf{r})T_{j'}(t). \tag{3.23}$$

Here, $\mathbf{f}_{n'}(\mathbf{r})$ represent the well-known RWG functions [40], $T_{j'}(t) = T(t - j'\Delta t)$ are the shifted Lagrange interpolation functions [23, 33], Δt is the time step size, $\{\bar{I}_{j'}^{\mathrm{J}}\}_{n'} = J_{n'}(j'\Delta t)$ and $\{\bar{I}_{j'}^{\mathrm{M}}\}_{n'} = M_{n'}(j'\Delta t)$ are the unknown coefficients, and N_{s} and N_{t} are the total numbers of spatial basis functions on S and the time steps, respectively. It should be mentioned here that each one of $\mathbf{f}_{n'}(\mathbf{r})$ is defined on a pair of triangular patches with support $S_{n'}$ and the Lagrange interpolation functions $T(t)$ are piecewise continuous polynomial functions defined on support $[-\Delta t, d\Delta t]$, where d is the order of $T(t)$. Inserting Eqs. (3.22) and (3.23) into Eqs. (3.1) and (3.2) and testing the resulting equations with $\hat{\mathbf{n}}(\mathbf{r}) \times \mathbf{f}_n(\mathbf{r})\delta(t - j\Delta t)$, $n = 1, ..., N_{\mathrm{s}}$, yield a system of equations:

$$\begin{bmatrix} \bar{\bar{Z}}_0^{\mathrm{JJ}} & \bar{\bar{Z}}_0^{\mathrm{JM}} \\ -\bar{\bar{Z}}_0^{\mathrm{JM}} & \bar{\bar{Z}}_0^{\mathrm{MM}} \end{bmatrix} \begin{bmatrix} \bar{I}_j^{\mathrm{J}} \\ \bar{I}_j^{\mathrm{M}} \end{bmatrix} = \begin{bmatrix} \bar{V}_j^{\mathrm{J}} \\ \bar{V}_j^{\mathrm{M}} \end{bmatrix} - \sum_{j'=1}^{j-1} \begin{bmatrix} \bar{\bar{Z}}_{j-j'}^{\mathrm{JJ}} & \bar{\bar{Z}}_{j-j'}^{\mathrm{JM}} \\ -\bar{\bar{Z}}_{j-j'}^{\mathrm{JM}} & \bar{\bar{Z}}_{j-j'}^{\mathrm{MM}} \end{bmatrix} \begin{bmatrix} \bar{I}_{j'}^{\mathrm{J}} \\ \bar{I}_{j'}^{\mathrm{M}} \end{bmatrix}. \tag{3.24}$$

Here, vectors $\bar{V}_j^{\mathrm{J}}$ and $\bar{V}_j^{\mathrm{M}}$ of size $N_{\mathrm{s}} \times 1$ store the tested incident fields and their elements are given by

$$\{\bar{V}_j^{\mathrm{J}}\}_n = -\big\langle \mathbf{f}_n(\mathbf{r}), \partial_t \mathbf{E}_0^{\mathrm{inc}}(\mathbf{r},t)\big\rangle_{t=j\Delta t} \tag{3.25}$$

$$\{\bar{V}_j^{\mathrm{M}}\}_n = -\big\langle \mathbf{f}_n(\mathbf{r}), \partial_t \mathbf{H}_0^{\mathrm{inc}}(\mathbf{r},t)\big\rangle_{t=j\Delta t}. \tag{3.26}$$

Note that here $\langle \mathbf{f}_n(\mathbf{r}), \mathbf{X}(\mathbf{r},t)\rangle_{t=j\Delta t} = \int_{S_n} \mathbf{f}_n(\mathbf{r}) \cdot \mathbf{X}(\mathbf{r},t) ds|_{t=j\Delta t}$ represents the inner product operation due to spatial testing. The elements of the matrices $\bar{\bar{Z}}_{j-j'}^{\mathrm{JJ}}$, $\bar{\bar{Z}}_{j-j'}^{\mathrm{JM}}$, and $\bar{\bar{Z}}_{j-j'}^{\mathrm{MM}}$ of size $N_{\mathrm{s}} \times N_{\mathrm{s}}$ are given by

$$\{\bar{\bar{Z}}_{j-j'}^{\mathrm{JJ}}\}_{n,n'} = \{\bar{\bar{Z}}_{j-j'}^{\mathrm{JJ},0}\}_{n,n'} + \{\bar{\bar{Z}}_{j-j'}^{\mathrm{JJ},1}\}_{n,n'} \tag{3.27}$$

$$\{\bar{\bar{Z}}_{j-j'}^{\mathrm{JM}}\}_{n,n'} = \{\bar{\bar{Z}}_{j-j'}^{\mathrm{JM},0}\}_{n,n'} + \{\bar{\bar{Z}}_{j-j'}^{\mathrm{JM},1}\}_{n,n'} \tag{3.28}$$

$$\{\bar{\bar{Z}}_{j-j'}^{\mathrm{MM}}\}_{n,n'} = \{\bar{\bar{Z}}_{j-j'}^{\mathrm{MM},0}\}_{n,n'} + \{\bar{\bar{Z}}_{j-j'}^{\mathrm{MM},1}\}_{n,n'} \tag{3.29}$$

where

$$\begin{aligned}\{\bar{\bar{Z}}_{j-j'}^{\mathrm{JJ},0}\}_{n,n'} = &-\mu_0 \langle \mathbf{f}_n(\mathbf{r}), \mathcal{L}_0\{\mathbf{f}_{n'}(\mathbf{r}) T_{j'}(t)\}\rangle_{t=j\Delta t} \\ &+\frac{1}{\varepsilon_0}\langle \mathbf{f}_n(\mathbf{r}), \mathcal{Q}_0\{\mathbf{f}_{n'}(\mathbf{r}) T_{j'}(t)\}\rangle_{t=j\Delta t}\end{aligned} \tag{3.30}$$

$$\{\bar{\bar{Z}}_{j-j'}^{\mathrm{JM},0}\}_{n,n'} = -\langle \mathbf{f}_n(\mathbf{r}), \mathcal{K}_0\{\mathbf{f}_{n'}(\mathbf{r}) T_{j'}(t)\}\rangle_{t=j\Delta t} \tag{3.31}$$

$$\{\bar{\bar{Z}}_{j-j'}^{\mathrm{MM},0}\}_{n,n'} = \frac{\varepsilon_0}{\mu_0}\{\bar{\bar{Z}}_{j-j'}^{\mathrm{JJ},0}\}_{n,n'} \tag{3.32}$$

$$\begin{aligned}\{\bar{\bar{Z}}_{j-j'}^{\mathrm{JJ},1}\}_{n,n'} = &-\mu_1 \langle \mathbf{f}_n(\mathbf{r}), \mathcal{L}_1\{\mathbf{f}_{n'}(\mathbf{r}) T_{j'}(t)\}\rangle_{t=j\Delta t} \\ &+ \frac{1}{\varepsilon_1^{\infty}}\langle \mathbf{f}_n(\mathbf{r}), \mathcal{Q}_1\{\mathbf{f}_{n'}(\mathbf{r}) T_{j'}(t)\}\rangle_{t=j\Delta t} \\ &+ \langle \mathbf{f}_n(\mathbf{r}), \mathcal{Q}_1\{\bar{\gamma}_1(t) * \mathbf{f}_{n'}(\mathbf{r}) T_{j'}(t)\}\rangle_{t=j\Delta t}\end{aligned} \tag{3.33}$$

$$\{\bar{\bar{Z}}^{\mathrm{JM},1}_{j-j'}\}_{n,n'} = -\langle \mathbf{f}_n(\mathbf{r}), \mathcal{K}_1\{\mathbf{f}_{n'}(\mathbf{r})T_{j'}(t)\}\rangle_{t=j\Delta t} \tag{3.34}$$

$$\begin{aligned}\{\bar{\bar{Z}}^{\mathrm{MM},1}_{j-j'}\}_{n,n'} = &-\varepsilon_1^{\infty}\langle \mathbf{f}_n(\mathbf{r}), \mathcal{L}_1\{\mathbf{f}_{n'}(\mathbf{r})T_{j'}(t)\}\rangle_{t=j\Delta t} \\ &- \langle \mathbf{f}_n(\mathbf{r}), \mathcal{L}_1\{\gamma_1(t) * \mathbf{f}_{n'}(\mathbf{r})T_{j'}(t)\}\rangle_{t=j\Delta t} \\ &+ \frac{1}{\mu_1}\langle \mathbf{f}_n(\mathbf{r}), \mathcal{Q}_1\{\mathbf{f}_{n'}(\mathbf{r})T_{j'}(t)\}\rangle_{t=j\Delta t}.\end{aligned} \tag{3.35}$$

Here, $\bar{\bar{Z}}^{\mathrm{JJ},p}_{j-j'}$, $\bar{\bar{Z}}^{\mathrm{JM},p}_{j-j'}$, and $\bar{\bar{Z}}^{\mathrm{MM},p}_{j-j'}$, $p \in \{0,1\}$, correspond to contributions from the scattered fields generated in the background medium ($p = 0$) and inside the nanostructure ($p = 1$). Their entries, which are given by Eqs. (3.30)-(3.35), are computed using the schemes described in Section 3.2.5. Once $\bar{\bar{Z}}^{\mathrm{JJ}}_{j-j'}$, $\bar{\bar{Z}}^{\mathrm{JM}}_{j-j'}$, and $\bar{\bar{Z}}^{\mathrm{MM}}_{j-j'}$ are constructed, unknown vectors $[\bar{I}^{\mathrm{J}}_j \ \bar{I}^{\mathrm{M}}_j]^T$, $j = 1, ..., N_{\mathrm{t}}$, are obtained recursively by time marching, as described next [22–25, 29, 30, 32, 33, 53–55]. First, $[\bar{I}^{\mathrm{J}}_1 \ \bar{I}^{\mathrm{M}}_1]^T$ at time $t = \Delta t$ is found by solving (3.24) with right-hand side $[\bar{V}^{\mathrm{J}}_1 \ \bar{V}^{\mathrm{M}}_1]^T$ ($j = 1$). $[\bar{I}^{\mathrm{J}}_1 \ \bar{I}^{\mathrm{M}}_1]^T$ are then used to compute the scattered fields at time $t = 2\Delta t$, which are added to the tested incident fields $[\bar{V}^{\mathrm{J}}_2 \ \bar{V}^{\mathrm{M}}_2]^T$ to yield the right-hand side of (3.24). $[\bar{I}^{\mathrm{J}}_2 \ \bar{I}^{\mathrm{M}}_2]^T$ is found by solving (3.24) with this right-hand side ($j = 2$). Then, $[\bar{I}^{\mathrm{J}}_1 \ \bar{I}^{\mathrm{M}}_1]^T$ and $[\bar{I}^{\mathrm{J}}_2 \ \bar{I}^{\mathrm{M}}_2]^T$ are used to compute the scattered fields at time $t = 3\Delta t$, which together with $[\bar{V}^{\mathrm{J}}_3 \ \bar{V}^{\mathrm{M}}_3]^T$ form the right-hand side and permit the computation of $[\bar{I}^{\mathrm{J}}_3 \ \bar{I}^{\mathrm{M}}_3]^T$, and so on. The computational cost of this time marching scheme is dominated by that of computing the scattered fields, i.e., the discrete summation on the right-hand side of (3.24). (See Section 3.2.6)

3.2.5 Computation of the Matrix Entries

Contributions from the Background Medium (p=0)

As described in Section 3.2.3, the Green function in the background medium, i.e., for $p = 0$, $g_0(R,t) = \delta(t - R/c_0)/(4\pi R)$. Inserting this in the expressions of $\{\bar{\bar{Z}}^{\mathrm{JJ},0}_{j-j'}\}_{n,n'}$, $\{\bar{\bar{Z}}^{\mathrm{JM},0}_{j-j'}\}_{n,n'}$, and $\{\bar{\bar{Z}}^{\mathrm{MM},0}_{j-j'}\}_{n,n'}$ in Eqs. (3.30)-(3.32) and using the definitions of integral

operators $\mathcal{L}_0\{\cdot\}$, $\mathcal{Q}_0\{\cdot\}$, and $\mathcal{K}_0\{\cdot\}$ in Eqs. (3.7)-(3.9), one can obtain

$$\begin{aligned}\{\bar{\bar{Z}}^{\mathrm{MM},0}_{j-j'}\}_{n,n'} &= \frac{\varepsilon_0}{\mu_0}\{\bar{\bar{Z}}^{\mathrm{JJ},0}_{j-j'}\}_{n,n'} = \\ &- \frac{\varepsilon_0}{4\pi}\int\limits_{S_n}\mathbf{f}_n(\mathbf{r})\cdot\int\limits_{S_{n'}}\frac{\mathbf{f}_{n'}(\mathbf{r}')\,\partial_t^2 T_{j'}(t)|_{t=j\Delta t-R/c_0}}{R}ds'ds \\ &- \frac{1}{4\pi\mu_0}\int\limits_{S_n}\nabla\cdot\mathbf{f}_n(\mathbf{r})\int\limits_{S_{n'}}\frac{\nabla'\cdot\mathbf{f}_{n'}(\mathbf{r}')T_{j'}(j\Delta t-R/c_0)}{R}ds'ds\end{aligned} \tag{3.36}$$

$$\begin{aligned}&\{\bar{\bar{Z}}^{\mathrm{JM},0}_{j-j'}\}_{n,n'} = \frac{1}{4\pi} \\ &\int\limits_{S_n}\mathbf{f}_n(\mathbf{r})\cdot\int\limits_{S_{n'}}\frac{\hat{\mathbf{R}}\times\mathbf{f}_{n'}(\mathbf{r}')}{R}\left[\frac{\partial_{t'}^2 T_{j'}(t')}{c_0}+\frac{\partial_t T_{j'}(t')}{R}\right]_{t'=j\Delta t-R/c_0}ds'ds.\end{aligned} \tag{3.37}$$

In (3.37), $\hat{\mathbf{R}} = (\mathbf{r}-\mathbf{r}')/R$. The surface integrals present in Eqs. (3.36) and (3.37) are computed using numerical quadrature [62] with proper singularity treatment [63]. One can also use semi-analytical expressions provided in [55, 64–66].

Contributions from the Plasmonic Medium (p=1)

These require computation of two types of convolutions.

Type-1 Convolutions: Type-1 refers to convolutions of $g_1(R,t)$ with $\nabla\cdot\mathbf{f}_{n'}(\mathbf{r})T_{j'}(t)$ and $\mathbf{f}_{n'}(\mathbf{r})\partial_t^2 T_{j'}(t)$ and the convolution of $\partial_R g_1(R,t)$ with $\mathbf{f}_{n'}(\mathbf{r})\partial_t T_{j'}(t)$. Let $\mathcal{C}_{\mathrm{T}}(R,t)$, $\mathcal{C}(R,t)$, and $\mathcal{C}_{\mathrm{R}}(R,t)$ denote the following temporal convolutions:

$$\mathcal{C}_{\mathrm{T}}(R,t) = g_1(R,t) * \partial_t^2 T_{j'}(t) \tag{3.38}$$

$$\mathcal{C}(R,t) = g_1(R,t) * T_{j'}(t) \tag{3.39}$$

$$\mathcal{C}_{\mathrm{R}}(R,t) = \partial_R g_1(R,t) * \partial_t T_{j'}(t). \tag{3.40}$$

Using the definitions in Eqs. (3.38)-(3.40), one can rewrite $\langle\mathbf{f}_n(\mathbf{r}),\mathcal{L}_1\{\mathbf{f}_{n'}(\mathbf{r})T_{j'}(t)\}\rangle_{t=j\Delta t}$, $\langle\mathbf{f}_n(\mathbf{r}),\mathcal{Q}_1\{\mathbf{f}_{n'}(\mathbf{r})T_{j'}(t)\}\rangle_{t=j\Delta t}$, and $\langle\mathbf{f}_n(\mathbf{r}),\mathcal{K}_1\{\mathbf{f}_{n'}(\mathbf{r})T_{j'}(t)\}\rangle_{t=j\Delta t}$, which are needed to

compute $\{\bar{\bar{Z}}^{\mathrm{JJ},1}_{j-j'}\}_{n,n'}$, $\{\bar{\bar{Z}}^{\mathrm{JM},1}_{j-j'}\}_{n,n'}$, and $\{\bar{\bar{Z}}^{\mathrm{MM},1}_{j-j'}\}_{n,n'}$:

$$\langle \mathbf{f}_n(\mathbf{r}), \mathcal{L}_1\{\mathbf{f}_{n'}(\mathbf{r})T_{j'}(t)\}\rangle_{t=j\Delta t} = \int\limits_{S_n} \mathbf{f}_n(\mathbf{r}) \cdot \int\limits_{S_{n'}} \mathcal{C}_{\mathrm{T}}(R,t)\mathbf{f}_{n'}(\mathbf{r}')ds'ds\Big|_{t=j\Delta t} \tag{3.41}$$

$$\langle \mathbf{f}_n(\mathbf{r}), \mathcal{Q}_1\{\mathbf{f}_{n'}(\mathbf{r})T_{j'}(t)\}\rangle_{t=j\Delta t} = -\int\limits_{S_n} \nabla\cdot\mathbf{f}_n(\mathbf{r}) \int\limits_{S_{n'}} \mathcal{C}(R,t)\nabla'\cdot\mathbf{f}_{n'}(\mathbf{r}')ds'ds\Big|_{t=j\Delta t} \tag{3.42}$$

$$\langle \mathbf{f}_n(\mathbf{r}), \mathcal{K}_1\{\mathbf{f}_{n'}(\mathbf{r})T_{j'}(t)\}\rangle_{t=j\Delta t} = \int\limits_{S_n} \mathbf{f}_n(\mathbf{r}) \cdot \int\limits_{S_{n'}} \hat{\mathbf{R}}\times\mathbf{f}_{n'}(\mathbf{r}')\mathcal{C}_{\mathrm{R}}(R,t)ds'ds\Big|_{t=j\Delta t}. \tag{3.43}$$

The surface integrals in Eqs. (3.41)-(3.43) are computed using numerical quadrature [62]. For every quadrature point pair, $\mathcal{C}_{\mathrm{T}}(R,t)$, $\mathcal{C}(R,t)$, and $\mathcal{C}_{\mathrm{R}}(R,t)$ have to be computed. Their explicit expressions are obtained by inserting Eqs. (3.18) and (3.21) into Eqs. (3.41)-(3.43):

$$\begin{aligned}\mathcal{C}_{\mathrm{T}}(R,t) = &\left[d^{\mathrm{g}}(R) + \frac{1}{4\pi R}\right]\partial_{t'}^2 T(t')\Big|_{t'=t-j'\Delta t-R/c_1} \\ &+ \sum_{m=1}^{N_{\mathrm{p}}^{\mathrm{VF}}} b_m^{\mathrm{g}}(R) \int\limits_{-\Delta t}^{\min(t-j'\Delta t-R/c_1,d\Delta t)} u(t-t'-j'\Delta t-R/c_1)e^{-a_m^{\mathrm{g}}(R)(t-t'-j'\Delta t-R/c_1)}\partial_{t'}^2 T(t')dt'\end{aligned} \tag{3.44}$$

$$\begin{aligned}\mathcal{C}(R,t) = &\left[d^{\mathrm{g}}(R) + \frac{1}{4\pi R}\right] T(t-j'\Delta t-R/c_1) \\ &+ \sum_{m=1}^{N_{\mathrm{p}}^{\mathrm{VF}}} b_m^{\mathrm{g}}(R) \int\limits_{-\Delta t}^{\min(t-j'\Delta t-R/c_1,d\Delta t)} u(t-t'-j'\Delta t-R/c_1)e^{-a_m^{\mathrm{g}}(R)(t-t'-j'\Delta t-R/c_1)}T(t')dt'\end{aligned} \tag{3.45}$$

$$\mathcal{C}_{\mathrm{R}}(R,t) = \left[f^{g_{\mathrm{R}}}(R) - \frac{1}{4\pi R c_1}\right] \partial_{t'}^2 T(t')\Big|_{t'=t-j'\Delta t-R/c_1} \tag{3.46}$$
$$+ \left[d^{g_{\mathrm{R}}}(R) - \frac{1}{4\pi R^2}\right] \partial_{t'} T(t')|_{t'=t-j'\Delta t-R/c_1}$$
$$+ \sum_{m=1}^{N_{\mathrm{p}}^{\mathrm{VF}}} b_m^{g_{\mathrm{R}}}(R) \int_{-\Delta t}^{\min(t-j'\Delta t-R/c_1, d\Delta t)} u(t-t'-j'\Delta t-R/c_1) e^{-a_m^{g_{\mathrm{R}}}(R)(t-t'-j'\Delta t-R/c_1)} \partial_{t'} T(t') dt'.$$

For every quadrature point pair, $\mathcal{C}_{\mathrm{T}}(R,t)$, $\mathcal{C}(R,t)$, and $\mathcal{C}_{\mathrm{R}}(R,t)$ are computed using Eqs. (3.44)-(3.46). For these computations, terms involving $1/R$ and $1/R^2$ are treated carefully using the proper singularity extraction schemes [63]. The boundaries of the time integrals are determined using the support of $T(t)$, $\partial_t T(t)$, and $\partial_t^2 T(t)$ and the unit step function $u(t-t'-j'\Delta t-R/c_1)$. It should also be noted here that these integrals are computed using closed-form expressions since $T(t)$, $\partial_t T(t)$, and $\partial_t^2 T(t)$ consist of polynomial functions [56].

Type-2 Convolutions: Type-2 refers to the convolutions of $g_1(R,t)$ with $\nabla \cdot \mathbf{f}_{n'}(\mathbf{r})\bar{\gamma}_1(t) * T_{j'}(t)$ and $\mathbf{f}_{n'}(\mathbf{r})\gamma_1(t) * \partial_t^2 T_{j'}(t)$. Note the presence of the extra temporal convolution (in comparison with type-1 convolutions). Let $\mathcal{D}(R,t)$ and $\mathcal{D}_{\mathrm{T}}(R,t)$ denote the following temporal convolutions:

$$\mathcal{D}(R,t) = g_1(R,t) * \bar{\gamma}_1(t) * T_{j'}(t) \tag{3.47}$$

$$\mathcal{D}_{\mathrm{T}}(R,t) = g_1(R,t) * \gamma_1(t) * \partial_t^2 T_{j'}(t) = \partial_t^2 g_1(R,t) * \gamma_1(t) * T_{j'}(t). \tag{3.48}$$

Using the definitions in Eqs. (3.47) and (3.48), one can rewrite the expressions of $\langle \mathbf{f}_n(\mathbf{r}), \mathcal{Q}_1\{\bar{\gamma}_1(t) * \mathbf{f}_{n'}(\mathbf{r}) T_{j'}(t)\}\rangle_{t=j\Delta t}$, and $\langle \mathbf{f}_n(\mathbf{r}), \mathcal{L}_1\{\gamma_1(t) * \mathbf{f}_{n'}(\mathbf{r}) T_{j'}(t)(t)\}\rangle_{t=j\Delta t}$, which

are needed to compute $\{\bar{\bar{Z}}^{\mathrm{JJ},1}_{j-j'}\}_{n,n'}$ and $\{\bar{\bar{Z}}^{\mathrm{MM},1}_{j-j'}\}_{n,n'}$:

$$\langle \mathbf{f}_n(\mathbf{r}), \mathcal{Q}_1\{\bar{\gamma}_1(t) * \mathbf{f}_{n'}(\mathbf{r})T_{j'}(t)\}\rangle_{t=j\Delta t} = -\int\limits_{S_n} \nabla\cdot\mathbf{f}_n(\mathbf{r}) \int\limits_{S_{n'}} \mathcal{D}(R,t)\nabla'\cdot\mathbf{f}_{n'}(\mathbf{r}')ds'ds\Big|_{t=j\Delta t} \tag{3.49}$$

$$\langle \mathbf{f}_n(\mathbf{r}), \mathcal{L}_1\{\gamma_1(t) * \mathbf{f}_{n'}(\mathbf{r})T_{j'}(t)\}\rangle_{t=j\Delta t} = \int\limits_{S_n} \mathbf{f}_n(\mathbf{r})\cdot \int\limits_{S_{n'}} \mathcal{D}_{\mathrm{T}}(R,t)\mathbf{f}_{n'}(\mathbf{r}')ds'ds\Big|_{t=j\Delta t}. \tag{3.50}$$

The surface integrals in Eqs. (3.49) and (3.50) are computed using numerical quadrature [62]. But this computation can be done very efficiently by making use of type-1 convolutions that are already computed using the same quadrature points. In other words, one can represent the inner products $\langle \mathbf{f}_n(\mathbf{r}), \mathcal{Q}_1\{\bar{\gamma}_1(t) * \mathbf{f}_{n'}(\mathbf{r})T_{j'}(t)\}\rangle_{t=j\Delta t}$ and $\langle \mathbf{f}_n(\mathbf{r}), \mathcal{L}_1\{\gamma_1(t) * \mathbf{f}_{n'}(\mathbf{r})T_{j'}(t)\}\rangle_{t=j\Delta t}$ (type-2 convolutions) in terms of the inner products $\langle \mathbf{f}_n(\mathbf{r}), \mathcal{Q}_1\{\mathbf{f}_{n'}(\mathbf{r})T_{j'}(t)\}\rangle_{t=j\Delta t}$ and $\langle \mathbf{f}_n(\mathbf{r}), \mathcal{L}_1\{\mathbf{f}_{n'}(\mathbf{r})T_{j'}(t)\}\rangle_{t=j\Delta t}$ (type-1 convolutions). This is described next. Note that convolutions $\mathcal{F}_{j'}(t) = \bar{\gamma}_1(t) * T_{j'}(t)$ and $\mathcal{F}^{\mathrm{T}}_{j'}(t) = \gamma_1(t) * T_{j'}(t)$ do not depend on space but only on the material properties. Let $\mathcal{F}_{j'}(t)$ and $\mathcal{F}^{\mathrm{T}}_{j'}(t)$ be discretized using the temporal basis function $T_{l'}(t)$ as:

$$\mathcal{F}_{j'}(t) = \bar{\gamma}_1(t) * T_{j'}(t) \approx \sum_{l'=1}^{N_{\mathrm{t}}} F_{l'-j'}T_{l'}(t) \tag{3.51}$$

$$\mathcal{F}^{\mathrm{T}}_{j'}(t) = \gamma_1(t) * T_{j'}(t) \approx \sum_{l'=1}^{N_{\mathrm{t}}} F^{\mathrm{T}}_{l'-j'}T_{l'}(t) \tag{3.52}$$

where $F_{l'-j'}$ and $F^{\mathrm{T}}_{l'-j'}$ are the expansion coefficients. To find them, Eqs. (3.51) and (3.52) are tested at times $s\Delta t$, where s is an integer. Using the fact that $T([s-l']\Delta t) = 1$ only when $s = l'$ and $T([s-l']\Delta t) = 0$ otherwise, and inserting the expressions for $\gamma(t)$ and $\bar{\gamma}(t)$ from Eqs. (3.14) and (3.15) into the resulting equations,

one can obtain

$$F_{l'-j'} = \mathcal{F}_{j'}(l'\Delta t) = \bar{\gamma}_1(t) * T_{j'}(t)\Big|_{t=l'\Delta t} = \tag{3.53}$$
$$\int_{-\Delta t}^{\min(l'-j',d)\Delta t} \bar{\gamma}_1([l'-j']\Delta t - t')T(t')dt' =$$
$$\sum_{m=1}^{N_{\mathrm{p}}^{\mathrm{VF}}} b_m^{\bar{\epsilon}} \int_{-\Delta t}^{\min(l'-j',d)\Delta t} u([l'-j']\Delta t - t')e^{-a_m^{\bar{\epsilon}}([l'-j']\Delta t - t')}T(t')dt'$$

$$F_{l'-j'}^{\mathrm{T}} = \mathcal{F}_{j'}^{\mathrm{T}}(l'\Delta t) = \gamma_1(t) * T_{j'}(t)\big|_{t=l'\Delta t} = \tag{3.54}$$
$$\int_{-\Delta t}^{\min(l'-j',d)\Delta t} \gamma_1([l'-j']\Delta t - t')T(t')dt' =$$
$$\sum_{m=1}^{N_{\mathrm{p}}^{\mathrm{VF}}} b_m^{\epsilon} \int_{-\Delta t}^{\min(l'-j',d)\Delta t} u([l'-j']\Delta t - t')e^{-a_m^{\epsilon}([l'-j']\Delta t - t')}T(t')dt'.$$

Note that the boundaries of the time integrals in Eqs. (3.53) and (3.54) are determined using the supports of $T(t)$ and the unit step function $u([l'-j']\Delta t - t')$. These integrals are computed using closed-form expressions since $T(t)$ consists of polynomial functions, respectively [56]. It should also be noted here $F_{l'-j'} = 0$ and $F_{l'-j'}^{\mathrm{T}} = 0$ for $j' \geq l'+1$. Inserting Eqs. (3.51) and (3.52) into Eqs. (3.47) and (3.48), respectively, yields

$$\mathcal{D}(R,t) = g_1(R,t) * \mathcal{F}_{l'-j'}(t) \approx \sum_{l'=1}^{N_{\mathrm{t}}} F_{l'-j'} g_1(R,t) * T_{l'}(t) \tag{3.55}$$

$$\mathcal{D}_{\mathrm{T}}(R,t) = \partial_t^2 g_1(R,t) * \mathcal{F}_{l'-j'}^{\mathrm{T}}(t) \approx \tag{3.56}$$
$$\sum_{l'=1}^{N_{\mathrm{t}}} F_{l'-j'}^{\mathrm{T}} \partial_t^2 g_1(R,t) * T_{l'}(t) = \sum_{l'=1}^{N_{\mathrm{t}}} F_{l'-j'}^{\mathrm{T}} g_1(R,t) * \partial_t^2 T_{l'}(t).$$

Finally, inserting Eqs. (3.55) and (3.56) into Eqs. (3.49) and (3.50), respectively,

yields:

$$\langle \mathbf{f}_n(\mathbf{r}), \mathcal{Q}_1\{\bar{\gamma}_1(t) * \mathbf{f}_{n'}(\mathbf{r})T_{j'}(t)\}\rangle_{t=j\Delta t} = \tag{3.57}$$
$$-\int_{S_n} \nabla\cdot\mathbf{f}_n(\mathbf{r}) \int_{S_{n'}} \left[\sum_{l'=1}^{N_\mathrm{t}} F_{l'-j'} g_1(R,t) * T_{l'}(t)\right] \nabla'\cdot\mathbf{f}_{n'}(\mathbf{r}')ds'ds\Big|_{t=j\Delta t} =$$
$$\sum_{l'=1}^{N_\mathrm{t}} \langle \mathbf{f}_n(\mathbf{r}), \mathcal{Q}_1\{\mathbf{f}_{n'}(\mathbf{r})T_{l'}(t)\}\rangle_{t=j\Delta t} F_{l'-j'}$$

$$\langle \mathbf{f}_n(\mathbf{r}), \mathcal{L}_1\{\gamma_1(t) * \mathbf{f}_{n'}(\mathbf{r})T_{j'}(t)\}\rangle_{t=j\Delta t} \tag{3.58}$$
$$= \int_{S_n} \mathbf{f}_n(\mathbf{r}) \cdot \int_{S_{n'}} \left[\sum_{l'=1}^{N_\mathrm{t}} F^{\mathrm{T}}_{l'-j'} g_1(R,t) * \partial_t^2 T_{l'}(t)\right] \mathbf{f}_{n'}(\mathbf{r}')ds'ds\Big|_{t=j\Delta t} =$$
$$= \sum_{l'=1}^{N_\mathrm{t}} \langle \mathbf{f}_n(\mathbf{r}), \mathcal{L}_1\{\mathbf{f}_{n'}(\mathbf{r})T_{l'}(t)\}\rangle_{t=j\Delta t} F^{\mathrm{T}}_{l'-j'}.$$

Above equations show that type-2 convolutions $\langle \mathbf{f}_n(\mathbf{r}), \mathcal{Q}_1\{\bar{\gamma}_1(t)*\mathbf{f}_{n'}(\mathbf{r})T_{j'}(t)\}\rangle_{t=j\Delta t}$ and $\langle \mathbf{f}_n(\mathbf{r}), \mathcal{L}_1\{\gamma_1(t)*\mathbf{f}_{n'}(\mathbf{r})T_{j'}(t)\}\rangle_{t=j\Delta t}$ can be easily computed using type-1 convolutions $\langle \mathbf{f}_n(\mathbf{r}), \mathcal{Q}_1\{\mathbf{f}_{n'}(\mathbf{r})T_{l'}(t)\}\rangle_{t=j\Delta t}$ and $\langle \mathbf{f}_n(\mathbf{r}), \mathcal{L}_1\{\mathbf{f}_{n'}(\mathbf{r})T_{l'}(t)\}\rangle_{t=j\Delta t}$.

3.2.6 Computational Complexity

In this section, computational complexity of the TD-PMCHWT-SIE solver is described step by step following the derivation of the matrix entries (Section 3.2.5) and the MOT scheme (Section 3.2.4):

(i) Computation of $\{\bar{\bar{Z}}^{\mathrm{JJ},0}_{j-j'}\}_{n,n'}$, $\{\bar{\bar{Z}}^{\mathrm{JM},0}_{j-j'}\}_{n,n'}$, and $\{\bar{\bar{Z}}^{\mathrm{MM},0}_{j-j'}\}_{n,n'}$ in Eqs. (3.36) and (3.37) scales with $O({N_\mathrm{s}}^2)$ because $g_0(R,t)$ is simply a Dirac function in time and space (no temporal tail).

(ii) Computation of type-1 convolutions in Eqs. (3.41)-(3.43) has a complexity of $O(N_\mathrm{t}{N_\mathrm{s}}^2)$ because $g_1(R,t)$ has a temporal tail.

(iii) Convolutions in Eqs. (3.53) and (3.54) depend only on the permittivity of

the plasmonic medium. Therefore $F_{l'-j'}$ and $F^{\mathrm{T}}_{l'-j'}$ are computed once and stored in the memory. Cost of computing $F_{l'-j'}$ and $F^{\mathrm{T}}_{l'-j'}$ scales with $O(N_{\mathrm{t}})$ because $\gamma_1(t)$ and $\bar{\gamma}_1(t)$ have temporal tails.

(iv) Computation of type-2 convolutions in Eqs. (3.57) and (3.58) scales with $O(N_{\mathrm{t}}{N_{\mathrm{s}}}^2)$ as a consequence of (ii) and (iii). As a result, computation of $\{\bar{\bar{Z}}^{\mathrm{JJ},1}_{j-j'}\}_{n,n'}$, $\{\bar{\bar{Z}}^{\mathrm{JM},1}_{j-j'}\}_{n,n'}$, and $\{\bar{\bar{Z}}^{\mathrm{MM},1}_{j-j'}\}_{n,n'}$ scales with $O(N_{\mathrm{t}}{N_{\mathrm{s}}}^2)$. This assumes that the results of discrete summations in Eqs. (3.57) and (3.58) are directly incorporated into the matrix elements.

Finally, the computational complexity of the MOT scheme given in Eq.(3.24) scales with $O({N_{\mathrm{t}}}^2{N_{\mathrm{s}}}^2)$. This cost can be reduced to $O(N_{\mathrm{t}}N_{\mathrm{s}}^{3/2}\log(N_{\mathrm{s}})\log(N_{\mathrm{t}}N_{\mathrm{s}})\log(N_{\mathrm{t}}))$ using FFT-based schemes [25, 30, 32–34]. In such cases, the discrete summations in Eqs. (3.57) and (3.58) should not be pre-computed into the MOT matrices but should be incorporated into time marching through the use of $\sum_{j'=1}^{l'-1} F_{l'-j'}\bar{I}^{\mathrm{J}}_{j'}$ and $\sum_{j'=1}^{l'-1} F^{\mathrm{T}}_{l'-j'}\bar{I}^{\mathrm{M}}_{j'}$. This computation can be done very efficiently using a blocked FFT scheme without impacting the computational complexity of the accelerated time marching [30]. The use of these accelerated MOT schemes reduce the computational complexity of the proposed solver to essentially that of FDTD schemes.

3.3 Numerical Results

In this section, accuracy and applicability of the proposed TD-PMCHWT-SIE solver are demonstrated through its application to the analysis of scattering from several nanostructures. In all examples, it is assumed that the nanostructure is residing in free space and excited by a plane wave with electric field

$$\mathbf{E}^{\mathrm{inc}}_0(\mathbf{r},t) = \hat{\mathbf{p}}E^{\mathrm{inc}}_0 G(t-\hat{\mathbf{k}}\cdot\mathbf{r}/c_0) \tag{3.59}$$

where $E_0^{\text{inc}} = 1$ V/m is the amplitude, $\hat{\mathbf{p}}$ is the polarization unit vector, $\hat{\mathbf{k}} = \hat{\mathbf{x}}\sin\theta^{\text{inc}}\cos\phi^{\text{inc}} + \hat{\mathbf{y}}\sin\theta^{\text{inc}}\sin\phi^{\text{inc}} + \hat{\mathbf{z}}\cos\theta^{\text{inc}}$ is the unit vector along the direction of propagation defined by the angles θ^{inc} and ϕ^{inc}, $G(t) = \cos(2\pi f_0[t-t_0])e^{-(t-t_0)^2/2\sigma^2}$ is a Gaussian pulse with modulation frequency f_0, duration σ, and delay t_0. In all examples, $t_0 = 8\sigma$ and $\sigma = 3/(2\pi f_{\text{bw}})$, where f_{bw} denotes an effective band. This specific selection of σ ensures that 99.998% of the incident energy is within the frequency band $[f_0 - f_{\text{bw}}, f_0 + f_{\text{bw}}]$. The free-space wavelengths at the minimum and maximum frequency of the excitation are $\lambda_{\max} = c_0/[f_0 - f_{\text{bw}}]$ and $\lambda_{\min} = c_0/[f_0 + f_{\text{bw}}]$.

In all examples, the unknown coefficients of the equivalent electric and magnetic current densities, $J_n(k\Delta t)$ and $M_n(k\Delta t)$, $k = 1, ..., N_{\text{t}}$, $n = 1, ..., N_{\text{s}}$, are computed by the proposed TD-PMCHWT-SIE solver under this excitation. After the time domain simulation is completed, the Fourier transforms of $J_n(k\Delta t)$ and $M_n(k\Delta t)$ are computed using the discrete time Fourier transform (DTFT). Normalizing the results with the DTFT of the samples of the Gaussian pulse, $G(k\Delta t)$, yields coefficients of the frequency domain (i.e., time harmonic) electric and magnetic current densities denoted by $J_n(l\Delta\omega)$ and $M_n(l\Delta\omega)$, $l = 1, ..., N_f$, where $\Delta\omega = 2\pi\Delta f$, Δf is the frequency step, and N_f is the number of frequency samples. This is followed by the computation of the frequency domain scattering and extinction cross sections, $C_{\text{sca}}(l\Delta\omega)$ and $C_{\text{ext}}(l\Delta\omega)$ [67]:

$$C_{\text{sca}}(l\Delta\omega) = \frac{1}{16\pi^2|E_0^{\text{inc}}|^2}\int_\Omega |\mathbf{F}(\hat{\mathbf{r}}, l\Delta\omega)|^2 d\Omega \tag{3.60}$$

$$C_{\text{ext}}(l\Delta\omega) = \frac{1}{k_0|E_0^{\text{inc}}|^2}\text{Im}\{E_0^{\text{inc}}\hat{\mathbf{p}}\cdot\mathbf{F}(\hat{\mathbf{k}}, l\Delta\omega)\}. \tag{3.61}$$

Here, $\hat{\mathbf{r}} = \hat{\mathbf{x}}\sin\theta\cos\phi + \hat{\mathbf{y}}\sin\theta\sin\phi + \hat{\mathbf{z}}\cos\theta$ is the unit vector along the direction defined by angles θ and ϕ, $d\Omega = \sin\theta d\theta d\phi$ is the differential solid angle, and $\mathbf{F}(\hat{\mathbf{r}}, l\Delta\omega)$ represents the scattered electric field pattern in the far field and computed by inserting

$J_n(l\Delta\omega)$ and $M_n(l\Delta\omega)$ into

$$\mathbf{F}(\hat{\mathbf{r}}, l\Delta\omega) = -\mathrm{j}(l\Delta\omega)\mu_0 \mathbf{N}(\hat{\mathbf{r}}, l\Delta\omega) + \mathrm{j}k_0 \hat{\mathbf{r}} \times \mathbf{L}(\hat{\mathbf{r}}, l\Delta\omega) \tag{3.62}$$

where

$$\mathbf{N}(\hat{\mathbf{r}}, l\Delta\omega) = \sum_{n=1}^{N_\mathrm{s}} J_n(l\Delta\omega) \int_{S_n} \mathbf{f}_n(\mathbf{r}') e^{\mathrm{j}k_0 \mathbf{r}'\cdot\hat{\mathbf{r}}} ds' \tag{3.63}$$

$$\mathbf{L}(\hat{\mathbf{r}}, l\Delta\omega) = \sum_{n=1}^{N_\mathrm{s}} M_n(l\Delta\omega) \int_{S_n} \mathbf{f}_n(\mathbf{r}') e^{\mathrm{j}k_0 \mathbf{r}'\cdot\hat{\mathbf{r}}} ds'. \tag{3.64}$$

Note that here $k_0 = (l\Delta\omega)\sqrt{\varepsilon_0\mu_0}$, it is assumed that $r \to \infty$ during the derivation of Eqs. (3.62)-(3.64), and $\hat{\mathbf{r}} \cdot \mathbf{F}(\hat{\mathbf{r}}, l\Delta\omega) = 0$ is explicitly enforced during the computation of $C_\mathrm{sca}(l\Delta\omega)$. Extinction efficiency of a scatterer, $Q_\mathrm{ext}(l\Delta\omega)$, is defined as the ratio of $C_\mathrm{ext}(l\Delta\omega)$ to its geometrical cross section on the plane perpendicular to the direction of propagation of the incident field $\hat{\mathbf{k}}$. In all examples presented in this section, $Q_\mathrm{ext}(l\Delta\omega)$, $C_\mathrm{ext}(l\Delta\omega)$, and $C_\mathrm{sca}(l\Delta\omega)$ computed by the proposed TD-PMCHWT-SIE solver are compared to those obtained by the frequency domain (FD) PMCHWT-SIE solver of [17] which computes $J_n(l\Delta\omega)$ and $M_n(l\Delta\omega)$ on the same discretization but directly in the frequency domain. Note that FD-PMCHWT-SIE solver has to be executed N_f times for this operation.

3.3.1 Accuracy of FRVF Scheme

In this section, the accuracy of the expansions in Eqs. (3.12) and (3.13) is demonstrated. The samples of the scatterer's permittivity, $\varepsilon_1(\omega_i)$, $i = 1, ..., N_\omega^\mathrm{VF}$, which are used in the FRVF scheme to generate the terms in these expansions, are obtained from the experimental data of Johnson-Christy tabulated for gold and silver in [60]. It should be noted here that experiments were carried out at only 49 frequency points, therefore spline interpolation is used to generate samples at $\omega_i \in 2\pi[f_\mathrm{min}^\mathrm{VF}, f_\mathrm{max}^\mathrm{VF}]$, $i = 1, ..., N_\omega^\mathrm{VF}$, $N_\omega^\mathrm{VF} = 1000$ required by Eqs. (3.12) and (3.13).

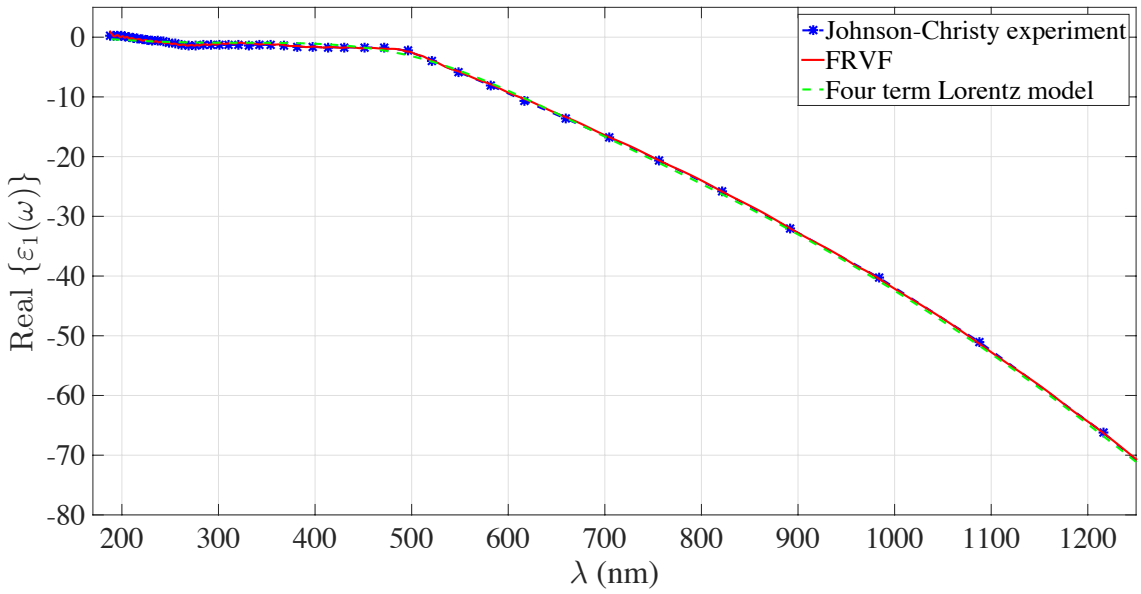

(a)

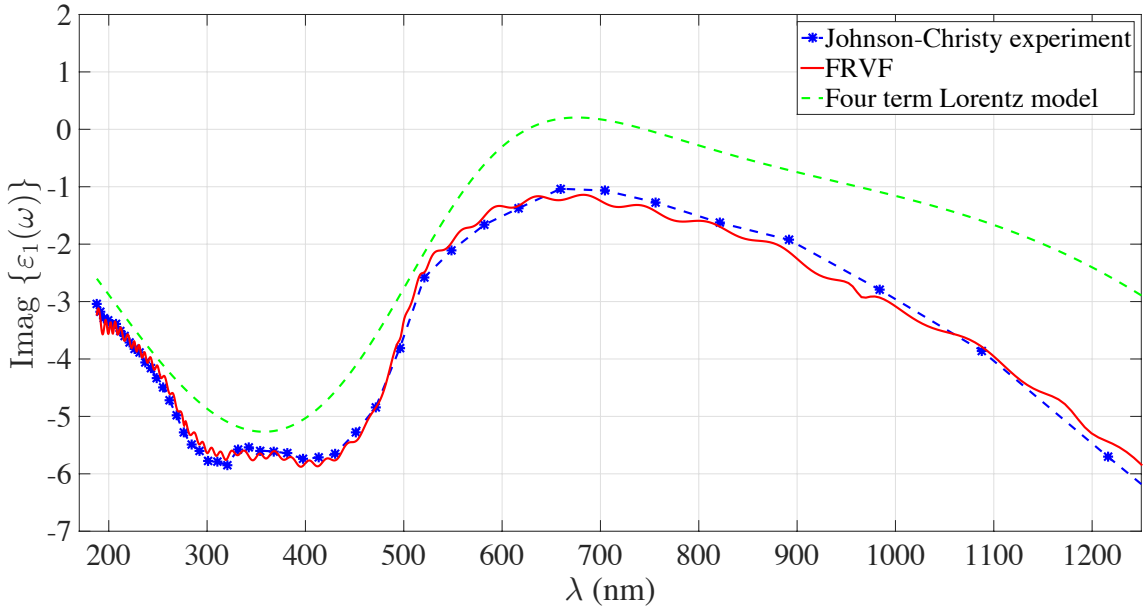

(b)

Figure 3.1: (a) Real and (b) imaginary parts of $\varepsilon_1(\omega)$ for gold.

Here, $f_{\min}^{\mathrm{VF}} = 155$ THz, and $f_{\max}^{\mathrm{VF}} = 1595$ THz (corresponding to free-space wavelengths of $\lambda_{\max}^{\mathrm{VF}} = c_0/f_{\min}^{\mathrm{VF}} = 1937$ nm and $\lambda_{\min}^{\mathrm{VF}} = c_0/f_{\max}^{\mathrm{VF}} = 188$ nm), and the number of terms in the expansions $N_{\mathrm{p}}^{\mathrm{VF}} = 100$. Fig. 3.1 and 3.2 compare $\varepsilon_1(\omega)$ in (3.12) obtained using the FRVF to that provided by the four-term Lorentz model described in [49], for gold and silver, respectively. Figures clearly show that both the FRVF ex-

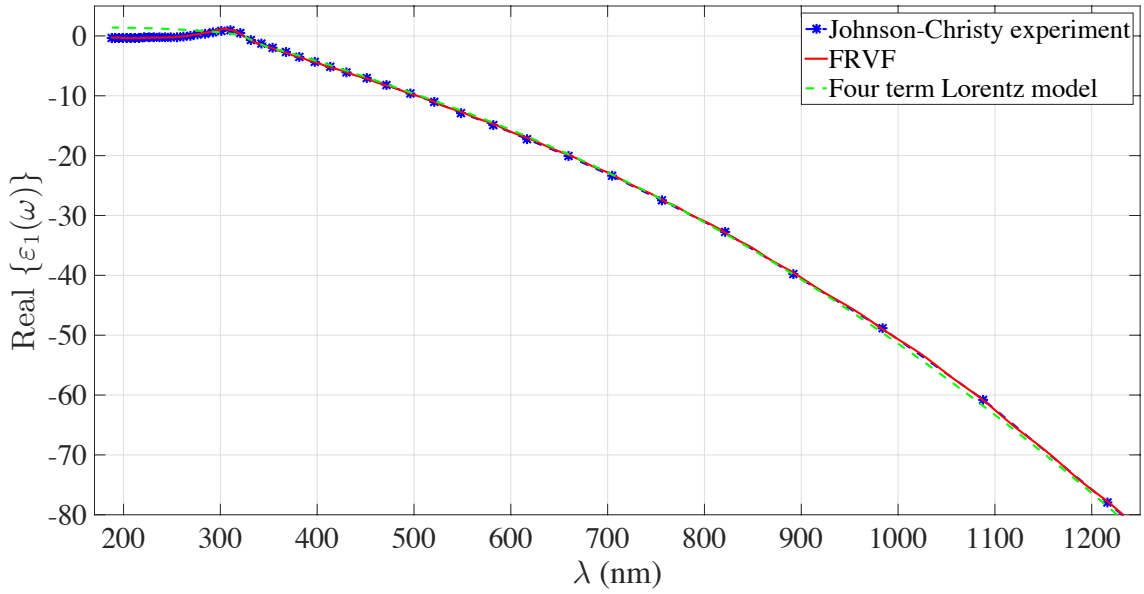

(a)

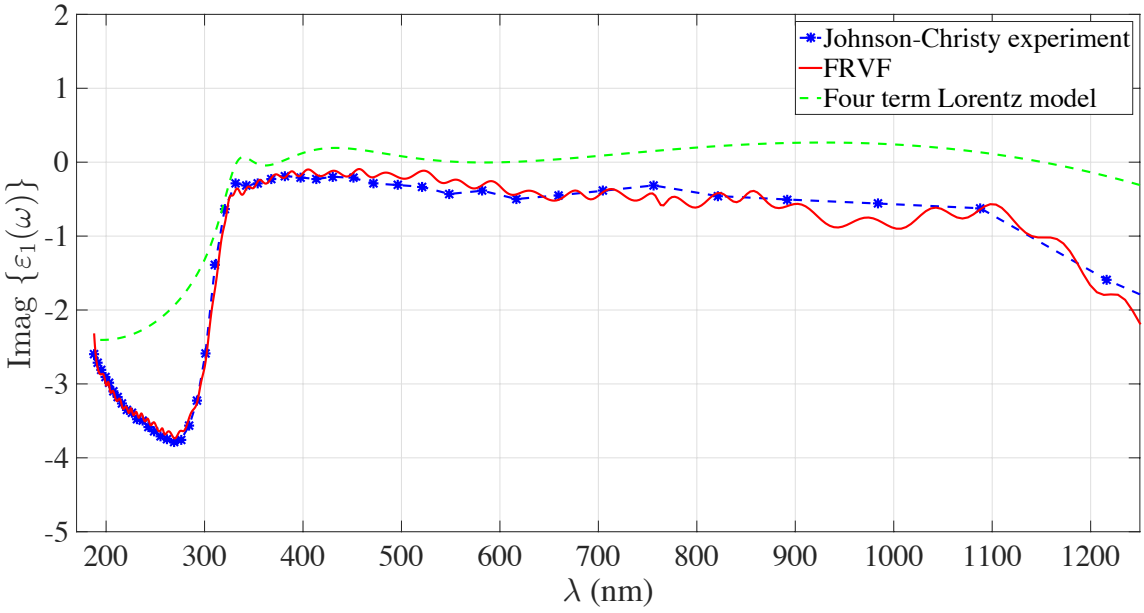

(b)

Figure 3.2: (a) Real and (b) imaginary parts of $\varepsilon_1(\omega)$ for silver.

pansion and the Lorentz model generate the real part of $\varepsilon_1(\omega)$ accurately. However, the imaginary part generated by the four term Lorentz model does not match the experimental data while FRVF captures the experimental data even at the resonance points of gold (320 nm) and silver (269 nm and 333 nm).

For the sake of completeness, Fig. 3.3, plot amplitude of $\gamma_1(t)$ and $\bar{\gamma}_1(t)$, which

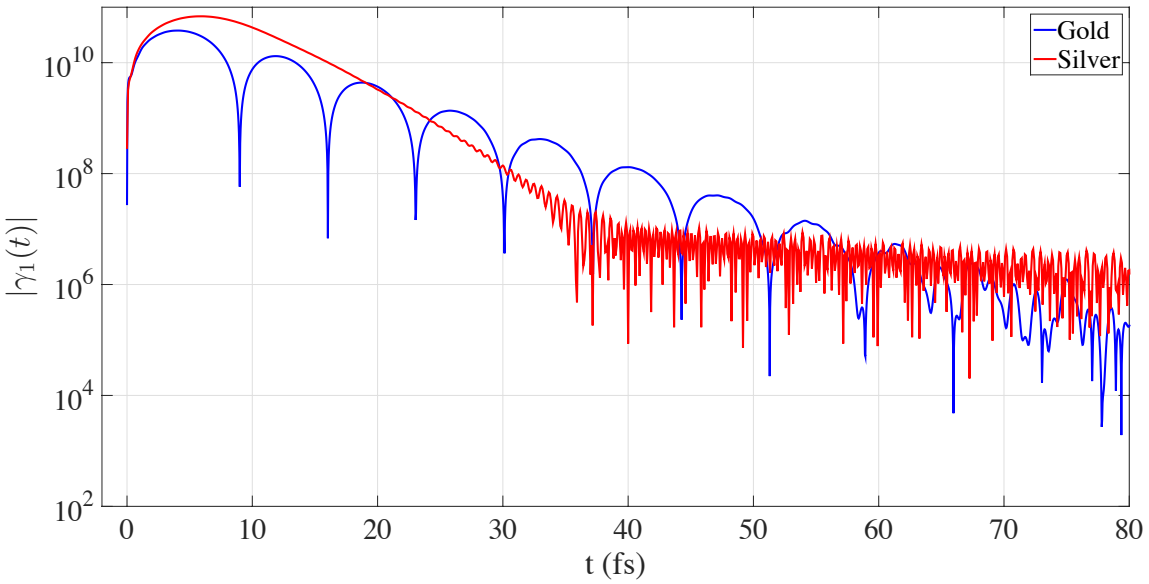

(a)

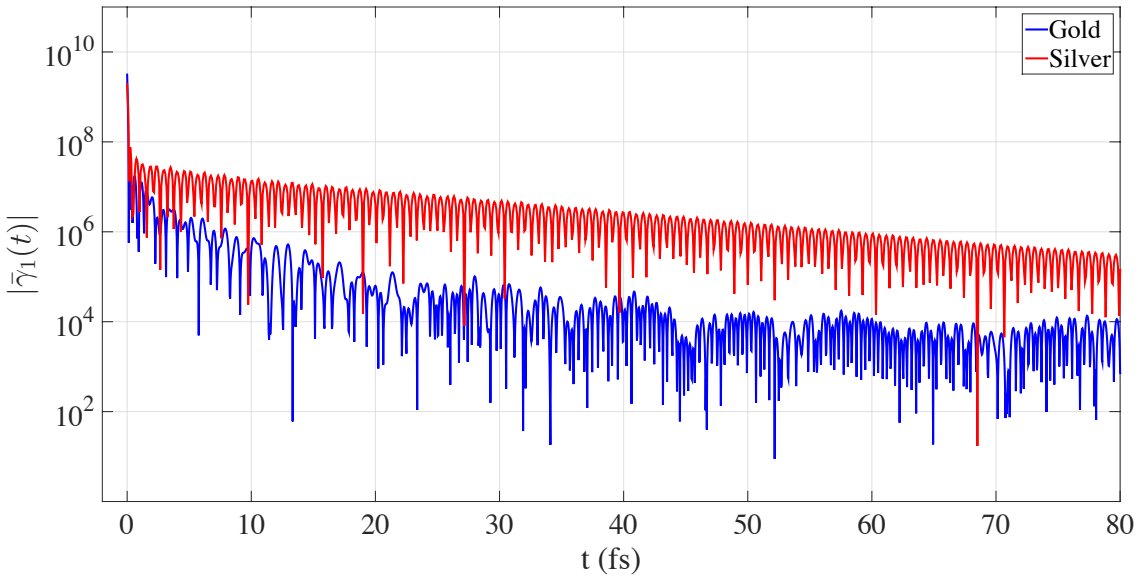

(b)

Figure 3.3: Amplitude of (a) $\gamma_1(t)$ and (b) $\bar{\gamma}_1(t)$ for gold and silver.

correspond to the Fourier transform of the summation in Eqs. (3.12) and (3.13), i.e., $\varepsilon_1(t)$ and $\bar{\varepsilon}_1(t)$ without the Dirac delta term [see Eqs. (3.14) and (3.15)].

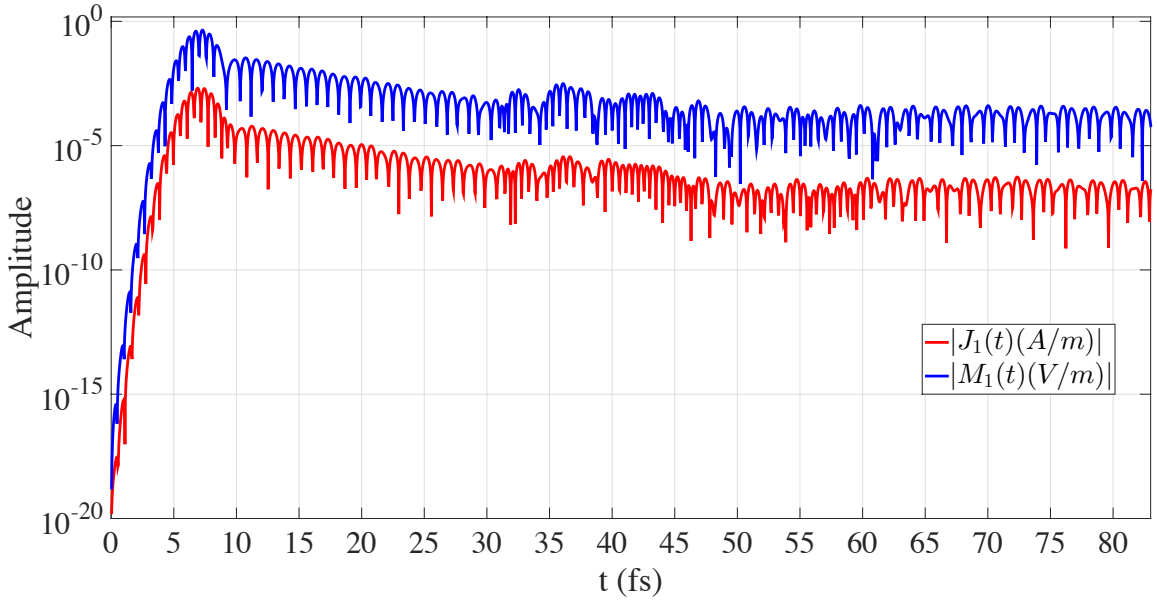

(a)

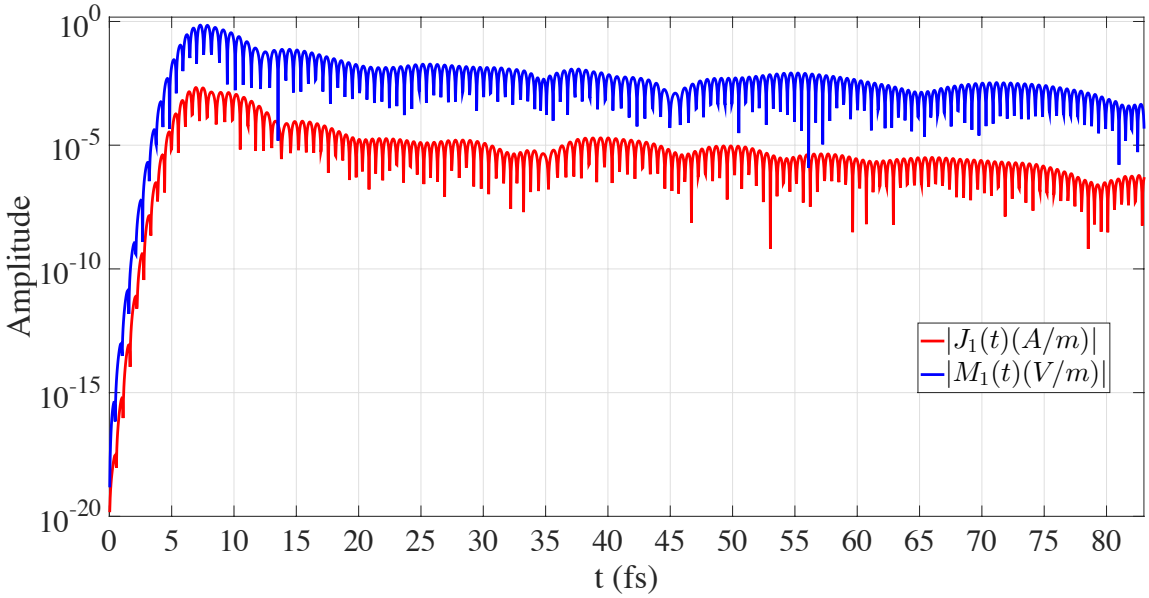

(b)

Figure 3.4: Amplitude of $J_1(t)$ and $M_1(t)$ induced on (a) the gold sphere and (b) the silver sphere.

3.3.2 Gold and Silver Spheres

In this example, the scatterer is a silver or gold sphere of radius 50 nm. The permittivities of gold and silver are obtained using the Johnson-Christy [60] experimental data. For the FRVF scheme, $N_{\mathrm{p}}^{\mathrm{VF}} = 100$, $N_{\omega}^{\mathrm{VF}} = 1000$, $\lambda_{\mathrm{min}}^{\mathrm{VF}} = 188$ nm, and $\lambda_{\mathrm{max}}^{\mathrm{VF}} = 1937$

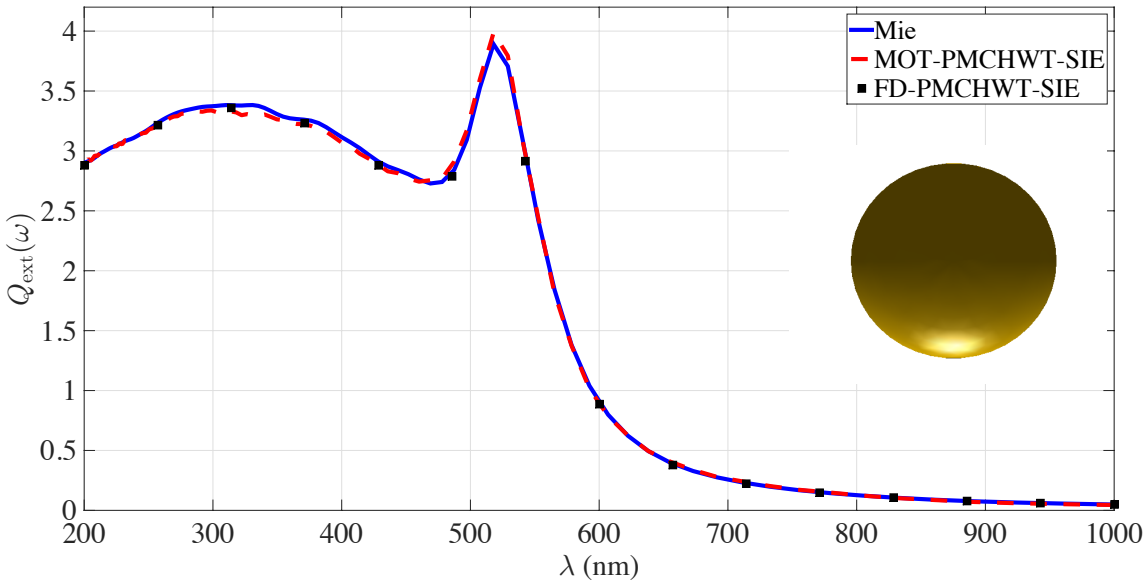

(a)

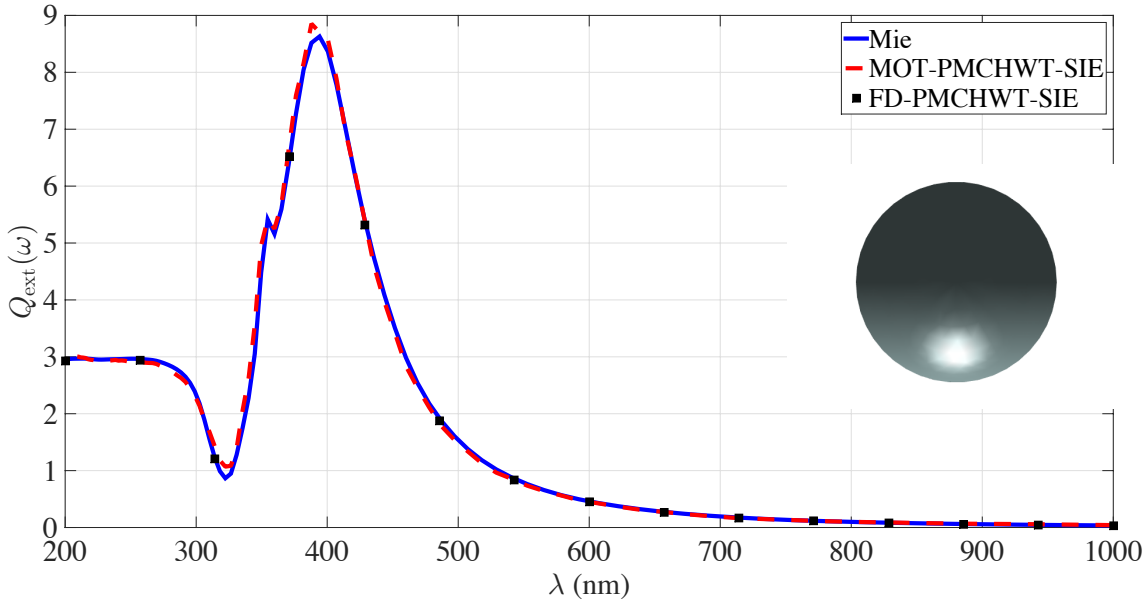

(b)

Figure 3.5: $Q_{\text{ext}}(\omega)$ computed for (a) the gold sphere and (b) the silver sphere.

nm. The excitation parameters are $\hat{\mathbf{p}} = \hat{\mathbf{x}}$, $\hat{\mathbf{k}} = \hat{\mathbf{z}}$, $f_0 = 900$ THz, $f_{\text{bw}} = 600$ THz, $\lambda_{\text{min}} = 200$ nm, and $\lambda_{\text{max}} = 1000$ nm. The currents induced on the sphere surface are discretized using $N_{\text{s}} = 1926$ RWG basis functions and the simulation is executed for $N_{\text{t}} = 2500$ time steps with step size $\Delta t = 0.0333$ fs. Fig. 3.4 plot the amplitudes of $J_1(k\Delta t)$ and $M_1(k\Delta t)$, $k = 1, ..., N_{\text{t}}$ computed during the simulations of the gold and

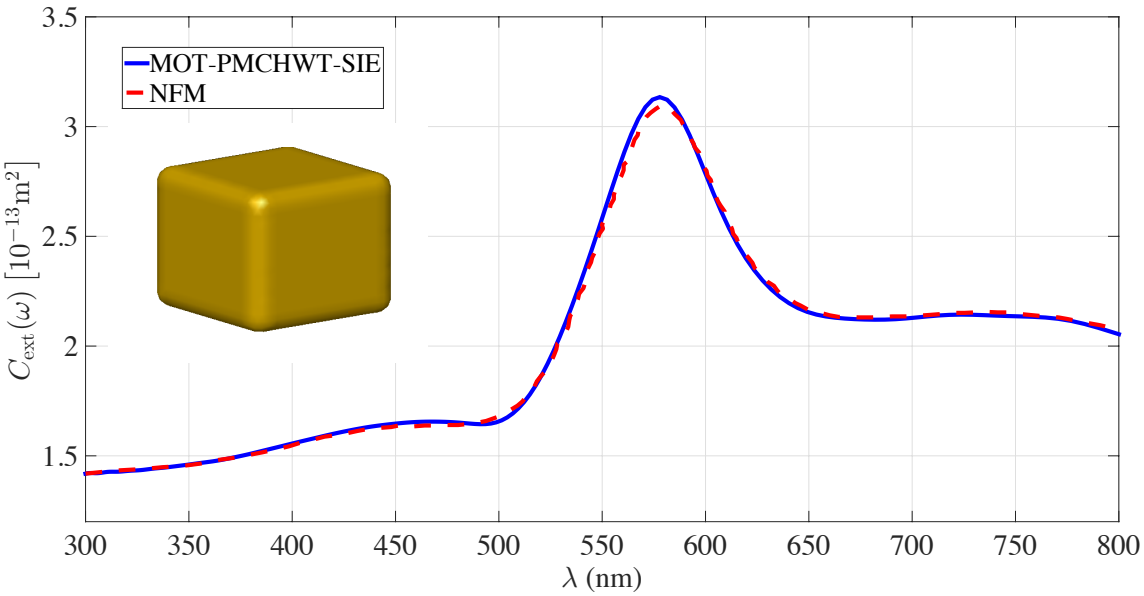

Figure 3.6: $C_{\text{ext}}(\omega)$ computed for the gold rounded cube.

silver spheres, respectively. Figures clearly show the stability of the results. Fig. 3.5 compare $Q_{\text{ext}}(l\Delta\omega)$, $l = 1, ..., N_f$, $N_f = 100$, $\Delta f = 12$ THz, computed by the TD-PMCHWT-SIE and FD-PMCHWT-SIE solvers, and those obtained from Mie series solution. Results agree well with each other.

Please note that the resonance observed in $C_{\text{ext}}(\omega)$ (Fig. 3.5(b)) at $\lambda = 354.6$ nm is due to the electrostatic resonance of a negative-permittivity dielectric sphere [68]. At $\lambda = 354.6$, the permittivity of silver is $-2.027 - \text{j}0.2819$. If the imaginary part of the permittivity was zero, the resonance effect would be more pronounced.

3.3.3 Gold Rounded Cube

Next, scattering from a gold rounded cube [69] is analyzed using the proposed TD-PMCHWT-SIE solver. The dimension of the cube is 200 nm and the radius of fillets on the edges and corners is 20 nm. The permittivity of gold is obtained using the Johnson-Christy [60] experimental data. For the FRVF scheme, $N_{\text{p}}^{\text{VF}} = 20$, $N_{\omega}^{\text{VF}} = 1000$, $\lambda_{\text{min}}^{\text{VF}} = 292$ nm, and $\lambda_{\text{max}}^{\text{VF}} = 1088$ nm. The excitation parameters are $\hat{\mathbf{p}} = \hat{\mathbf{x}}$, $\hat{\mathbf{k}} = \hat{\mathbf{z}}$, $f_0 = 685$ THz, $f_{\text{bw}} = 315$ THz, $\lambda_{\text{min}} = 300$ nm, and $\lambda_{\text{max}} = 810$ nm. The

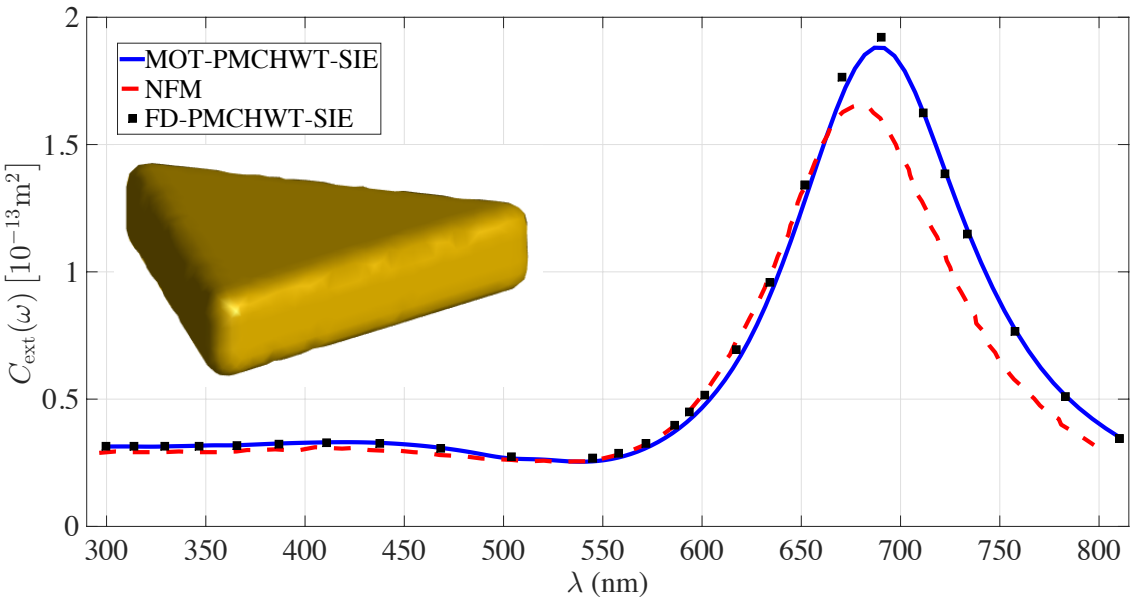

Figure 3.7: $C_{\text{ext}}(\omega)$ computed for the gold rounded triangular prism.

currents induced on the cube surface are discretized using $N_{\text{s}} = 6543$ RWG basis functions and the simulation is executed for $N_{\text{t}} = 900$ time steps with step size $\Delta t = 0.05$ fs. Figure 6 compares $Q_{\text{ext}}(l\Delta\omega)$, $l = 1, ..., N_f$, $N_f = 200$, $\Delta f = 3.15$ THz, obtained using the proposed TD-PMCHWT-SIE solver to that computed by the null field method (NFM) [69]. Results are in good agreement with each other.

3.3.4 Gold Rounded Triangular Prism

In this example, the scatterer is a gold rounded triangular prism of height 40 nm and edge length 200 nm [69]. The radius of the fillets on the edges and the corners is 10 nm. The permittivity of gold is obtained using the Johnson-Christy [60] experimental data. For the FRVF scheme, $N_{\text{p}}^{\text{VF}} = 20$, $N_{\omega}^{\text{VF}} = 1000$, $\lambda_{\text{min}}^{\text{VF}} = 292$ nm, and $\lambda_{\text{max}}^{\text{VF}} = 1088$ nm. The excitation parameters are $\hat{\mathbf{p}} = \hat{\mathbf{x}}$, $\hat{\mathbf{k}} = \hat{\mathbf{z}}$, $f_0 = 685$ THz, $f_{\text{bw}} = 315$ THz, $\lambda_{\text{min}} = 300$ nm, and $\lambda_{\text{max}} = 810$ nm. The currents induced on the cube surface are discretized using $N_{\text{s}} = 6543$ RWG basis functions and the simulation is executed for $N_{\text{t}} = 900$ time steps with step size $\Delta t = 0.05$ fs. Figure 7 compares $C_{\text{ext}}(l\Delta\omega)$, $l = 1, ..., N_f$, $N_f = 200$, $\Delta f = 3.15$ THz obtained using the TD-PMCHWT-SIE and

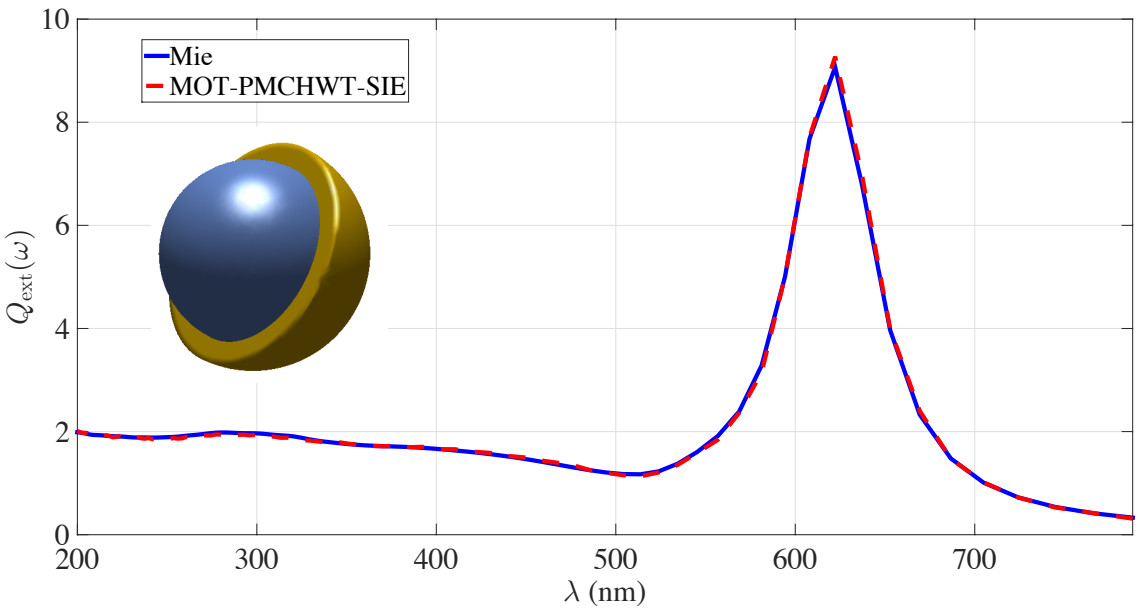

Figure 3.8: $Q_{\text{ext}}(\omega)$ computed for the gold shell with silica core.

FD-PMCHWT-SIE solvers to that computed by the discrete dipole approximation (DDA) [69]. Results obtained by the TD-PMCHWT-SIE and FD-PMCHWT-SIE solvers match well with each other, but the result computed by the DDA differs from those especially around the peak values. Same type of mismatch is also observed in [69] and explained by the fact that the DDA loses accuracy as the permittivity of the scatterer increases [70].

3.3.5 Gold-Coated Silica Sphere

Scattering from a silica sphere coated with gold [49] is analyzed using the proposed TD-PMCHWT-SIE solver. The radius of the silica sphere and the thickness of the gold layer are 40 nm and 10 nm, respectively. The relative permittivity of the silica is 2.04 while the permittivity of gold is obtained using the Johnson-Christy [60] experimental data. For the FRVF scheme, $N_{\text{p}}^{\text{VF}} = 100$, $N_{\omega}^{\text{VF}} = 1000$, $\lambda_{\text{min}}^{\text{VF}} = 188$ nm, and $\lambda_{\text{max}}^{\text{VF}} = 1937$ nm. The excitation parameters are $\hat{\mathbf{p}} = \hat{\mathbf{x}}$, $\hat{\mathbf{k}} = \hat{\mathbf{z}}$, $f_0 = 940$ THz, $f_{\text{bw}} = 560$ THz, $\lambda_{\text{min}} = 200$ nm, and $\lambda_{\text{max}} = 788$ nm. The currents induced on the

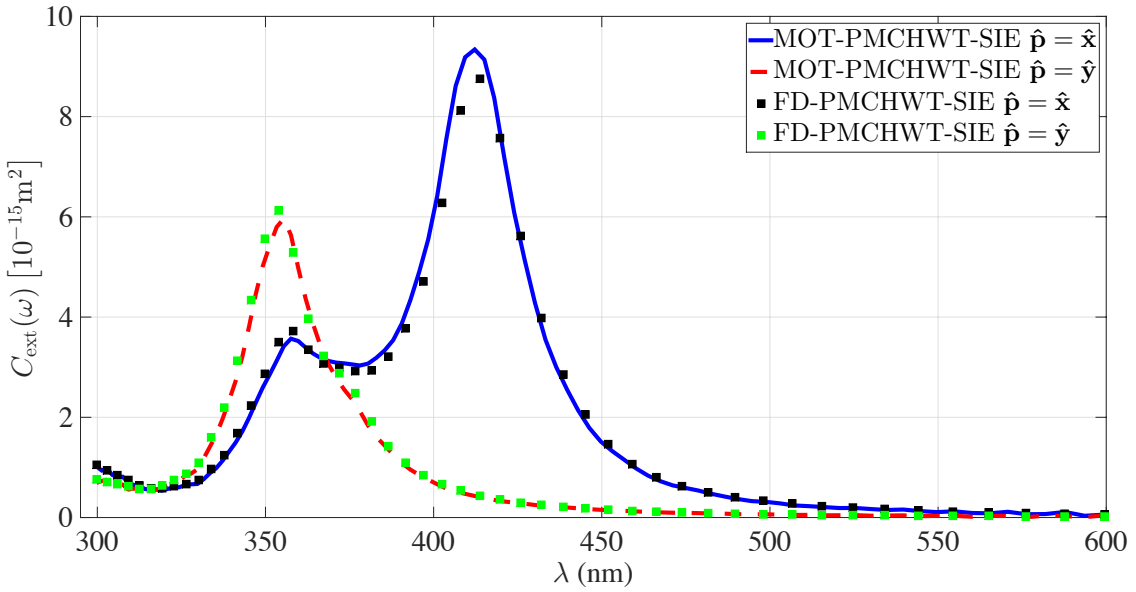

Figure 3.9: $C_{\text{ext}}(\omega)$ computed for the silver dimer under two excitations with different polarizations.

sphere surface are discretized using $N_{\text{s}} = 2130$ RWG basis functions and the simulation is executed for $N_{\text{t}} = 2000$ time steps with step size $\Delta t = 0.0333$ fs. Figure 8 plots $C_{\text{ext}}(l\Delta\omega)$, $l = 1, ..., N_f$, $N_f = 100$, $\Delta f = 11.2$ THz computed by the TD-PMCHWT-SIE solver to that obtained from the Mie series solution. Results are in good agreement.

3.3.6 Silver Dimer

In this example, the scatterer is an x-directed dimer consisting of two silver spheres residing on the xy-plane [71]. The radius of the spheres and the shortest distance between them are 15 nm and 1.5 nm, respectively. The permittivity of silver is obtained using the Palik experimental data [61]. For the FRVF scheme, $N_{\text{p}}^{\text{VF}} = 100$, $N_{\omega}^{\text{VF}} = 1000$, $\lambda_{\text{min}}^{\text{VF}} = 196$ nm, and $\lambda_{\text{max}}^{\text{VF}} = 1033$ nm. Two simulations are carried out for two polarizations of the incident field, $\hat{\mathbf{p}} = \hat{\mathbf{x}}$ and $\hat{\mathbf{p}} = \hat{\mathbf{y}}$. The remaining excitation parameters are $\hat{\mathbf{k}} = \hat{\mathbf{z}}$, $f_0 = 750$ THz, $f_{\text{bw}} = 250$ THz, $\lambda_{\text{min}} = 300$ nm, and $\lambda_{\text{max}} = 600$ nm. The currents induced on the sphere surfaces are discretized

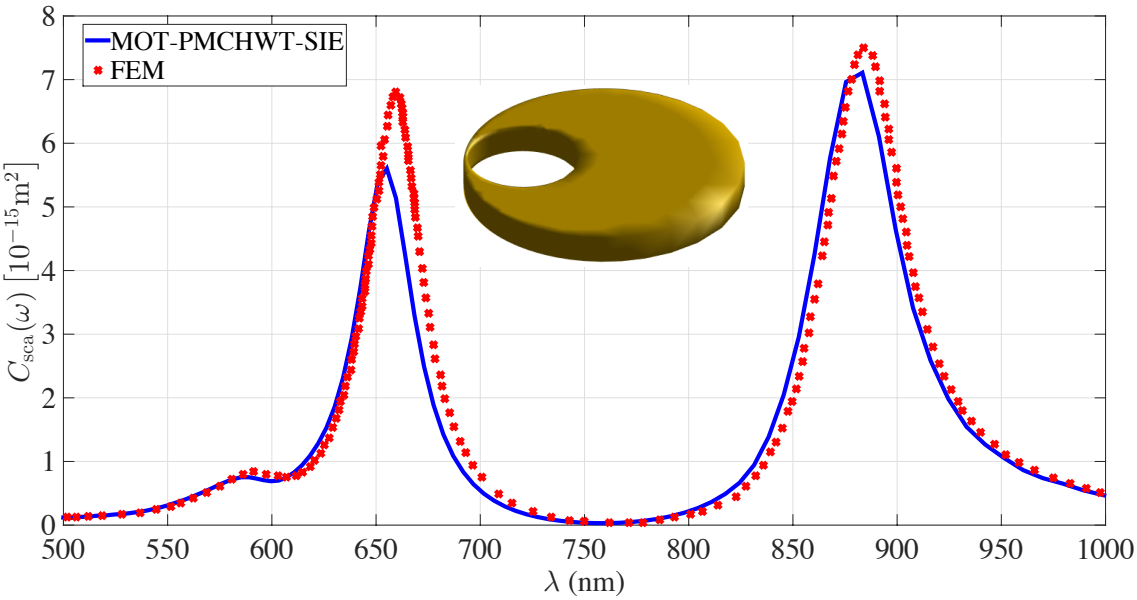

Figure 3.10: $C_{\text{sca}}(\omega)$ computed for the gold disk with the non-concentric cavity.

using $N_{\text{s}} = 1428$ RWG basis functions. Both simulations are executed for $N_{\text{t}} = 2000$ time steps with step size $\Delta t = 0.0333$ fs. Figure 9 compares $C_{\text{ext}}(l\Delta\omega)$, $l = 1, ..., N_f$, $N_f = 100$, $\Delta f = 5$ THz, computed by the TD-PMCHWT-SIE and FD-PMCHWT-SIE solvers. Results agree well with each other and also with those provided in [71].

3.3.7 Gold Disk with a Non-Concentric Cavity

In the last example, the scatterer is a gold disk embedding a non-concentric cavity and residing on the xy-plane [72]. The radius and thickness of the disk are 50 nm and 10 nm, respectively. The radius of the circular cavity is 20 nm and its center is offset from the center of the disk by 29 nm in the x-direction. The permittivity of gold is obtained using the Johnson-Christy [60] experimental data. For the FRVF scheme, $N_{\text{p}}^{\text{VF}} = 20$, $N_{\omega}^{\text{VF}} = 1000$, $\lambda_{\text{min}}^{\text{VF}} = 496$ nm, and $\lambda_{\text{max}}^{\text{VF}} = 1216$ nm. The excitation parameters are $\hat{\mathbf{p}} = \hat{\mathbf{y}}$, $\theta^{\text{inc}} = 78$ and $\phi^{\text{inc}} = 0$, $f_0 = 450$ THz, $f_{\text{bw}} = 150$ THz, $\lambda_{\text{min}} = 500$ nm, and $\lambda_{\text{max}} = 1000$ nm. The currents induced on the surface of the scatterer are discretized using $N_{\text{s}} = 4380$ RWG basis functions. The simulation is executed for $N_{\text{t}} = 1500$ time steps with step size $\Delta t = 0.083$ fs. Figure 10 compares

$C_{\text{sca}}(l\Delta\omega)$, $l = 1, ..., N_f$, $N_f = 100$, $\Delta f = 3$ THz, obtained using the proposed TD-PMCHWT-SIE solver to that computed by the frequency domain FEM [72]. The results agree with each other reasonably well. The positions of the two main peaks in the results are close enough yet the peak at 660 nm is less pronounced and slightly blue-shifted in the result obtained by the TD-PMCHWT-SIE solver.

3.4 Conclusion

In this chapter, an MOT scheme for solving the TD-PMCHWT-SIE enforced on surfaces of plasmonic nanostructures is described. The unknown equivalent electric and magnetic current densities introduced on these surfaces are expanded by RWG and polynomial basis functions in space and time, respectively. Inserting this expansion into the TD-PMCHWT-SIE and Galerkin-testing the resulting equation at discrete times yield a system of equations. This system is then solved for the unknown expansion coefficients using the MOT scheme.

The TD-PMCHWT-SIE requires evaluation of additional convolutions involving the plasmonic medium's permittivity and Green function and the temporal basis function to compute the scattered fields. This convolution is discretized in a way that is fully consistent with the MOT scheme. The computation of the discretized convolution is carried out with almost no additional cost and without changing the computational complexity of the MOT scheme. Time domain samples of the permittivity and the Green function required by this computation are obtained from their frequency domain samples using the FRVF algorithm. Frequency samples are generated using tabulated data obtained from experiments.

Numerical results which demonstrate the accuracy of the TD-PMCHWT-SIE solver are presented. The quantum-corrected version of the same solver, which can accurately be applied to scatterers separated by subnanometer distances, is described in the next chapter.

Chapter 4

TD-SIE Solver for Quantum Corrected Analysis of Scattering from Plasmonic Nanostructures with Sub-nanometer Gaps

4.1 Introduction

Recent advances in nano-fabrication techniques permit prototyping and production of plasmonic structures with sub-nanometer holes and gaps [73, 74]. When two nanostructures are separated with a gap shorter than approximately 0.5 nm, one can expect to see the effects of quantum (electron) tunneling on the structures' scattering spectrum [5, 6, 75, 76]. Indeed this has been demonstrated experimentally for a single dimer [77–81] and an ensemble of dimers [82, 83]. Consequently this means that, to design geometrically more complicated nano-scale plasmonic devices, simulations tools, which are capable of accurately modeling these quantum-tunneling effects, are needed. Unfortunately, numerical schemes, which are developed for solving classical equations of electromagnetics, are intrinsically not equipped to model tunneling of electrons between two nanostructures. One could use a quantum mechanical solver for this purpose, but this approach would be computationally very expensive since the whole device has to be modeled at an atomic level. One way to overcome this bottleneck and take into account the tunneling effects accurately without sacrificing from efficiency is to incorporate quantum mechanical solution locally (around and inside the gap) into a classical electromagnetic solver. This approach is termed quantum-corrected model (QCM) [6, 76].

The QCM proposed in [6, 76] replaces the gap between two nanostructures with

an auxiliary (cylindrically multi-layered) tunnel. In [6, 37, 76, 84], Drude models with different parameters are used to represent the permittivity of the nanostructures and the auxiliary tunnel. To determine the parameters of the tunnel's Drude model, first, quantum tunneling probability is computed by solving a one-dimensional (1D) Schrödinger equation for a single electron for different gap lengths (corresponding to layers of the tunnel). Then, this tunneling probability is used to compute the conductivity of the layers. Finally, the conductivity is incorporated into the Drude model through a damping parameter [6, 76] or by adding it directly to the imaginary part of the permittivity [37, 84]. Once the permittivity of the auxiliary tunnel is computed, a frequency domain surface integral equation (FD-SIE) solver [6, 37, 76] or a frequency domain finite element method (FD-FEM) [84] is used to characterize the time harmonic electromagnetic interactions on the combined structure (two nanostructures plus the auxiliary tunnel connecting them).

The QCM briefly summarized above has two bottlenecks: (i) While solving the 1D Schrödinger equation for a single electron, atomic structure of the materials is not accounted for. This might result in inaccuracies: It has been argued in [85] that modeling many body interaction of electrons and taking the atomic structure of a material into account yield more accurate values for its optical parameters. (ii) The Drude model used for the permittivity of the nanostructures does not take into account the inter-band contributions to the permittivity. Including only intra-band contributions produces permittivity values that do not match to those obtained by experiments [49]. Indeed, experimental permittivity values are used in numerical characterization of gold and silver nanoparticles in many different studies [77, 78, 81]. (iii) A classical electromagnetic solver, which relies on a volumetric discretization, as in [84], requires a very high sampling rate in the vicinity of the nanostructure surface to accurately capture the fast decaying plasmonic fields. This significantly increases the number of unknowns to be solved for.

In this work, a quantum corrected time domain surface integral equation (TD-SIE) solver for characterizing transient electromagnetic wave interactions on plasmonic nanostructures with sub-nanometer gaps is formulated and implemented. The permittivity of the nanostructure (bulk material) and the auxiliary tunnel are obtained from the density functional theory (DFT) computations [86, 87]. DFT solves the many body problem of electrons in a crystal structure of atoms and accounts for inter- and intra-band contributions to the permittivity [9, 88] [addressing the bottleneck (i) above]. Then the permittivity is represented as a sum of rational functions (in Laplace domain). Weights of the rational functions are extracted by the fast relaxed vector fitting (FRVF) scheme [57–59] from the frequency domain permittivity samples (computed by the DFT). Finally, time domain permittivity is obtained analytically by applying inverse Laplace transform to the sum of rational functions. Note that the computation of the time domain permittivity using the procedure described here does not assume any specific model but requires only frequency domain samples of the permittivity [addressing the bottleneck (ii) above]. Electromagnetic interactions on the combined structure (two nanostructures plus the auxiliary tunnel connecting them) are accounted for by the time domain Poggio-Miller-Chan-Harrington-Wu-Tsai surface integral equation (TD-PMCHWT-SIE) [7]. TD-PMCHWT-SIE is enforced on interfaces between different dielectric volumes, each of which is representing nanostructures, layers of the tunnel, and the background medium. Equivalent electric and magnetic currents introduced on these interfaces and they are expanded in terms of Rao-Wilton-Glisson (RWG) basis functions [40] in space and polynomial interpolants in time [23]. Inserting this expansion into the TD-PMCHWT-SIE and Galerkin testing the resulting equation at discrete times yield a system of equations. This system is solved for the unknown expansion coefficients of the currents using a marching on-in-time (MOT) scheme. Note that this scheme calls for computation of the time domain samples of the Green functions of the unbounded media with permittivity of

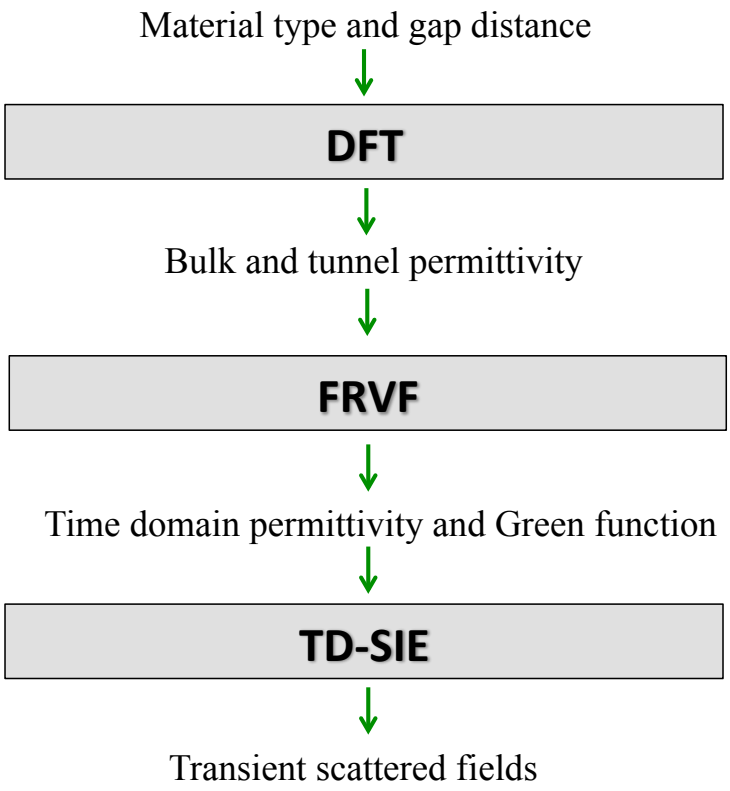

Figure 4.1: Steps of the quantum corrected transient electromagnetic analysis

each volume. Time domain samples of the Green functions are obtained from their frequency domain samples using the same procedure used for time domain permittivity. It should be emphasized here that the TD-PMCHWT-SIE solver calls for only the discretization of boundaries of the structure (instead of a volumetric discretization), satisfies radiation condition implicitly without any need for approximate boundary conditions, and time step size does not depend on spatial discretization, i.e. time step size is not limited to Courant-Frederich-Lewy (CFL) like condition [10,11] [addressing the challenge (iii)].

4.2 Formulations

This section describes the steps involved in quantum corrected analysis of transient electromagnetic/plasmonic field interactions. Figure 4.1 presents a flow diagram sum-

marizing these steps.

4.2.1 Tunnel Model

It has been theoretically and experimentally shown that the quantum tunneling is observed only when the distance between two structures is smaller than approximately 0.5 nm [6, 76–81] . Additionally, the permittivity of the auxiliary tunnel introduced between the two nanostructures depends on this distance [6]. It should be noted here that, since this distance might vary depending on the shape of the nanostructure surfaces, the auxiliary tunnel is constructed layer by layer. In other words the distance between the two surfaces is sampled and each layer corresponds to a "sampled" gap tunneling distance. The permittivity of a layer is then obtained from the DFT computations that use the sampled distance associated with that layer (see Section 4.2.2). As expected higher number of layers translates to higher accuracy in the tunnel model since the spatial dependence of the permittivity is sampled with a higher accuracy. This is especially true for shorter tunneling distances since the variation in the permittivity of the resulting auxiliary tunnel is much faster.

For an example of how the tunnel model is constructed, consider a dimer consisting of two spheres, as shown in Fig. 4.2a. In this case, the tunneling gap distance, which is defined as the distance between two spherical surfaces along the direction that is perpendicular to the dimer axis, is clearly not constant and varies between d_{min} (shortest distance) and $d_{max} = 0.55$ nm (distance beyond which the tunneling effects are assumed to vanish). It should be noted here the schematics in Figs. 4.2a and 4.2b are not drawn to scale. Figure 4.2b shows three (cylindrical) layers used for representing the auxiliary tunnel in Fig. 4.2a. End surfaces (caps) of the layers are not flat but curved surfaces that match the surfaces of the spheres. This means that each of these layers must be assigned an effective length as described next. For the inner most layer [shown with red in Fig. 4.2b] the effective layer length is the shortest

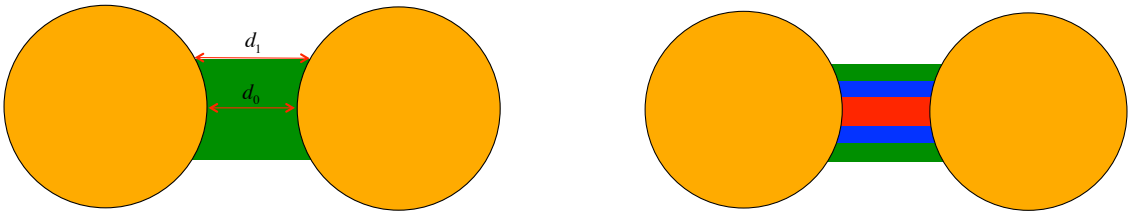

Figure 4.2: Auxiliary tunnel with (a) single layer and (b) three layers.

distance between the two "caps" of the layer. For the other two layers, effective length is the average between the shortest and longest height of the layer. Finally, effective length of a given layer is used in DFT computations to obtain the permittivity of that layer (see Section 4.2.2).

4.2.2 Permittivity from DFT Computations

Information about structural, electronic, magnetic, and chemical properties of a material can be obtained by studying the quantum mechanical wave function of its electrons. However, computation of the wave functions in a many-electron system from the approximation-free solution of the Schrödinger equation is not easy if not impossible. The DFT overcomes this problem by using density functional of electrons as the quantity of interest instead of the wave function. Indeed, all related information of a material can also be retrieved from the density functional of electrons [86, 87]. The DFT formulates the many-electron problem in a material/crystal with fixed nuclei (i.e. under Born-Oppenheimer approximation) using a self-consistent density functional. Even after this simplification, electron density functional cannot be solved for using analytical methods and a numerical scheme has to be used for this purpose [89]. In this work, the DFT computations are carried out using the commercially-available WIEN2k solver [8], which makes use of the full potential linearized augmented plane wave (FP-LAPW) method [90]. Additionally, WIEN2k solver uses the generalized gradient approximation (Perdew-Burke-Ernzerhof functional) to account for the ex-

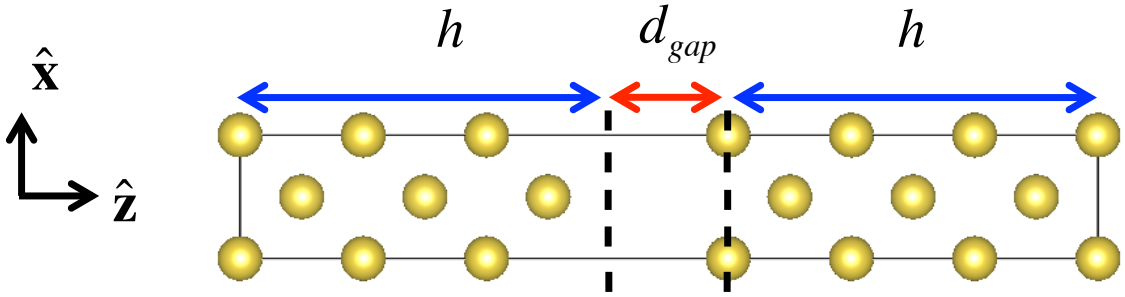

Figure 4.3: Supercell with gap.

change correlation interaction [91]. The rest of this section describes how the permittivity of the bulk material and auxiliary tunnel is computed.

In the framework of DFT, the many-electron problem is reduced to a single-particle type Schrödinger equations given by [86, 87]

$$H\psi_{n,\mathbf{k}}(\mathbf{r}) = E_{n,\mathbf{k}}\psi_{n,\mathbf{k}}(\mathbf{r}). \tag{4.1}$$

The Hamiltonian H includes the kinetic and potential energy terms. $E_{n,\mathbf{k}}$ is the energy of the particle at that state $\psi_{n,\mathbf{k}}(\mathbf{r})$ which is known as Kohn-Sham state. $\psi_{n,\mathbf{k}}(\mathbf{r})$ are expanded in terms of known basis functions [9, 89] $\phi_{\mathbf{k}+\mathbf{G}}(\mathbf{r})$ and unknown coefficients $C_{n,\mathbf{k}}(\mathbf{G})$ in the reciprocal space as

$$\psi_{n,\mathbf{k}}(\mathbf{r}) = \sum_{\mathbf{G}} C_{n,\mathbf{k}}(\mathbf{G})\phi_{\mathbf{k}+\mathbf{G}}(\mathbf{r}). \tag{4.2}$$

Here $\mathbf{G}$ are the reciprocal lattice vectors. Equation (4.1) is solved by using (4.2) and minimizing the material energy to obtain $C_{n,\mathbf{k}}(\mathbf{G})$ and hence $\psi_{n,\mathbf{k}}(\mathbf{r})$. This solution gives correct density for the ground state, but for the computation of permittivity knowledge of excited states are needed. Here, Kohn-Sham states are interpreted as excited states to compute the permittivity. This assumption is valid for metals as shown in the literature [9,88]. However, for semi-conductors further study needed such as solution of Bethe-Salpeter equation [92] which includes electron-hole interaction.

The dielectric permittivity is given in reciprocal space by Linhard formula [93]

$$\varepsilon(\mathbf{q},\omega) = 1 - \lim_{\alpha\to 0} \frac{8\pi q_e^2}{\mathbf{q}^2\Omega} \sum_{n,n',\mathbf{k}} \langle n,\mathbf{k}|n',\mathbf{k}+\mathbf{q}\rangle^2 \frac{(f(E_{n,\mathbf{k}}) - f(E_{n',\mathbf{k}+\mathbf{q}}))}{E_{n,\mathbf{k}} - E_{n',\mathbf{k}+\mathbf{q}} - \hbar\omega + \mathrm{j}\alpha\omega} \tag{4.3}$$

Here, $\hbar$ is the reduced Planck constant, q_e is the charge of the electron, Ω is the volume of the supercell, $f(E_{n,\mathbf{k}})$ is the Fermi distribution, $\mathbf{k}$ is the crystal wave vector, and the bra-ket notation $\langle n,\mathbf{k}|n',\mathbf{k}+\mathbf{q}\rangle = \psi^*_{n,\mathbf{k}}\psi_{n',\mathbf{k}+\mathbf{q}}$ is employed. Upon taking the limit, the imaginary part of (4.3) can be written as

$$\begin{aligned}&\mathrm{Im}\{\varepsilon(\mathbf{q},\omega)\} = \\ &\frac{8\pi^2 q_e^2}{\mathbf{q}^2\Omega} \sum_{n,n',\mathbf{k}} \langle n,\mathbf{k}|n',\mathbf{k}+\mathbf{q}\rangle^2 (f(E_{n,\mathbf{k}}) - f(E_{n',\mathbf{k}+\mathbf{q}}))\delta(E_{n,\mathbf{k}} - E_{n',\mathbf{k}+\mathbf{q}} - \hbar\omega)\end{aligned} \tag{4.4}$$

where the definition of Dirac delta function $\delta(x) = \lim_{\alpha\to 0} \frac{1}{\pi}\frac{\alpha}{\alpha^2+x^2}$ is employed. Note that permittivity given in (4.3) is non-local, i.e. it explicitly depends on the wave vector $\mathbf{q}$. However, it is shown that the effect of non-locality is less pronounced than the quantum tunneling [76], therefore here a local permittivity model is used. This is achieved by taking the limit $\mathbf{q}\to\mathbf{0}$. Since $\mathbf{q}$ is a vector quantity, dielectric permittivity is written as a 3×3 tensor $\bar{\bar{\varepsilon}}^{\mathrm{DFT}}(\omega) = \bar{\bar{\varepsilon}}^{\mathrm{inter}}(\omega) + \bar{\bar{\varepsilon}}^{\mathrm{intra}}(\omega)$ with interband ($n \neq n'$) and intraband ($n = n'$) contributions. The imaginary part of interband contribution $\mathrm{Im}\{\bar{\bar{\varepsilon}}^{\mathrm{inter}}(\omega)\}$ is given by [9, 88, 93]

$$\begin{aligned}&\mathrm{Im}\{\bar{\bar{\varepsilon}}^{\mathrm{inter}}_{zz}(\omega)\} = \\ &\frac{\hbar^2 q_e^2}{\pi m_e^2\omega^2} \sum_{n\neq n'} \int_{\mathbf{k}} p^2_{z;n,n',\mathbf{k}} (f(E_{n,\mathbf{k}}) - f(E_{n',\mathbf{k}}))\delta\left(E_{n,\mathbf{k}} - E_{n',\mathbf{k}} - \hbar\omega\right) d^3k,\end{aligned} \tag{4.5}$$

which takes into account all transitions between different ($n \neq n'$) states. In (4.5), m_e is the mass of the electron, $p_{z;n,n',\mathbf{k}}$ is the momentum matrix element along z-direction

that is found by perturbation theory [9, 93] for small $\mathbf{q}$ as

$$\langle n, \mathbf{k} | n', \mathbf{k}+\mathbf{q} \rangle^2 = \delta_{n,n'} - (1-\delta_{n,n'}) \frac{\hbar \mathbf{p}_{n,n',\mathbf{k}} \cdot \mathbf{q}}{m_e (E_{n,\mathbf{k}} - E_{n',\mathbf{k}})}. \tag{4.6}$$

The real part of the interband contribution of the dielectric permittivity tensor is computed using the Kramers-Kronig relation [94]

$$\mathrm{Re}\{\bar{\bar{\varepsilon}}^{\mathrm{inter}}_{zz}(\omega)\} = 1 + \frac{2}{\pi} P \int_0^\infty \frac{\omega' \mathrm{Im}\{\bar{\bar{\varepsilon}}^{\mathrm{inter}}_{zz}(\omega')\} d\omega'}{\omega'^2 - \omega^2}, \tag{4.7}$$

where P denotes the principal value integral.

For the intraband contribution, it can be seen that taking the limit $\mathbf{q} \to \mathbf{0}$ of (4.4) will lead to singularities. Therefore, intraband contribution is given by a Drude model

$$\bar{\bar{\varepsilon}}^{\mathrm{intra}}_{zz}(\omega) = 1 - \frac{\omega^2_{p,zz}}{\omega(\omega - \mathbf{j}\gamma)}. \tag{4.8}$$

where γ the lifetime broadening (or damping frequency) is introduced. The plasma frequency $\omega^2_{p,zz}$ is computed by

$$\omega^2_{p,zz} = \frac{\hbar^2 q_e^2}{\pi m_e^2} \sum_n \int_{\mathbf{k}} p^2_{z;n,n,\mathbf{k}} \delta\left(E_{n,\mathbf{k}} - E_F\right) d^3k, \tag{4.9}$$

where E_F is the Fermi energy and n runs over all states.

Two different configurations are considered. In the first configuration, for the bulk material, Eq. (4.5)-(4.9) are obtained from the DFT computations on a unit cell of the crystal with periodic boundary conditions [9, 88]. The permittivity tensor $\bar{\bar{\varepsilon}}^{\mathrm{DFT}}(\omega)$ obtained under this configuration gives the permittivity of the bulk material, i.e. $\varepsilon_{\mathrm{bulk}}(\omega) = \bar{\bar{\varepsilon}}^{\mathrm{DFT}}_{zz}(\omega)$. Note that the permittivity tensor has only one independent component due to the symmetry of the crystal. For the second configuration, for the auxiliary tunnel, $p_{z;n,n',\mathbf{k}}$, $\mathrm{Im}\{\bar{\bar{\varepsilon}}^{\mathrm{inter}}_{zz}(\omega)\}$, $\mathrm{Re}\{\bar{\bar{\varepsilon}}^{\mathrm{inter}}_{zz}(\omega)\}$, and $\omega^2_{p,zz}$ are obtained from

the DFT computations on a $1 \times 1 \times 6$ supercell (Fig. 4.3). The gap with length d_{gap} is introduced between two groups of three unit cells, i.e. gap is introduced between two metal blocks of three unit cells. This ensures that the resulting permittivity is not affected by the periodic boundary conditions. Due to the symmetry of the problem the dielectric permittivity tensor has two independent components $\bar{\bar{\varepsilon}}_{xx}^{\text{DFT}}(\omega) = \bar{\bar{\varepsilon}}_{yy}^{\text{DFT}}(\omega)$ and $\bar{\bar{\varepsilon}}_{zz}^{\text{DFT}}(\omega)$, yet here only the permittivity along the z-direction $\bar{\bar{\varepsilon}}_{zz}^{\text{DFT}}(\omega)$ is required, since incident electric field will be along this direction and the length along z-direction is much longer than other directions.

The supercell in Fig. 4.3 can be treated as a layered medium where the effective permittivity is given by $\bar{\bar{\varepsilon}}_{zz}^{\text{DFT}}(\omega)$, which is computed using (4.5)-(4.9). Then the permittivity of the gap $\varepsilon_{\text{gap}}(\omega)$ is obtained using the expression [95]

$$\varepsilon_{\text{gap}}(\omega) = \frac{\bar{\bar{\varepsilon}}_{zz}^{\text{DFT}}(\omega)\varepsilon_{\text{bulk}}(\omega)d_{\text{gap}}}{\varepsilon_{\text{bulk}}(\omega)(2h + d_{\text{gap}}) - 2h\bar{\bar{\varepsilon}}_{zz}^{\text{DFT}}(\omega)}. \tag{4.10}$$

Here, h is the length of metal blocks, i.e. 3 lattice constants. It should be noted here d_{gap} is set to the effective length of the auxiliary tunnel layer as explained in Section 4.2.1, and $\bar{\bar{\varepsilon}}_{zz}^{\text{DFT}}(\omega)$ and $\varepsilon_{\text{gap}}(\omega)$ are computed for every different value of d_{gap}.

4.2.3 Weighted Rational Function Fit

The bulk material and auxiliary tunnel permittivity functions, $\varepsilon_{\text{bulk}}(\omega)$ and $\varepsilon_{\text{gap}}(\omega)$ are formulated and computed in frequency domain as described in Section 4.2.2. Let $\varepsilon(\omega)$ represent $\varepsilon_{\text{bulk}}(\omega)$ and $\varepsilon_{\text{gap}}(\omega)$. To be able to analyze the transient electromagnetic interactions on the nanostructure, one has to carry out simulations in time domain. Consequently, the TD-SIE solver described in Section 4.2.4 requires time domain samples of $\varepsilon(\omega)$, $\bar{\varepsilon}(\omega) = 1/\varepsilon(\omega)$, Green function $G(R,\omega) = e^{-\text{j}\omega R\sqrt{\varepsilon(\omega)\mu}}/4\pi R$, and its spatial derivative $\partial_R G(R,\omega) = \left[-\text{j}\omega\sqrt{\varepsilon(\omega)\mu} - 1/R\right] e^{-\text{j}\omega R\sqrt{\varepsilon(\omega)\mu}}/(4\pi R)$, to

be computed. The transformation from frequency domain to time domain cannot be carried out analytically since frequency domain samples of $\varepsilon(\omega)$ are obtained numerically. Therefore the numerical scheme initially proposed in [7] is used for computing the required time domain samples. This scheme is briefly described next.

Let $F(\omega)$ represent any one of $\varepsilon(\omega)$, $\bar{\varepsilon}(\omega)$, $G(R,\omega)$, and $\partial_R G(R,\omega)$. It is assumed that in a given frequency band $F(\omega)$ can be approximated using rational functions as

$$F(\omega) \approx d + \mathrm{j}\omega f + \sum\nolimits_{k=1}^{N} \{b_k/[\mathrm{j}\omega + a_k]\}. \tag{4.11}$$

Here, N is the number of rational functions, d and f are constants (which can explicitly be enforced to be zero) and a_k and b_k are the poles and the residues associated with the rational functions. To find unknown the coefficients, d, f, a_k, and b_k, FRVF [57–59] algorithm is used. The FRVF scheme minimizes the difference between the samples of $F(\omega)$ and the right hand side of (4.11) (computed in the given frequency band) to find the unknown coefficients. It should be noted here that during this operation, it is enforced that d and f are real valued, and a_k, and b_k are real valued or come complex conjugate pairs. Additionally, the FRVF scheme chooses stable poles, i.e., the resulting a_k satisfy $\mathrm{Re}\{a_k\} > 0$. Once the coefficients are obtained, one can find the time domain expression for $F(t)$ by inverse Fourier transforming (4.11):

$$\mathcal{F}^{-1}\{F(\omega)\} \approx d\delta(t) + f\delta'(t) + \sum\nolimits_{k=1}^{N} b_k u(t) e^{a_k t}. \tag{4.12}$$

Here, $\delta'(.)$ is the first derivative of Dirac delta function and $u(.)$ is the unit step function. The expression in (4.12) allows $\varepsilon(t)$, $\bar{\varepsilon}(t)$, $G(R,t)$, and $\partial_R G(R,t)$ to be computed in closed form in time domain.

4.2.4 TD-PMCHWT-SIE

In this section, formulation given in Chapter 3 is generalized to multiple nanostructures. Let $V = \cup_{p=1}^{P} V_p$ represent the total volume of the combined structure consisting of the nanostructures and the auxiliary tunnel. Each one of the nanostructures and the layers of the tunnel is assigned a volume represented with V_p , $p = 1, 2, .., P$. The combined structure resides in an unbounded non-dispersive background medium represented with V_0. The permittivity and inverse permittivity of V_p are denoted by $\varepsilon_p(t)$ and $\bar{\varepsilon}_p(t)$, respectively. For $p = 0$, permittivity is constant, i.e. $\varepsilon_0(t) = \varepsilon_0$ and $\bar{\varepsilon}_0(t) = 1/\varepsilon_0$. All volumes are non-magnetic with the constant permeability $\mu_p = \mu_0$, $p = 0, 1, .., P$. The surface between the two volumes V_q and V_p is represented by S_l,$l = 1, 2, ..., L$, $p, q = 0, ..., P$, $p \neq q$, and $\hat{\mathbf{n}}_l(\mathbf{r})$ is the unit normal vector on S_l pointing towards V_p. Let $\{\mathbf{E}_p^{\text{inc}}(\mathbf{r}, t), \mathbf{H}_p^{\text{inc}}(\mathbf{r}, t)\}$ and $\{\mathbf{E}_p^{\text{sca}}(\mathbf{r}, t), \mathbf{H}_p^{\text{sca}}(\mathbf{r}, t)\}$ represent incident and scattered electromagnetic fields in V_p, respectively. It is assumed that $\mathbf{E}_p^{\text{inc}}(\mathbf{r}, t)$ and $\mathbf{H}_p^{\text{inc}}(\mathbf{r}, t)$ are vanishingly small $\forall \mathbf{r} \in V$, $t < 0$ and essentially band limited to $f_{\max}$. The fields $\{\mathbf{E}_p^{\text{inc}}(\mathbf{r}, t), \mathbf{H}_p^{\text{inc}}(\mathbf{r}, t)\}$ and $\{\mathbf{E}_p^{\text{sca}}(\mathbf{r}, t), \mathbf{H}_p^{\text{sca}}(\mathbf{r}, t)\}$ satisfy two boundary conditions for $\mathbf{r} \in S_l$:

$$\hat{\mathbf{n}}_l(\mathbf{r}) \times \left[\partial_t \mathbf{E}_p^{\text{inc}}(\mathbf{r}, t) - \partial_t \mathbf{E}_q^{\text{inc}}(\mathbf{r}, t)\right]\Big|_{\mathbf{r}\in S_l} = -\hat{\mathbf{n}}_l(\mathbf{r}) \times \left[\partial_t \mathbf{E}_p^{\text{sca}}(\mathbf{r}, t) - \partial_t \mathbf{E}_q^{\text{sca}}(\mathbf{r}, t)\right]\Big|_{\mathbf{r}\in S_l} \tag{4.13}$$

$$\hat{\mathbf{n}}_l(\mathbf{r}) \times \left[\partial_t \mathbf{H}_p^{\text{inc}}(\mathbf{r}, t) - \partial_t \mathbf{H}_q^{\text{inc}}(\mathbf{r}, t)\right]\Big|_{\mathbf{r}\in S_l} = -\hat{\mathbf{n}}_l(\mathbf{r}) \times \left[\partial_t \mathbf{H}_p^{\text{sca}}(\mathbf{r}, t) - \partial_t \mathbf{H}_q^{\text{sca}}(\mathbf{r}, t)\right]\Big|_{\mathbf{r}\in S_l}. \tag{4.14}$$

Using surface equivalence principle, one can express $\{\mathbf{E}_p^{\text{sca}}(\mathbf{r}, t), \mathbf{H}_p^{\text{sca}}(\mathbf{r}, t)\}$ in terms of electric current density $\mathbf{J}_l(\mathbf{r}, t)$ and magnetic current density $\mathbf{M}_l(\mathbf{r}, t)$ introduced on

S_l [55]:

$$\partial_t \mathbf{E}_p^{\mathrm{sca}}(\mathbf{r},t) = \sum\nolimits_{l'} \left[\mathcal{L}_p\{\mu_0 \mathbf{J}_{l'}(\mathbf{r},t)\} - \mathcal{Q}_p\{\bar{\varepsilon}_p(t) * \mathbf{J}_{l'}(\mathbf{r},t)\} + \mathcal{K}_p\{\mathbf{M}_{l'}(\mathbf{r},t)\}\right] \quad (4.15)$$

$$\partial_t \mathbf{H}_p^{\mathrm{sca}}(\mathbf{r},t) = \sum\nolimits_{l'} \left[\mathcal{L}_p\{\varepsilon_p(t) * \mathbf{M}_{l'}(\mathbf{r},t)\} - \mathcal{Q}_p\{\mu_0^{-1} \mathbf{M}_{l'}(\mathbf{r},t)\} - \mathcal{K}_p\{\mathbf{J}_{l'}(\mathbf{r},t)\}\right]. \quad (4.16)$$

In (4.15) and (4.16), the summation index l' runs over the indices of the surfaces that "touches" V_p and integral operators are defined as

$$\begin{aligned}
\mathcal{L}_p\{\mathbf{X}_{l'}(\mathbf{r},t)\} &= \int_{S_{l'}} G_p(R,t) * \partial_t^2 \mathbf{X}_{l'}(\mathbf{r}',t) d\mathbf{r}' \\
\mathcal{Q}_p\{\mathbf{X}_{l'}(\mathbf{r},t)\} &= \nabla \int_{S_{l'}} G_p(R,t) * \nabla' \cdot \mathbf{X}_{l'}(\mathbf{r}',t) d\mathbf{r}' \\
\mathcal{K}_p\{\mathbf{X}_{l'}(\mathbf{r},t)\} &= \nabla \times \int_{S_{l'}} G_p(R,t) * \partial_t \mathbf{X}_{l'}(\mathbf{r}',t) d\mathbf{r}'.
\end{aligned} \quad (4.17)$$

Here, $G_p(R,t)$ is the Green function of the unbounded medium that has the same permittivity and permeability as V_p ($\varepsilon_p(t)$ and μ_p), $R = |\mathbf{r} - \mathbf{r}'|$ is the distance between points $\mathbf{r}$ and $\mathbf{r}'$ and "$*$" denotes temporal convolution. It should be noted here that for $p = 0$, temporal convolutions in (4.15)-(4.17) are simplified using the fact that $\varepsilon_0(t) = \varepsilon_0$, $\bar{\varepsilon}_0(t) = 1/\varepsilon_0$, $G_0(R,t) = \delta(t - R\sqrt{\varepsilon_0\mu_0})/(4\pi R)$. For $p = 1, 2, .., P$, $\varepsilon_p(t)$, $\bar{\varepsilon}_p(t)$, $G_p(R,t)$ are computed as described in Sections 4.2.2 and 4.2.3. Inserting (4.15) and (4.16) into (4.13) and (4.14) yields TD-PMCHWT-SIE [7] in unknown $\mathbf{J}_l(\mathbf{r},t)$ and $\mathbf{M}_l(\mathbf{r},t)$. To numerically solve the TD-PMCHWT-SIE, S_l are discretized into triangular patches and unknowns $\mathbf{J}_l(\mathbf{r},t)$ and $\mathbf{M}_l(\mathbf{r},t)$ are expanded using the Rao-Wilton-Glisson (RWG) functions [40] $\mathbf{f}_n^l(\mathbf{r})$ in space and Lagrange interpolation functions $T(t)$ in time [23, 33]:

$$\mathbf{J}_l(\mathbf{r},t) = \sum\nolimits_{j=1}^{N_{\mathrm{t}}} \sum\nolimits_{n=1}^{N_{\mathrm{s}}^l} J_{jn}^l T(t - j\Delta t) \mathbf{f}_n^l(\mathbf{r}) \quad (4.18)$$

$$\mathbf{M}_l(\mathbf{r},t) = \sum\nolimits_{j=1}^{N_{\mathrm{t}}} \sum\nolimits_{n=1}^{N_{\mathrm{s}}^l} M_{jn}^l T(t - j\Delta t) \mathbf{f}_n^l(\mathbf{r}). \quad (4.19)$$

Here, Δt is time step size, $N_{\rm t}$ is number of time steps, and $N_{\rm s}^l$ is the number of RWG basis functions on surface S_l, and J_{jn}^l and M_{jn}^l are the unknown current coefficients. Inserting (4.18)-(4.19), into the TD-PMCHWT-SIE and testing the resulting equation with $\mathbf{f}_m^l(\mathbf{r})\delta(t-i\Delta t)$, $m=1,2,..,N_s^l$, $l=1,2,..,L$, yield [55]

$$\bar{\bar{Z}}_0\bar{I}_i = \bar{V}_i - \sum\nolimits_{j=1}^{i-1} \bar{\bar{Z}}_{i-j}\bar{I}_j. \tag{4.20}$$

Here, $\bar{I}_i$ and $\bar{V}_i$ store the unknown coefficients $J_{n,i}^l$ and $M_{n,i}^l$ and the tested incident fields, and $\bar{\bar{Z}}_{i-j}$ are the MOT matrices, respectively. The elements of $\bar{\bar{Z}}_{i-j}$ call for the computation of a several types of spatio-temporal convolutions involving $\varepsilon_p(t)$, $\bar{\varepsilon}_p(t)$, $G_p(R,t)$, $\partial_R G_p(R,t)$, $T(t)$, and $\mathbf{f}_n^l(\mathbf{r})$. These convolutions are computed efficiently using the method described in Chapter 3 and in [7, 56]. Special care is taken while computing the contributions from junctions as explained in [96]. Once $\bar{\bar{Z}}_{i-j}$ are computed, $\bar{I}_i$ is obtained recursively by time marching, as described next [55]. First, $\bar{I}_1$ (at time Δt) is found by solving (4.20) with right-hand side $\bar{V}_1(i=1\ )$. $\bar{I}_1$ is then used to compute $\bar{\bar{Z}}_1\bar{I}_1$ which is added to $\bar{V}_2$ to yield the right-hand side of (4.20) at time $2\Delta t$. $\bar{I}_2$ is found by solving (4.20) with this right-hand side ($i=2\ $). Then, $\bar{I}_1$ and $\bar{I}_2$ are used to compute $\bar{\bar{Z}}_2\bar{I}_1+\bar{\bar{Z}}_1\bar{I}_2$ which is added to $\bar{V}_3$ to yield the right-hand side at time $3\Delta t$ and permit the solution of (4.20) for $\bar{I}_3$, and so on. At the end of time marching, all $\bar{I}_i$, $i=1,2,...,N_t$, are computed and known.

4.3 Numerical Results

4.3.1 Permittivity Values

In the DFT calculations, the accurate full potential linearized augmented plane wave method as implemented in the WIEN2k package [8] is used. The generalized gradient approximation (Perdew-Burke-Ernzerhof functional) is employed to treat the exchange correlation interaction. Both systems, Au and Ag, are face-centered cubic

belonging to space group $Fm\bar{3}m$ (No. 225) with experimental lattice constants of 0.407 and 0.408 nm [97]. First, the crystal structures are fully optimized and the equilibrium lattice constants of 0.408 nm and 0.409 nm are obtained for Au and Ag, respectively. These optimized lattice constants are used to further study the permittivity of the bulk materials as well as the gapped materials. To study the effect of the gap distance on permittivity, a $1 \times 1 \times 6$ supercell is used as explained above. A dense $96 \times 96 \times 16$ k-mesh is used. For the total energy convergence, the product $R_{mt}K_{max}$ is set to 7, where R_{mt} is the smallest muffin-tin sphere radius and K_{max} represents the cutoff of the wave function basis. The maximum angular momentum (l_{max}) inside the atomic spheres is taken to be 10, while G_{max} is set to 12 $\mathrm{Ry}^{1/2}$ in the charge density Fourier expansion. The muffin-tin radii for Au and Ag are set to 2.50 bohr. Convergence of the self-consistent calculations is considered to be achieved when succeeding iterations have an energy difference less than 10^{-4} Ry. The permittivity values for the auxiliary tunnel of gold and silver computed by (4.8) are plotted in Figs. 4.4 and 4.5, respectively.

In Figs. 4.6 and 4.7 , the permittivity model obtained by DFT computations is compared to the Johnson-Christy model [60] and the Drude model [6] for bulk ($d_{\mathrm{gap}} = 0$) gold and silver, respectively. Note that $e^{j\omega t}$ convention is used in these figures.

Looking at permittivity values alone will be misleading to understand the effect of the permittivity on the plasmonic properties. Therefore in Figs. 4.8a and 4.8b analytical Mie series solutions of the extinction cross section ($C_{\mathrm{ext}}(\omega)$) are plotted for gold and silver spheres, respectively. The Drude model gives unreliable results with very high plasmon resonances at high energies compared to the Johnson-Christy model. For that reason, in the simulations of Ref. [77], the Johnson-Christy model [60] is used for the permittivity of the nanostructure, while the Drude model used for the auxiliary tunnel. However, using experimental values for the nanostructure and

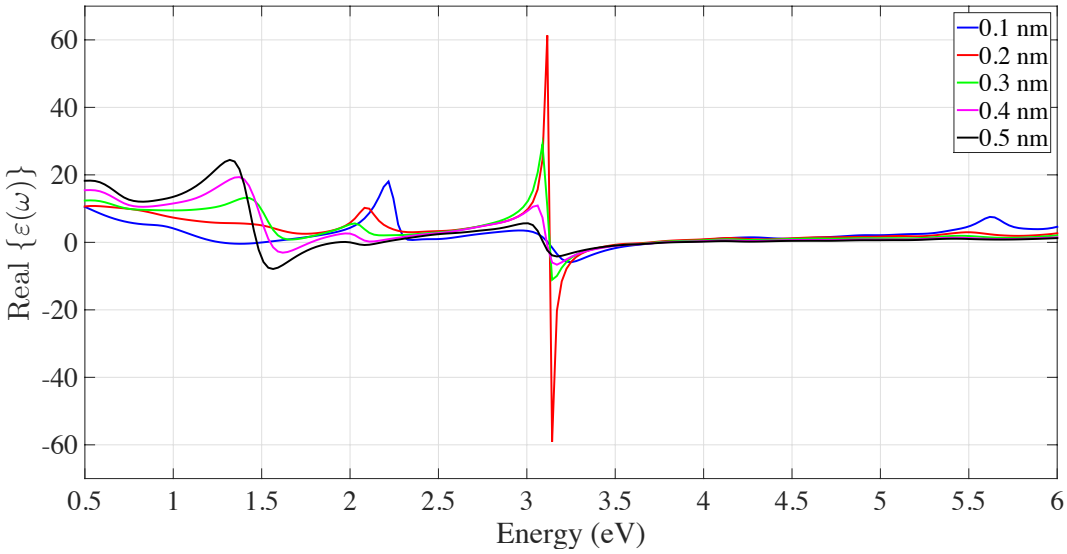

(a)

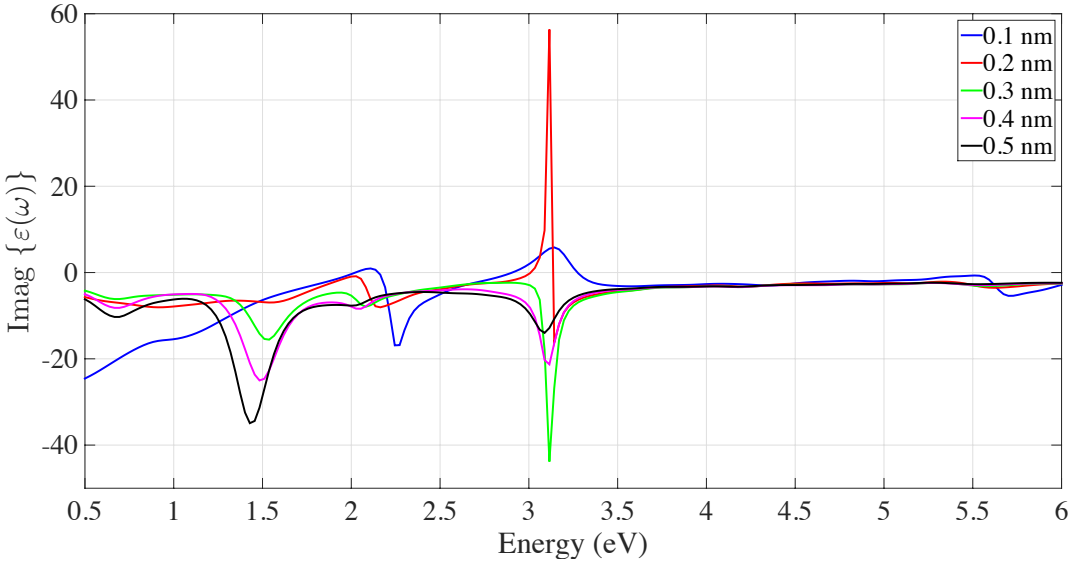

(b)

Figure 4.4: (a) Real and (b) imaginary parts of $\varepsilon_{\text{gap}}(\omega, d_{\text{gap}})$ for gold.

Drude model for the auxiliary tunnel is not consistent, because the permittivity of the auxiliary tunnel should converge to the bulk permittivity when the gap distance goes to zero [6, 76]. This problem is solved here since both permittivities (nanostructure and auxiliary tunnel) are obtained by DFT computations. Hence, in the limit that the gap distance goes to zero, the permittivity of the auxiliary tunnel converges to the bulk value. In Figs. 4.8a and 4.8b, the DFT model provides an extinction spectrum

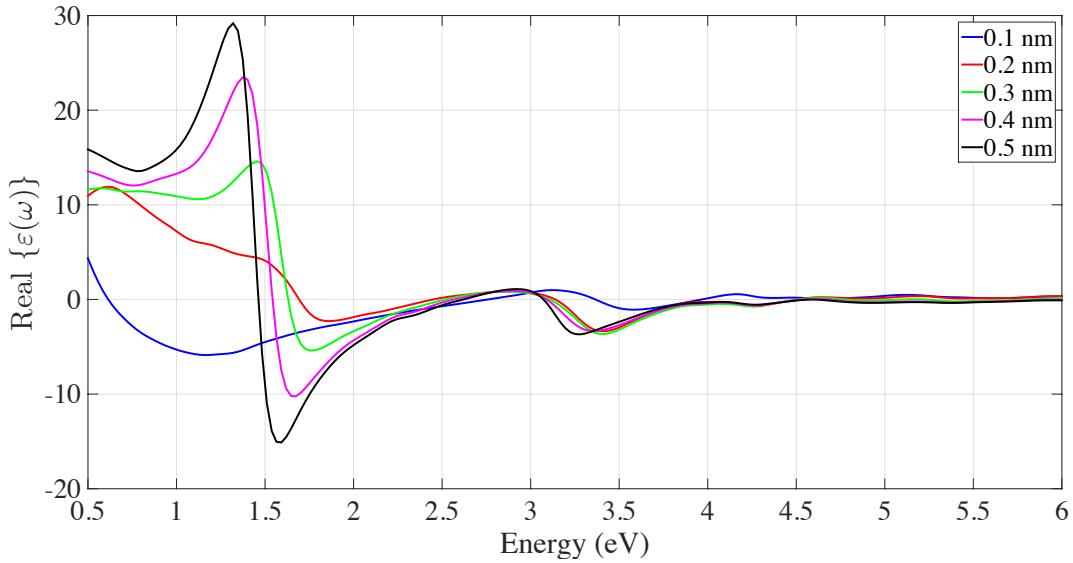

(a)

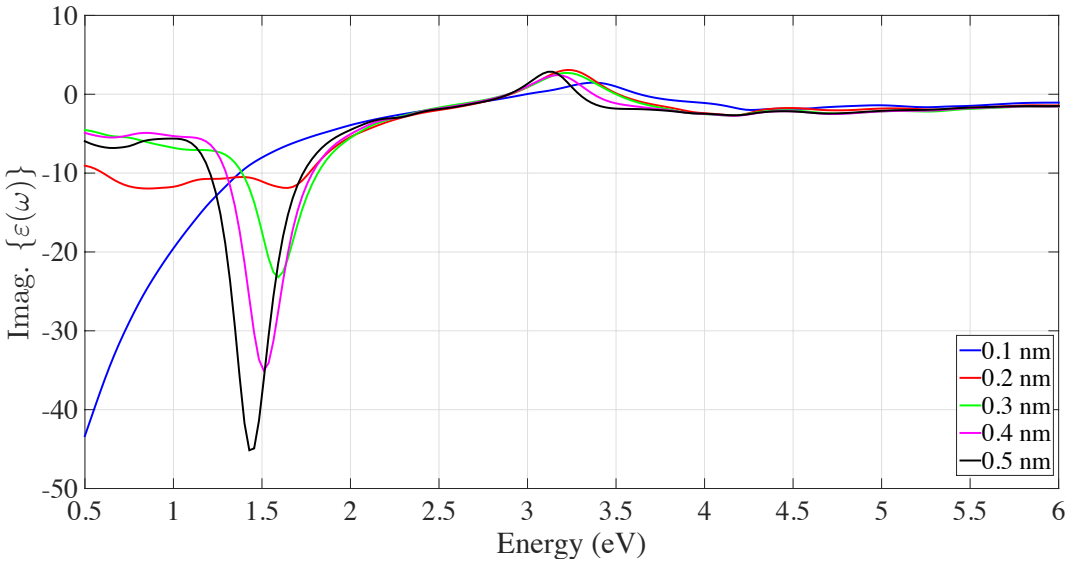

(b)

Figure 4.5: (a) Real and (b) imaginary parts of $\varepsilon_{\text{gap}}(\omega, d_{\text{gap}})$ for silver.

closer to the Johnson-Christy model than the Drude model for gold and silver spheres.

In the following examples, only DFT model is used for the bulk material and the auxiliary tunnel. It is assumed that the nanostructures are residing in free space and

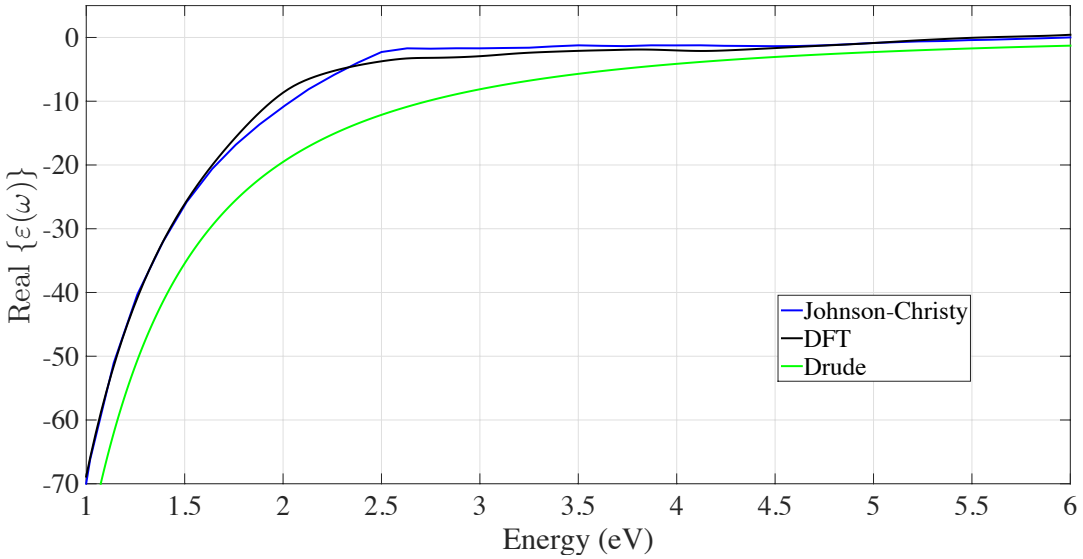

(a)

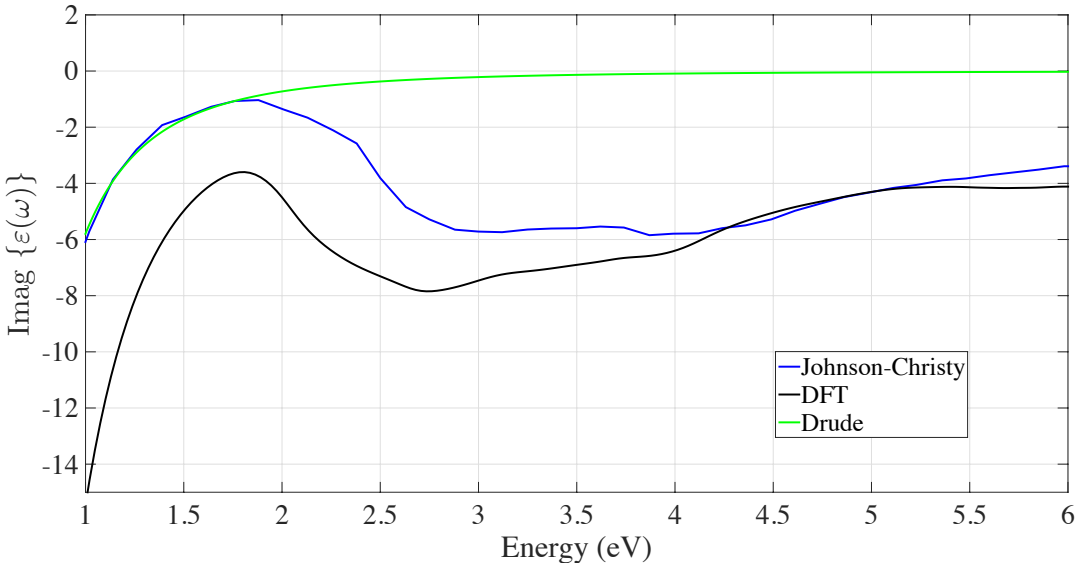

(b)

Figure 4.6: (a) Real and (b) imaginary parts of $\varepsilon(\omega)$ for bulk gold.

excited only from free space by a plane wave with electric field

$$\mathbf{E}_0^{\text{inc}}(\mathbf{r}, t) = \hat{\mathbf{p}} E_0^{\text{inc}} G(t - \hat{\mathbf{k}} \cdot \mathbf{r}/c_0), \tag{4.21}$$

where E_0^{inc} is the amplitude, $\hat{\mathbf{p}}$ is the polarization unit vector, $\hat{\mathbf{k}}$ is the unit vector along the direction of propagation, $G(t) = \cos(2\pi f_0[t - t_0])e^{-(t-t_0)^2/2\sigma^2}$ is a Gaussian

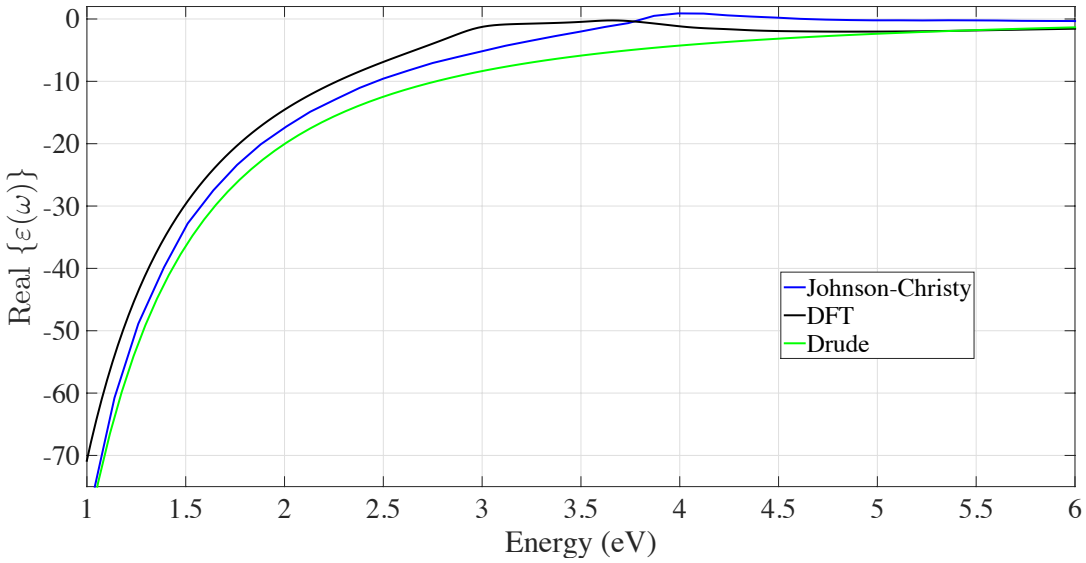

(a)

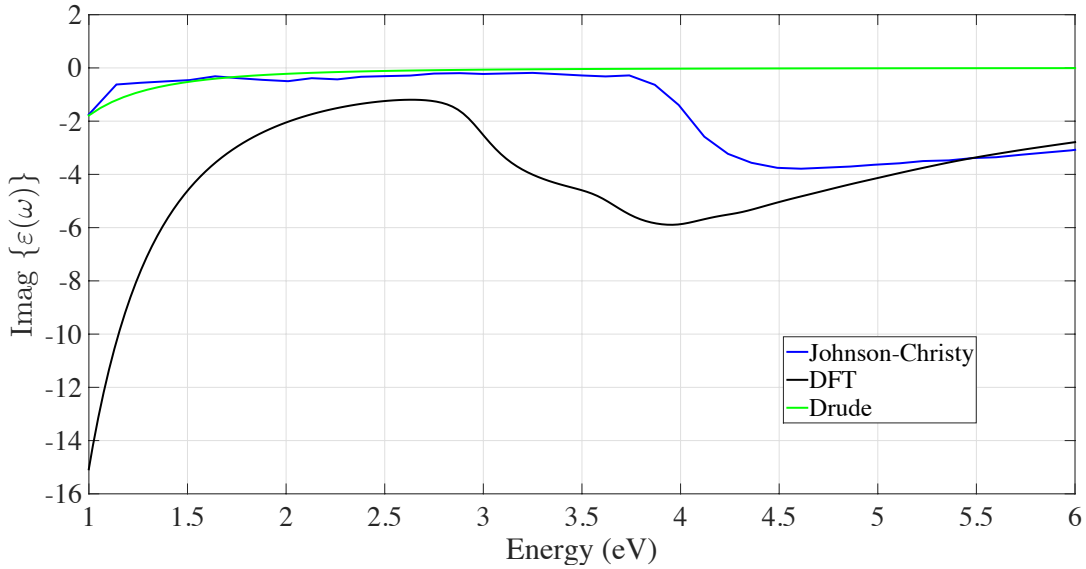

(b)

Figure 4.7: (a) Real and (b) imaginary parts of $\varepsilon(\omega)$ for bulk silver.

pulse with modulation frequency f_0, duration σ, and delay t_0. In all examples, $t_0 = 8\sigma$ and $\sigma = 3/(2\pi f_{\text{bw}})$, where f_{bw} denotes an effective bandwidth. After the time domain simulation is completed, equivalent electric and magnetic current densities are converted to frequency domain by using the discrete time Fourier transform with proper normalization. This is followed by the computation of the extinction cross section in frequency domain.

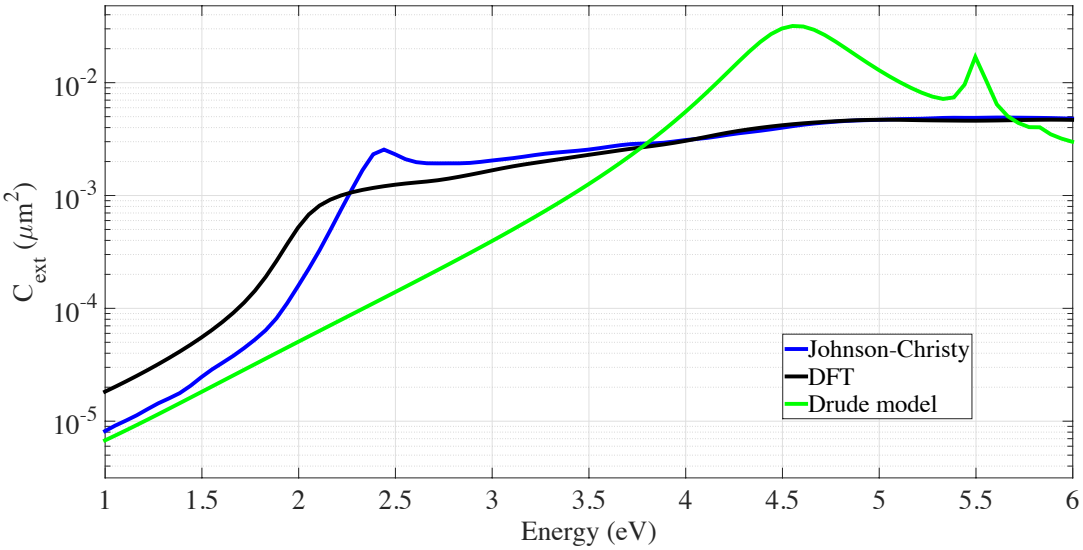

(a) Gold sphere, radius of 25 nm.

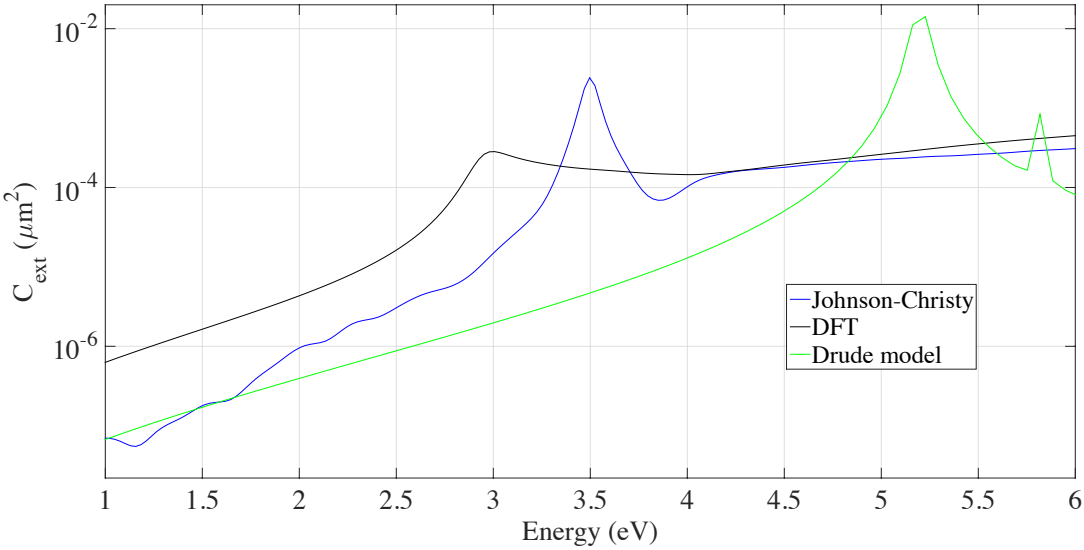

(b) Silver sphere, radius of 10 nm.

Figure 4.8: $C_{\text{ext}}(\omega)$ obtained from Mie Series solution for different permittivity models.

4.3.2 Gold and Silver Spheres

In the first example, accuracy of the proposed classical electromagnetic solver is tested by comparing extinction cross section computed with the TD-SIE solver to the Mie series solution for gold and silver spheres in Fig. 4.9a and 4.9b, respectively. The excitation parameters are $\hat{\mathbf{p}} = \hat{\mathbf{x}}$, $\hat{\mathbf{k}} = \hat{\mathbf{z}}$, $f_0 = 785$ THz, and $f_{\text{bw}} = 665$ THz.

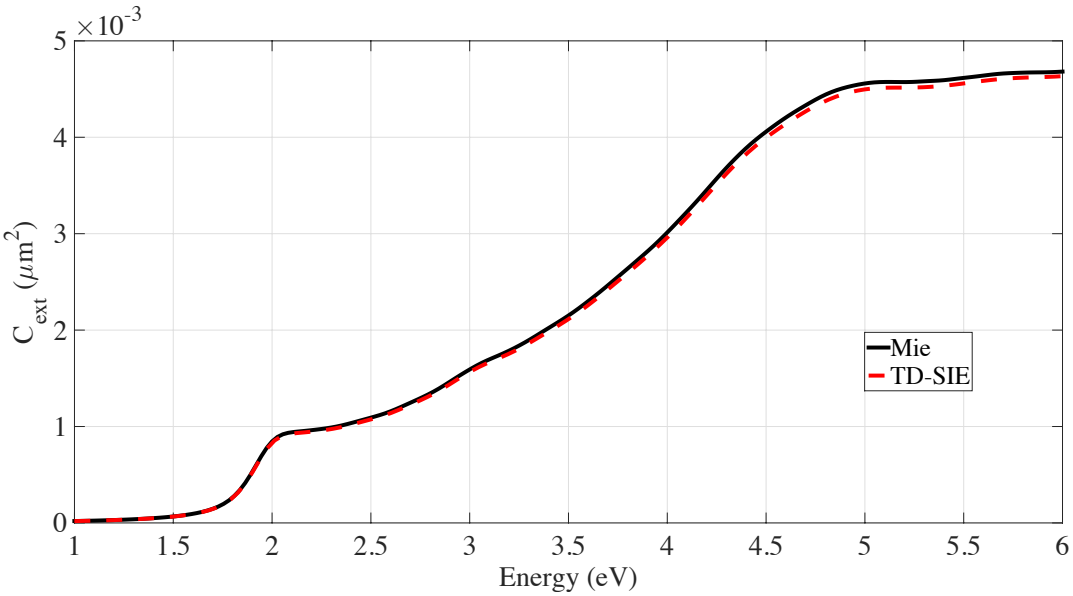

(a) Gold sphere, radius of 25 nm.

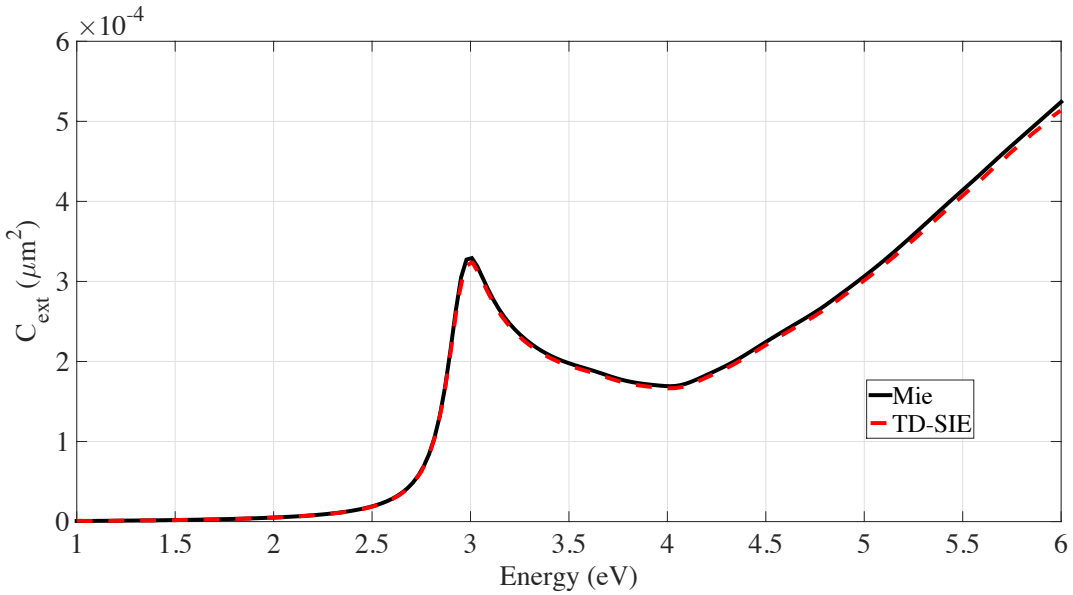

(b) Silver sphere, radius of 10 nm.

Figure 4.9: Comparison of $C_{\text{ext}}(\omega)$ obtained from Mie Series and TD-PMCHWT-SIE solutions.

The currents induced on the sphere surface are discretized using $N_{\text{s}} = 1509$ RWG basis functions and the simulation is executed for $N_{\text{t}} = 1500$ time steps with step size $\Delta t = 0.03$ fs. Very good match between analytical solver and proposed solver observed.

4.3.3 Gold Dimer

In the next example, a dimer consisting of two gold spheres is analyzed. Spheres have radius of 25 nm and aligned along the z-axis. The excitation parameters are $\hat{\mathbf{p}} = \hat{\mathbf{z}}$, $\hat{\mathbf{k}} = \hat{\mathbf{x}}$, $f_0 = 785$ THz, and $f_{\text{bw}} = 665$ THz. The simulation is executed for $N_{\text{t}} = 1500$ time steps with step size $\Delta t = 0.03$ fs. Fig. 4.10a plots the extinction cross section for the gold dimer without quantum correction, i. e. without an auxiliary tunnel. For each gap distance, figure is shifted vertically to see the effect of gap distance on plasmon resonance. Spheres are discretized with $N_{\text{s}} = 2676$ RWG basis functions. Main plasmon resonance redshifts as expected from classical simulations [6, 76].

In Fig. 4.10b, extinction cross section of the gold dimer with quantum correction, i. e. with an auxiliary tunnel, for various gap distances are plotted. The numbers of layers used in the auxiliary tunnel for the gap distances 0.1 nm, 0.2 mn, 0.3 nm, 0.4 nm, and 0.5 nm are 4, 4, 3, 2, and 1, respectively. The currents induced on the surfaces of nanostructure are discretized using a maximum of $N_{\text{s}} = 2808$ RWG basis functions for the shortest distance 0.1 nm. Unlike the first classical case without the auxiliary tunnel, main plasmon resonance at 1.902 eV blueshifts to 1.976 eV as the gap distance reduces to 0.1 nm. In addition, a second plasmon resonance emerges at 1.2 eV due to the quantum correction, and first redshifts then blueshifts to 1.16 eV.

Convergence of the extinction cross section with the increasing number of layers to model the auxiliary tunnel is depicted in Fig. 4.11 for the same gold dimer. The gap distance is set to 0.1 nm and four different cases are analyzed where the numbers of layers are 1, 3, 4, and 7. Convergence is achieved for 4 layers, therefore 4 layered tunnel model is used for the shortest gap distance of 0.1 nm in Fig. 4.10b. The number of layers reduces as the gap distance increases such that a single layer is used for the gap distance of 0.5 nm.

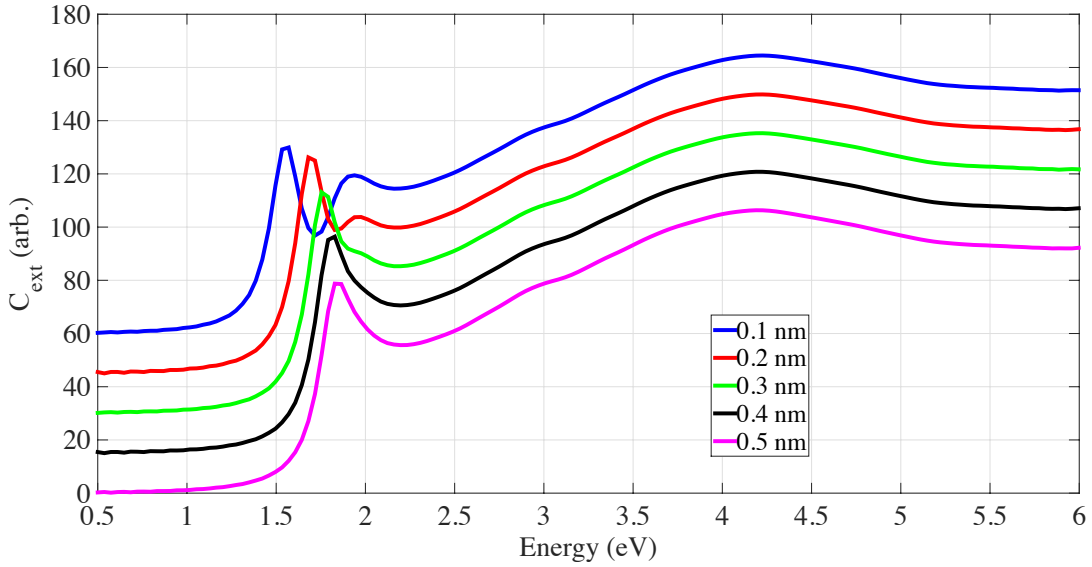

(a) No tunnel.

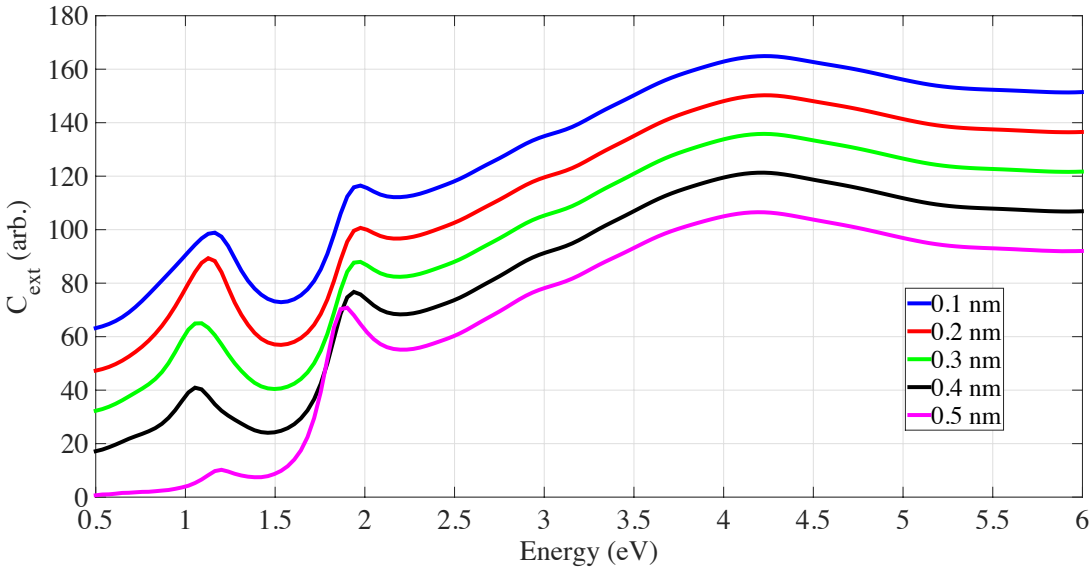

(b) Auxiliary tunnel.

Figure 4.10: $C_{\text{ext}}(\omega)$ computed for gold dimer.

4.3.4 Silver Dimer

In this example, a silver dimer consisting of two silver spheres is analyzed. Spheres have a radius of 10 nm and aligned along the z-axis. The excitation parameters are $\hat{\mathbf{p}} = \hat{\mathbf{z}}$, $\hat{\mathbf{k}} = \hat{\mathbf{x}}$, $f_0 = 506$ THz, and $f_{\text{bw}} = 493$ THz. The simulation is executed for $N_{\text{t}} = 1500$ time steps with step size $\Delta t = 0.03$ fs. Fig. 4.12a plots the extinction

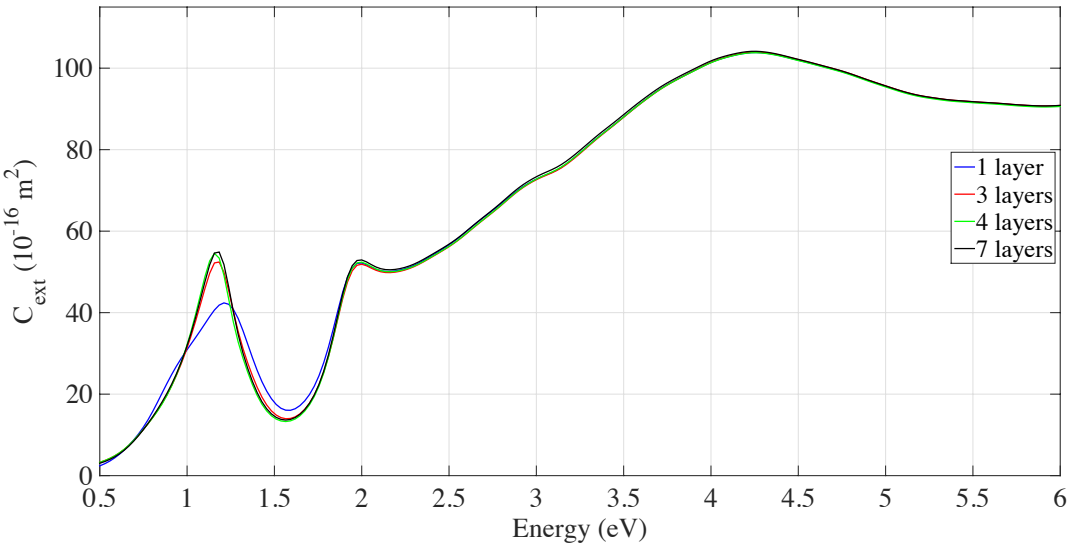

Figure 4.11: Convergence of $C_{\text{ext}}(\omega)$ with increasing number of layers.

cross section for the silver dimer without quantum correction. Spheres are discretized with $N_{\text{s}} = 2292$ RWG basis functions. Main plasmon resonance redshifts from 2.55 eV to 2.1 eV as the gap reduces to 0.1 nm. The second plasmon resonance at 2.85 eV redshifts to 2.62 eV and another resonance appears at 2.81 eV as the gap reduces to 0.1 nm.

In Fig. 4.12b, extinction cross section of the silver dimer with quantum correction for various gap distances are plotted. Number of layers used to model the auxiliary tunnel for gap distances 0.1 nm, 0.2 nm, 0.3 nm, 0.4 nm, and 0.5 nm are 4, 4, 3, 2, and 1, respectively. The currents induced on the surfaces of nanostructure are discretized using a maximum of $N_{\text{s}} = 2454$ RWG basis functions. Main plasmon resonance at 2.66 eV blue shifts to 2.76 eV as the gap distance reduces to 0.2 nm and becomes 2.73 eV at 0.1 nm. This result is very close to a charge transfer plasmon seen around 2.9 eV in electron energy loss spectroscopy (EELS) experiments on silver dimers [79]. Although excitation in EELS is different than a plane wave, the EELS experiments are compared to electromagnetic simulations under plane wave excitation in the case of silver cubes and good agreement has been shown [81]. Similarly, both EELS experiments of [79] and simulations in this example analyze the same plasmonic

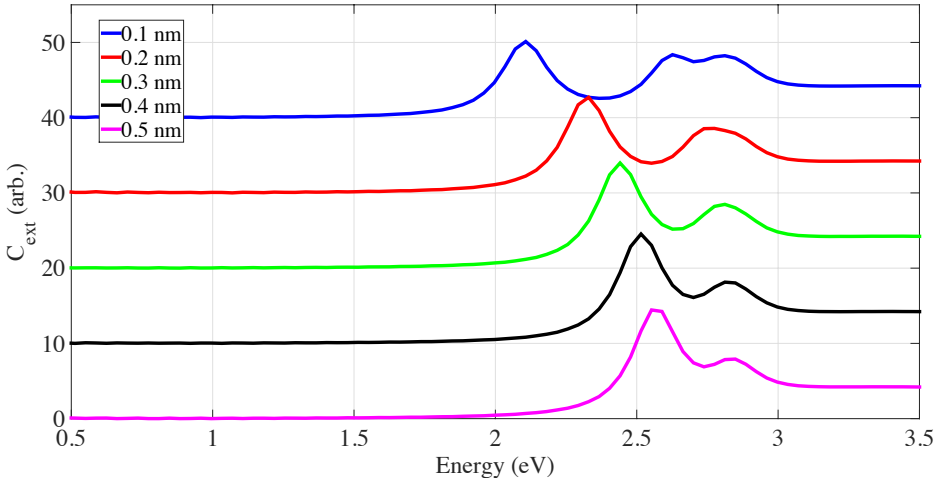

(a) No tunnel.

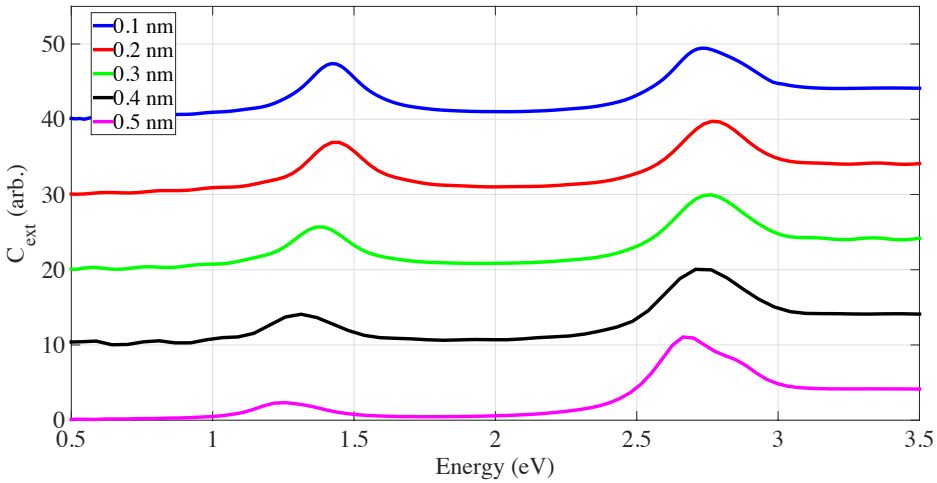

(b) Auxiliary tunnel.

Figure 4.12: $C_{\text{ext}}(\omega)$ computed for silver dimer.

system.

In Fig. 4.12b, another plasmon resonance appears at 1.25 eV that blue shifts to 1.42 eV when gap reduces to 0.1 nm, whereas EELS experiments of [79] reveal a charge transfer plasmon around 1.3 eV just after contact. Proposed scheme predicts a plasmon in the same energy level, yet before contact. This discrepancy might be due to the fact that measurements have a limited spatial resolution 0.3-0.4 nm and an error of ± 0.2 nm is estimated in measurements of gaps [79].

4.4 Conclusion

A quantum corrected TD-SIE solver for plasmonic nanostructures with sub-nanometer gaps is introduced. Dielectric permittivity of closely spaced nanostructures is obtained by DFT computations where the many body problem of electrons is solved taking into account of the atomic structure of materials. Analysis has been done for gold and silver since they are commonly used in plasmonic applications, yet this scheme can be extended to other metals or metal-alkanedithiol-metal structures [82]. After permittivity values are obtained in frequency domain, FRVF algorithm is used to get the time domain permittivity function and Green functions. Then, the scattered electromagnetic fields are computed by the proposed TD-SIE solver. Dimers consisting of gold and silver spheres are analyzed and a charge transfer plasmon is observed with the quantum correction at low energies. Good qualitative agreement between EELS experiments on silver dimers and present work is obtained.

Chapter 5

Conclusion

5.1 Summary

Plasmonics has recently become one of the most exciting research fields of electromagnetics and photonics due its the wide spread applications in bio-medicine and bio-imaging, solar energy, and nanocatalysis [1–3]. Almost all of these applications call for plasmonic nanostructures to manipulate electromagnetic fields. Due to their irregular shape, design and characterization of these structures cannot be carried out using analytical methods. Consequently, one has to use simulation tools capable of solving differential or integral form of Maxwell equations [1, 4] to compute plasmonic fields induced on nanostructures. However, these "classical" electromagnetic solvers become inaccurate when the structures have geometrical dimensions on the order of few nanometers or below. This is simply due to the fact that quantum mechanical effects generated on/between sub-nanometer scale geometry components are not accounted for by these solvers. Tunneling, one of these quantum mechanical effects, occurs when the distance between two nanostructures is smaller than a nanometer. For such short distances, electrons transfer between two structures generating a "non-classical" current path, which is not accounted for by classical electromagnetic solvers as mentioned above.

One way to overcome this problem and accurately analyze plasmonic structures with sub-nanometer gaps is to use quantum mechanical solvers on the whole geometry. But this is computationally very expensive since other geometrical dimensions of

a typical nanostructure are on the order of 10 nm or above. Therefore, a hybrid approach has been developed in [6]. This so-called quantum corrected (QC) model introduces an auxiliary tunnel between the two structures to support the current path generated by tunneling of electrons. The permittivity of this auxiliary tunnel was retrieved from the solution of a one-dimensional (1D) Schrödinger equation while the permittivity of the nanostructures presented using a Drude model. Electromagnetic field interactions on the resulting combined structure (nanostructures and auxiliary tunnel) are computed using a frequency domain surface integral equation solver (FD-SIE).

This QC-FD-SIE solver suffers from two bottlenecks: (i) It is inefficient for producing broadband results since it has to be run once per frequency sample. (ii) 1D Schrödinger equation (used for producing the permittivity of the tunnel) is not accurate when used in modeling three-dimensional (3D) crystal structure of metals [85]. (iii) Drude model (used for producing the permittivity of the structures) does not match models generated using experimentally measured permittivity values [49] .

The solver developed in this work is designed to address these bottlenecks. More specifically, a QC time domain surface integral equation (TD-SIE) solver is proposed for accurately analyzing plasmonic nanostructures with sub-nanometer gaps. The permittivity of the auxiliary tunnel is obtained from density functional theory (DFT) computations, which takes into account crystal structure of metals as well as inter-band and intra-band contributions to the permittivity. Transient electromagnetic interactions on the resulting combined structure (nanostructures and auxiliary tunnel) are computed using a time domain Poggio-Miller-Chan-Harrington-Wu-Tsai surface integral equation (TD-PMCHWT-SIE) solver [7]. This TD-SIE solver requires samples of the time domain permittivity function and Green function of each medium (corresponding to nanostructures and the auxiliary tunnel) to be computed. This is carried out using a fast relaxed vector fitting (FRVF) [57–59] algorithm, which gener-

ates time domain expressions of permittivity and Green function from their frequency domain samples.

5.1.1 Contribution of the Thesis

The aim of this work is to formulate and implement a QC-TD-SIE solver to accurately analyze transient electromagnetic field interactions on plasmonic nanostructures with of sub-nanometer gaps. To successfully achieve this goal, several challenges had to be addressed by novel numerical schemes developed during the course of this work.

Time domain permittivity and Green function

The TD-PMCHWT-SIE solver requires samples of the time domain permittivity and the Green function to be computed. For dispersive media, such as metals at optical frequencies, permittivity oftentimes is described in frequency domain. Time domain expressions are limited to mathematical representations such as Drude or Debye models [28]. Even then one may not obtain an analytical expression for the time domain Green function. To overcome this difficulty and to account for experimental models such as Johnson-Christy [60] and Palik [61] in time domain representations, a numerical approach is adopted in this work. First, FRVF is applied to frequency domain samples of the permittivity and Green function [57–59]. This generates a sequence of rational functions in Laplace domain, whose summation approximates the frequency domain permittivity and Green function. Each rational function has an analytical inverse Laplace transform in time domain. Consequently, this leads to approximate time domain expressions for the permittivity and Green function. These expressions are then used to compute their samples.

Double temporal convolution

Unlike the previously developed TD-SIE solvers [38], the implementation of the TD-PMCHWT-SIE solver formulated in this work calls for discretization of an additional temporal convolution between the permittivity, the Green function, and the

equivalent currents. The combined (double) temporal convolution is discretized into a double discrete summation where the inner summation corresponds to the convolution of the Green function and basis functions (used in discretization of equivalent currents). The multipliers in the outer summation depend only on the medium parameters, therefore they are precomputed per medium without introducing any significant computational burden. For unaccelerated TD-SIE solvers, the multipliers in the outer summation are simply combined with the matrix entries resulting from the convolution of the Green function and basis functions. For accelerated solvers [25,30,32,33]., the outer summation is computed efficiently using blocked-FFTs [30]. Lossy (dissipative) dielectrics are considered before dealing with dispersive media, because lossy media resembles the dispersive media by having a Green function with temporal tail. Moreover, the time domain Green function is analytically well defined that simplifies the formulation of a TD-SIE solver.

Quantum correction by DFT

To increase the accuracy of material and tunnel modeling, permittivity of the nanostructures and the auxiliary tunnel are extracted from DFT computations that accounts for the atomic structure of materials as well as the inter- and intra-band electron contributions. More specifically, the permittivity of metals (bulk material) has been computed accurately using DFT [8,9,88] on a unit cell with periodic boundary conditions. This concept is then generalized to "gapped" materials to account for the auxiliary tunnel and extract its permittivity.

5.2 Future Research Directions

The work presented in this thesis can be extended and improved in several different ways. These are grouped under four categories: (i) improvements on classical electromagnetic solver, (ii) extensions of quantum modeling, (iii) development of numerical schemes solving coupled system of Maxwell and Schrödinger equations, and

(iv) application of the solver to more realistic experimental set-ups.

Improvements on classical electromagnetic solver

The computational complexity of the TD-PMCHWT-SIE solver scales as $O({N_\mathrm{t}}^2{N_\mathrm{s}}^2)$. This computational cost can be reduced to $O(N_\mathrm{t}N_\mathrm{s}^{3/2}\log(N_\mathrm{s})\log(N_\mathrm{t}N_\mathrm{s})\log(N_\mathrm{t}))$ and $O(N_\mathrm{t}N_\mathrm{s}\log^2(N_\mathrm{t})\log(N_\mathrm{s}))$ using fast Fourier transform (FFT)-based schemes [25, 30, 32, 33] and plane wave time domain (PWTD) method [29], respectively. These techniques accelerate the computation of the convolution between the Green function and equivalent currents by making use of the low-rank characteristics of the scattered fields away from the currents. Having said that these techniques have never been used in the presence of double convolutions as described in Chapters 2 and 3. To facilitate their use and maintain the low computational cost of the solution, one has to use incorporate the outer summation in the discretized double convolution into time marching and use blocked FFTs to accelerate its computation [30]. It should be noted here that the use of FFT-based schemes and PWTD method reduces the computational complexity of the TD-PMCHWT-SIE solver to essentially that of finite difference time domain (FDTD) methods.

Extensions of quantum modeling

The DFT computations used for extracting the auxiliary tunnel's permittivity do not account for electron-hole interactions. Although these interactions can accurately be ignored for metals, they become dominant in semi-conductors and insulators. To include the effect of electron-hole interactions in tunnel's effective permittivity, one can use many-body perturbation theory and solve Bethe-Salpeter equation (BSE) [92] on the supercell defined to account for the gap between the two nanostructures.

Solution of the coupled system of Maxwell and Schrödinger equations

The numerical scheme developed in this work models the classical electromagnetic and quantum interactions, separately. The accuracy of the overall solution can be increased by constructing a fully coupled system, i.e. by solving the coupled system of

Maxwell and Schrödinger equations. The validity of this approach has been demonstrated only for theoretical problems [98] or single molecules [99]. Indeed, direct coupling of 3D Maxwell and Schrödinger equations is prohibitively expensive for realistic systems. For a computationally cheaper approach, one might consider coupling time domain density functional theory (TD-DFT) [100] computations with Maxwell equation solvers. Although both of these techniques are well developed, coupling them on 3D geometrically complicated structures is still a challenging problem.

Application to experimental set-ups

In several applications where nanostructures are used, such as molecular spectroscopy, numerical methods might be required to simulate scenarios where a layer of molecules is located between two nanostructures [81]. In such cases, contributions of molecules to the (effective) permittivity should be accounted for by the DFT computations. This can be done by introducing the layer of molecules in the gap of the super lattice.

All the application examples, which are considered in this thesis, use plane waves to excite the structures under analysis. Even though plane wave excitation is a good approximation to many sources used in experiments, other excitation types should be implemented to be able to account for a broader range of experimental set-ups. One example of these set-ups is electron energy loss spectroscopy (EELS) [101]. The EELS uses an electron with constant high speed as an excitation source. Electromagnetic fields generated by this electron path should be computed and used as incident fields for the TD-PMCHWT-SIE solver. Frequency domain counterpart of this excitation has already been implemented in FD-SIE solver [102].

REFERENCES

[1] S. A. Maier, *Plasmonics: Fundamentals and Applications.* Springer, 2007.

[2] J. N. Anker, W. P. Hall, O. Lyandres, N. C. Shah, J. Zhao, and R. P. V. Duyne, "Biosensing with plasmonic nanosensors," *Nat. Mater.*, vol. 7, pp. 442–453, 2008.

[3] D. J. de Aberasturi, A. B. Serrano-Montes, and L. M. Liz-Marzán, "Modern applications of plasmonic nanoparticles: From energy to health," *Adv. Opt. Mater.*, vol. 3, no. 5, pp. 602–617, 2015.

[4] J. Smajic, C. Hafner, L. Raguin, K. Tavzarashvili, and M. Mishrikey, "Comparison of numerical methods for the analysis of plasmonic structures," *J. Comput. Theor. Nanosci.*, vol. 6, no. 3, pp. 763–774, 2009.

[5] J. Zuloaga, E. Prodan, and P. Nordlander, "Quantum description of the plasmon resonances of a nanoparticle dimer," *Nano Lett.*, vol. 9, no. 2, pp. 887–891, 2009.

[6] R. Esteban, A. G. Borisov, P. Nordlander, and J. Aizpurua, "Bridging quantum and classical plasmonics with a quantum-corrected model," *Nat. Commun.*, vol. 3, p. 825, 2012.

[7] I. E. Uysal, H. A. Ülkü, and H. Bağci, "Transient analysis of electromagnetic wave interactions on plasmonic nanostructures using a surface integral equation solver," *J. Opt. Soc. Am. A*, vol. 33, no. 9, pp. 1747–1759, Sep 2016. [Online]. Available: http://josaa.osa.org/abstract.cfm?URI=josaa-33-9-1747

[8] K. Schwarz, P. Blaha, and G. Madsen, "Electronic structure calculations of solids using the WIEN2k package for material sciences," *Comput. Phys. Commun.*, vol. 147, no. 1, pp. 71–76, 2002.

[9] C. Ambrosch-Draxl and J. O. Sofo, "Linear optical properties of solids within the full-potential linearized augmented planewave method," *Comput. Phys. Commun.*, vol. 175, no. 1, pp. 1–14, 2006.

[10] A. Taflove and S. C. Hagness, *Computational Electrodynamics.* Artech House, 2005.

[11] P. G. Petropoulos, "Stability and phase error analysis of FD-TD in dispersive dielectrics," *IEEE Trans. Antennas Propag.*, vol. 42, 1994.

[12] J.-M. Jin, *The finite element method in electromagnetics*. John Wiley & Sons, 2014.

[13] S. Gedney and U. Navsariwala, "An unconditionally stable finite element time-domain solution of the vector wave equation," *IEEE Microw. Guided Wave Lett.*, vol. 5, no. 10, pp. 332–334, Oct 1995.

[14] R. F. Harrington, "Boundary integral formulations for homogeneous material bodies," *J. Electromagn. Waves Appl.*, vol. 3, 1989.

[15] A. M. Kern and O. J. Martin, "Surface integral formulation for 3D simulations of plasmonic and high permittivity nanostructures," *J. Opt. Soc. Am. A*, vol. 26, no. 4, pp. 732–740, 2009.

[16] M. Araújo, J. Taboada, J. Rivero, D. Solís, and F. Obelleiro, "Solution of large-scale plasmonic problems with the multilevel fast multipole algorithm," *Opt. Lett.*, vol. 37, no. 3, pp. 416–418, 2012.

[17] M. Araújo, J. Taboada, D. Solís, J. Rivero, L. Landesa, and F. Obelleiro, "Comparison of surface integral equation formulations for electromagnetic analysis of plasmonic nanoscatterers," *Opt. Express*, vol. 20, no. 8, pp. 9161–9171, 2012.

[18] B. Gallinet, A. M. Kern, and O. J. Martin, "Accurate and versatile modeling of electromagnetic scattering on periodic nanostructures with a surface integral approach," *J. Opt. Soc. Am. A*, vol. 27, no. 10, pp. 2261–2271, 2010.

[19] J. M. Taboada, J. Rivero, F. Obelleiro, M. G. Araújo, and L. Landesa, "Method-of-moments formulation for the analysis of plasmonic nano-optical antennas," *J. Opt. Soc. Am. A*, vol. 28, no. 7, pp. 1341–1348, 2011.

[20] J. H. Greene and A. Taflove, "General vector auxiliary differential equation finite-difference time-domain method for nonlinear optics," *Opt. Express*, vol. 14, no. 18, pp. 8305–8310, 2006.

[21] W. Chew, *Waves and Fields in Inhomogenous Media*, ser. IEEE Press Series on Electromagnetic Wave Theory. Wiley, 1999.

[22] D. Vechinski, S. M. Rao *et al.*, "Transient scattering from two-dimensional dielectric cylinders of arbitrary shape," *IEEE Trans. Antennas Propag.*, vol. 40, no. 9, pp. 1054–1060, 1992.

[23] G. Manara, A. Monorchio, and R. Reggiannini, "A space-time discretization criterion for a stable time-marching solution of the electric field integral equation," *IEEE Trans. Antennas Propag.*, vol. 45, no. 3, pp. 527–532, Mar. 1997.

[24] H. Bagci, A. Yilmaz, J.-M. Jin, and E. Michielssen, "Fast and rigorous analysis of EMC/EMI phenomena on electrically large and complex cable-loaded structures," *IEEE Trans. Electromagn. Compat.*, vol. 49, no. 2, pp. 361–381, May 2007.

[25] A. Yilmaz, D. S. Weile, B. Shanker, J.-M. Jin, and E. Michielssen, "Fast analysis of transient scattering in lossy media," *IEEE Antennas Wireless Propag. Lett.*, vol. 1, no. 1, pp. 14–17, 2002.

[26] X. Wang and D. S. Weile, "Electromagnetic scattering from dispersive dielectric scatterers using the finite difference delay modeling method," *IEEE Trans. Antennas Propag.*, vol. 58, no. 5, pp. 1720–1730, 2010.

[27] C. Lubich, "Convolution quadrature and discretized operational calculus. I," *Numerische Mathematik*, vol. 52, no. 2, pp. 129–145, 1988.

[28] A. Karlsson and S. Rikte, "Time-domain theory of forerunners," *J. Opt. Soc. Am. A*, vol. 15, no. 2, pp. 487–502, 1998.

[29] P.-L. Jiang and E. Michielssen, "Multilevel plane wave time domain-enhanced mot solver for analyzing electromagnetic scattering from objects residing in lossy media," in *IEEE Int. Symp. Antennas Propag.*, vol. 3B, July 2005, pp. 447–450.

[30] H. Bagci, A. Yilmaz, and E. Michielssen, "An FFT-accelerated time-domain multiconductor transmission line simulator," *IEEE Trans. Electromagn. Compat.*, vol. 52, no. 1, pp. 199–214, Feb. 2010.

[31] X. Wang and D. S. Weile, "Implicit Runge-Kutta methods for the discretization of time domain integral equations," *IEEE Trans. Antennas Propag.*, vol. 59, no. 12, pp. 4651–4663, 2011.

[32] A. E. Yilmaz, J.-M. Jin, and E. Michielssen, "Time domain adaptive integral method for surface integral equations," *IEEE Trans. Antennas Propag.*, vol. 52, no. 10, pp. 2692–2708, Oct. 2004.

[33] H. Bagci, A. Yilmaz, V. Lomakin, and E. Michielssen, "Fast solution of mixed-potential time-domain integral equations for half-space environments," *IEEE Trans. Geosci. Remote Sens.*, vol. 43, no. 2, pp. 269–279, Feb. 2005.

[34] C. Lubich and A. Ostermann, "Linearly implicit time discretization of non-linear parabolic equations," *IMA Journal of Numerical Analysis*, vol. 15, no. 4, pp. 555–583, 1995.

[35] J. Putnam and L. Medgyesi-Mitschang, "Combined field integral equation formulation for inhomogeneous two and three-dimensional bodies: the junction problem," *IEEE Trans. Antennas Propag.*, vol. 39, no. 5, pp. 667–672, May 1991.

[36] K. Donepudi, J.-M. Jin, and W. C. Chew, "A higher order multilevel fast multipole algorithm for scattering from mixed conducting/dielectric bodies," *IEEE Trans. Antennas Propag.*, vol. 51, no. 10, pp. 2814–2821, Oct. 2003.

[37] U. Hohenester, "Quantum corrected model for plasmonic nanoparticles: A boundary element method implementation," *Phys. Rev. B*, vol. 91, p. 205436, May 2015. [Online]. Available: http://link.aps.org/doi/10.1103/PhysRevB.91.205436

[38] E. Schlemmer, W. Rucker, and K. Richter, "Boundary element computations of 3D transient scattering from lossy dielectric objects," *IEEE Trans. Magn.*, vol. 29, no. 2, pp. 1524–1527, Mar. 1993.

[39] C. Yang and V. Jandhyala, "Modeling of lossy multiregion substrates in microelectronic circuits using time-domain surface integral equations," *Microwave Opt. Technol. Lett.*, vol. 47, no. 1, pp. 68–73, 2005. [Online]. Available: http://dx.doi.org/10.1002/mop.21084

[40] S. Rao, D. Wilton, and A. Glisson, "Electromagnetic scattering by surfaces of arbitrary shape," *IEEE Trans. Antennas Propag.*, vol. 30, no. 3, pp. 409–418, May 1982.

[41] B. Shanker, A. A. Ergin, and E. Michielssen, "Plane-wave-time-domain-enhanced marching-on-in-time scheme for analyzing scattering from homogeneous dielectric structures," *J. Opt. Soc. Am. A*, vol. 19, no. 4, pp. 716–726, Apr. 2002.

[42] P. M. Morse and H. Feshbach, *Methods of Theoretical Physics*. New York: McGraw-Hill, 1953.

[43] M. Vikram, A. Baczewski, B. Shanker, and L. Kempel, "Accelerated cartesian expansion (ACE) based framework for the rapid evaluation of diffusion, lossy wave, and Klein-Gordon potentials," *Journal of Comput.*

Phys., vol. 229, no. 24, pp. 9119 – 9134, 2010. [Online]. Available: http://www.sciencedirect.com/science/article/pii/S0021999110004729

[44] P.-L. Jiang and E. Michielssen, "Temporal acceleration of time-domain integral-equation solvers for electromagnetic scattering from objects residing in lossy media," *Microwave Opt. Technol. Lett.*, vol. 44, no. 3, pp. 223–230, 2005. [Online]. Available: http://dx.doi.org/10.1002/mop.20595

[45] J. Bor, O. Lafond, H. Merlet, P. Le Bars, and M. Himdi, "Foam based Luneburg lens antenna at 60 GHz," *Prog. Electromagn. Res. Lett.*, vol. 44, pp. 1–7, 2014.

[46] S. I. Bozhevolnyi, V. S. Volkov, E. Devaux, J.-Y. Laluet, and T. W. Ebbesen, "Channel plasmon subwavelength waveguide components including interferometers and ring resonators," *Nature*, vol. 440, no. 7083, pp. 508–511, 2006.

[47] C. Oubre and P. Nordlander, "Optical properties of metallodielectric nanostructures calculated using the finite difference time domain method," *J. Phys. Chem. B*, vol. 108, no. 46, pp. 17 740–17 747, 2004.

[48] A. Vial, A.-S. Grimault, D. Macías, D. Barchiesi, and M. L. de La Chapelle, "Improved analytical fit of gold dispersion: Application to the modeling of extinction spectra with a finite-difference time-domain method," *Phys. Rev. B*, vol. 71, no. 8, p. 085416, 2005.

[49] F. Hao and P. Nordlander, "Efficient dielectric function for FDTD simulation of the optical properties of silver and gold nanoparticles," *Chem. Phys. Lett.*, vol. 446, no. 1, pp. 115–118, 2007.

[50] Y. Hu, S. J. Noelck, and R. A. Drezek, "Symmetry breaking in gold- silica- gold multilayer nanoshells," *ACS Nano*, vol. 4, no. 3, pp. 1521–1528, 2010.

[51] K. L. Kelly, E. Coronado, L. L. Zhao, and G. C. Schatz, "The optical properties of metal nanoparticles: the influence of size, shape, and dielectric environment," *J. Phys. Chem. B*, vol. 107, no. 3, pp. 668–677, 2003.

[52] K. Sirenko, V. Pazynin, Y. K. Sirenko, and H. Bagci, "An FFT-accelerated FDTD scheme with exact absorbing conditions for characterizing axially symmetric resonant structures," *Prog. Electromagn. Res.*, vol. 111, pp. 331–364, 2011.

[53] A. A. Ergin, B. Shanker, and E. Michielssen, "The plane-wave time-domain algorithm for the fast analysis of transient wave phenomena," *IEEE Trans. Antennas Propag.*, vol. 41, no. 4, pp. 39–52, Sep. 1999.

[54] B. Shanker, A. A. Ergin, M. Lu, and E. Michielssen, "Fast analysis of transient electromagnetic scattering phenomena using the multilevel plane wave time domain algorithm," *IEEE Trans. Antennas Propag.*, vol. 51, no. 3, pp. 628–641, Mar. 2003.

[55] B. Shanker, M. Lu, J. Yuan, and E. Michielssen, "Time domain integral equation analysis of scattering from composite bodies via exact evaluation of radiation fields," *IEEE Trans. Antennas Propag.*, vol. 57, no. 5, pp. 1506–1520, May 2009.

[56] I. Uysal, H. Ulku, and H. Bagci, "MOT solution of the PMCHWT equation for analyzing transient scattering from conductive dielectrics," *IEEE Antennas Wireless Propag. Lett.*, vol. 14, pp. 507–510, 2015.

[57] B. Gustavsen and A. Semlyen, "Rational approximation of frequency domain responses by vector fitting," *IEEE Trans. Power Del.*, vol. 14, no. 3, pp. 1052–1061, 1999.

[58] B. Gustavsen, "Improving the pole relocating properties of vector fitting," *IEEE Trans. Power Del.*, vol. 21, no. 3, pp. 1587–1592, 2006.

[59] D. Deschrijver, M. Mrozowski, T. Dhaene, and D. De Zutter, "Macromodeling of multiport systems using a fast implementation of the vector fitting method," *IEEE Microw. Wirel. Compon. Lett.*, vol. 18, no. 6, pp. 383–385, 2008.

[60] P. B. Johnson and R.-W. Christy, "Optical constants of the noble metals," *Phys. Rev. B*, vol. 6, no. 12, p. 4370, 1972.

[61] E. D. Palik, *Handbook of Optical Constants of Solids*. Academic Press, 1998, vol. 3.

[62] S. Rao, *Time Domain Electromagnetics*. Elsevier Science, 1999.

[63] D. Wilton, S. Rao, A. Glisson, D. Schaubert, O. Al-Bundak, and C. Butler, "Potential integrals for uniform and linear source distributions on polygonal and polyhedral domains," *IEEE Trans. Antennas Propag.*, vol. 32, no. 3, pp. 276–281, Mar. 1984.

[64] H. A. Ulku and A. A. Ergin, "Analytical evaluation of transient magnetic fields due to RWG current bases," *IEEE Trans. Antennas Propag.*, vol. 55, no. 12, pp. 3565–3575, Dec. 2007.

[65] ——, "On the singularity of the closed-form expression of the magnetic field in time domain," *IEEE Trans. Antennas Propag.*, vol. 59, no. 2, pp. 691–694, Feb. 2011.

[66] ——, "Application of analytical retarded-time potential expressions to the solution of time domain integral equations," *IEEE Trans. Antennas Propag.*, vol. 59, no. 11, pp. 4123–4131, Nov. 2011.

[67] M. I. Mishchenko, L. D. Travis, and A. A. Lacis, *Scattering, Absorption, and Emission of Light by Small Particles*. Cambridge University Press, 2002.

[68] Z. Mei, T. K. Sarkar, and M. Salazar-Palma, "A study of negative permittivity and permeability for small sphere," *IEEE Antennas Wireless Propag. Lett.*, vol. 12, pp. 1228–1231, 2013.

[69] C. Forestiere, G. Iadarola, G. Rubinacci, A. Tamburrino, L. Dal Negro, and G. Miano, "Surface integral formulations for the design of plasmonic nanostructures," *J. Opt. Soc. Am. A*, vol. 29, no. 11, pp. 2314–2327, 2012.

[70] B. T. Draine and P. J. Flatau, "Discrete-dipole approximation for scattering calculations," *J. Opt. Soc. Am. A*, vol. 11, no. 4, pp. 1491–1499, Apr. 1994.

[71] E. R. Encina and E. A. Coronado, "Plasmon coupling in silver nanosphere pairs," *J. Phys. Chem. C*, vol. 114, no. 9, pp. 3918–3923, 2010.

[72] M. Amin and H. Bağcı, "Scattering properties of vein induced localized surface plasmon resonances on a gold disk," in *High Capacity Optical Networks and Enabling Technologies (HONET), 2011*. IEEE, 2011, pp. 237–240.

[73] M. S. Tame, K. McEnery, Ş. Özdemir, J. Lee, S. Maier, and M. Kim, "Quantum plasmonics," *Nat. Phys.*, vol. 9, no. 6, pp. 329–340, Nov. 2013.

[74] K. Kneipp, H. Kneipp, and J. Kneipp, "Probing plasmonic nanostructures by photons and electrons," *Chem. Sci.*, vol. 6, no. 5, pp. 2721–2726, 2015.

[75] I. Romero, J. Aizpurua, G. W. Bryant, and F. J. G. de Abajo, "Plasmons in nearly touching metallic nanoparticles: singular response in the limit of touching dimers," *Opt. Express*, vol. 14, no. 21, pp. 9988–9999, Oct 2006. [Online]. Available: http://www.opticsexpress.org/abstract.cfm?URI=oe-14-21-9988

[76] R. Esteban, A. Zugarramurdi, P. Zhang, P. Nordlander, F. J. Garcia-Vidal, A. G. Borisov, and J. Aizpurua, "A classical treatment of optical tunneling in plasmonic gaps: extending the quantum corrected model to practical situations," *Faraday Discuss.*, vol. 178, pp. 151–183, 2015. [Online]. Available: http://dx.doi.org/10.1039/C4FD00196F

[77] K. J. Savage, M. M. Hawkeye, R. Esteban, A. G. Borisov, J. Aizpurua, and J. J. Baumberg, "Revealing the quantum regime in tunnelling plasmonics," *Nature*, vol. 491, no. 7425, pp. 574–577, 2012.

[78] J. A. Scholl, A. García-Etxarri, A. L. Koh, and J. A. Dionne, "Observation of quantum tunneling between two plasmonic nanoparticles," *Nano Lett.*, vol. 13, no. 2, pp. 564–569, 2013.

[79] S. Kadkhodazadeh, J. B. Wagner, H. Kneipp, and K. Kneipp, "Coexistence of classical and quantum plasmonics in large plasmonic structures with subnanometer gaps," *Appl. Phys. Lett.*, vol. 103, no. 8, 2013. [Online]. Available: http://scitation.aip.org/content/aip/journal/apl/103/8/10.1063/1.4819163

[80] W. Zhu and K. B. Crozier, "Quantum mechanical limit to plasmonic enhancement as observed by surface-enhanced raman scattering," *Nature Commun.*, vol. 5, 2014.

[81] S. F. Tan, L. Wu, J. K. Yang, P. Bai, M. Bosman, and C. A. Nijhuis, "Quantum plasmon resonances controlled by molecular tunnel junctions," *Science*, vol. 343, no. 6178, pp. 1496–1499, 2014. [Online]. Available: http://science.sciencemag.org/content/343/6178/1496

[82] H. Jung, H. Cha, D. Lee, and S. Yoon, "Bridging the nanogap with light: continuous tuning of plasmon coupling between gold nanoparticles," *ACS Nano*, vol. 9, no. 12, pp. 12 292–12 300, 2015.

[83] H. Cha, D. Lee, J. H. Yoon, and S. Yoon, "Plasmon coupling between silver nanoparticles: Transition from the classical to the quantum regime," *J. Colloid Interface Sci.*, vol. 464, pp. 18 – 24, 2016. [Online]. Available: http://www.sciencedirect.com/science/article/pii/S0021979715303192

[84] L. Wu, H. Duan, P. Bai, M. Bosman, J. K. Yang, and E. Li, "Fowler–Nordheim tunneling induced charge transfer plasmons between nearly touching nanoparticles," *ACS Nano*, vol. 7, no. 1, pp. 707–716, 2012.

[85] P. Zhang, J. Feist, A. Rubio, P. García-González, and F. J. García-Vidal, "*Ab initio* nanoplasmonics: The impact of atomic structure," *Phys. Rev. B*, vol. 90, p. 161407, Oct 2014. [Online]. Available: http://link.aps.org/doi/10.1103/PhysRevB.90.161407

[86] P. Hohenberg and W. Kohn, "Inhomogeneous electron gas," *Phys. Rev.*, vol. 136, no. 3B, p. B864, 1964.

[87] W. Kohn and L. J. Sham, "Self-consistent equations including exchange and correlation effects," *Phys. Rev.*, vol. 140, no. 4A, p. A1133, 1965.

[88] W. S. Werner, K. Glantschnig, and C. Ambrosch-Draxl, "Optical constants and inelastic electron-scattering data for 17 elemental metals," *J. Phys. Chem. Ref. Data*, vol. 38, no. 4, pp. 1013–1092, 2009.

[89] S. Cottenier, "Density functional theory and the family of (L) APW-methods: a step-by-step introduction," *Instituut voor Kern-en Stralingsfysica, KU Leuven, Belgium*, vol. 4, no. 0, p. 41, 2002. [Online]. Available: http://www.wien2k.at/reguser/textbooks

[90] P. Blaha, K. Schwarz, P. Sorantin, and S. Trickey, "Full-potential, linearized augmented plane wave programs for crystalline systems," *Comput. Phys. Commun.*, vol. 59, no. 2, pp. 399–415, 1990.

[91] J. P. Perdew, K. Burke, and M. Ernzerhof, "Generalized gradient approximation made simple," *Phys. Rev. Lett.*, vol. 77, pp. 3865–3868, Oct 1996. [Online]. Available: http://link.aps.org/doi/10.1103/PhysRevLett.77.3865

[92] D. Rocca, D. Lu, and G. Galli, "Ab initio calculations of optical absorption spectra: Solution of the Bethe–Salpeter equation within density matrix perturbation theory," *J. Chem. Phys.*, vol. 133, no. 16, 2010. [Online]. Available: http://scitation.aip.org/content/aip/journal/jcp/133/16/10.1063/1.3494540

[93] H. Ehrenreich and M. H. Cohen, "Self-consistent field approach to the many-electron problem," *Phys. Rev.*, vol. 115, pp. 786–790, Aug 1959. [Online]. Available: http://link.aps.org/doi/10.1103/PhysRev.115.786

[94] F. Wooten, *Optical Properties of Solids*. Academic Press, New York, 1972.

[95] L. Brekhovskikh, *Waves in Layered Media*, ser. Applied Mathematics and Mechanics. Academic Press, 1980, vol. 16.

[96] P. Yla-Oijala, M. Taskinen, and J. Sarvas, "Surface integral equation method for general composite metallic and dielectric structures with junctions," *Prog. Electromagn. Res.*, vol. 52, pp. 81–108, 2005.

[97] A. T. Fromhold, *Quantum Mechanics for Applied Physics and Engineering*. Academic Press, New York, 1981.

[98] R. W. Ziolkowski, J. M. Arnold, and D. M. Gogny, "Ultrafast pulse interactions with two-level atoms," *Phys. Rev. A*, vol. 52, pp. 3082–3094, Oct 1995. [Online]. Available: http://link.aps.org/doi/10.1103/PhysRevA.52.3082

[99] K. Lopata and D. Neuhauser, "Nonlinear nanopolaritonics: Finite-difference time-domain Maxwell Schrödinger simulation of molecule-assisted plasmon

transfer," *J. Chem. Phys.*, vol. 131, no. 1, 2009. [Online]. Available: http://scitation.aip.org/content/aip/journal/jcp/131/1/10.1063/1.3167407

[100] H. Chen, J. M. McMahon, M. A. Ratner, and G. C. Schatz, "Classical electrodynamics coupled to quantum mechanics for calculation of molecular optical properties: a RT-TDDFT/FDTD approach," *J. Phys. Chem. C*, vol. 114, no. 34, pp. 14 384–14 392, 2010. [Online]. Available: http://dx.doi.org/10.1021/jp1043392

[101] F. G. De Abajo, "Optical excitations in electron microscopy," *Rev. Mod. Phys.*, vol. 82, no. 1, p. 209, 2010.

[102] U. Hohenester, "Simulating electron energy loss spectroscopy with the MNPBEM toolbox," *Comput. Phys. Commun.*, vol. 185, no. 3, pp. 1177–1187, 2014.

APPENDICES

A Appendix A: FRVF Scheme

This section briefly describes the fundamental idea behind the FRVF scheme. The details can be found in [57–59]. Let $F(\omega)$ represent a function defined in the frequency domain. FRVF approximates $F(\omega)$ as a sum of rational functions:

$$F(\omega) \approx \mathrm{j}\omega f + d + \sum_{m=1}^{N} \frac{b_m}{\mathrm{j}\omega + a_m}. \tag{A.1}$$

Here, N is termed fitting order, d and f are optional parameters, and a_m and b_m are poles and residues, respectively. While d and f are real or can be forced to be zero, and a_m and b_m are either real or have to come in complex conjugate pairs.

The FRVF scheme is iteratively executed. Each iteration has two stages: identification of poles and residues of the right hand side of Eq. (A.1). First, poles are identified as described next. Let $S(\omega)$ and $S(\omega)F(\omega)$ represent two auxiliary functions:

$$S(\omega) = 1 + \sum_{m=1}^{N} \frac{b_m^{\mathrm{S}}}{\mathrm{j}\omega + \tilde{a}_m}, \tag{A.2}$$

$$S(\omega)F(\omega) \approx \mathrm{j}\omega f^{\mathrm{SF}} + d^{\mathrm{SF}} + \sum_{m=1}^{N} \frac{b_m^{\mathrm{SF}}}{\mathrm{j}\omega + \tilde{a}_m}. \tag{A.3}$$

Here, $\tilde{a}_m$ are "guessed" poles of $S(\omega)$ and $S(\omega)F(\omega)$ for the given iteration. Multiplying Eq. (A.2) with $F(\omega)$ and equating the resulting expression to the right hand side of Eq. (A.3), and evaluating the final equation at frequency samples ω_i, $i = 1, ..., N_{\mathrm{samp}}$,

where $N < N_{\text{samp}}$, yield an overdetermined system

$$\bar{\bar{A}}\bar{X} = \bar{Y}. \tag{A.4}$$

Here, $[\bar{\bar{A}}]_i = \left[\frac{1}{\mathrm{j}\omega_i+\tilde{a}_1} \dots \frac{1}{\mathrm{j}\omega_i+\tilde{a}_N} \quad 1 \quad \mathrm{j}\omega_i \quad \frac{-F(\omega_i)}{\mathrm{j}\omega_i+\tilde{a}_1} \dots \frac{-F(\omega_i)}{\mathrm{j}\omega_i+\tilde{a}_N}\right]$ represents the ith row of $\bar{\bar{A}}$, $\bar{X} = \left[b_1^{\text{SF}} \dots b_N^{\text{SF}} \quad d^{\text{SF}} \quad f^{\text{SF}} \quad b_1^{\text{S}} \dots b_N^{\text{S}}\right]^T$ is the unknown vector, and $\{\bar{Y}\}_i = F(\omega_i)$. Unknown $\bar{X}$ is obtained by solving Eq. (A.4) in the least squares sense. One can show that zeros of the $S(\omega)$ are equal to the poles of $F(\omega)$ by rewriting Eqs. (A.1)-(A.3) in terms of sum of partial fractions [57]. These zeros are equal to the eigenvalues of the matrix $\bar{\bar{D}} - \bar{H}\bar{B}^T$ where $\bar{\bar{D}}$ is a diagonal matrix with entries $\{\bar{\bar{D}}\}_{m,m} = \tilde{a}_m$, $\{\bar{H}\}_m = 1$, and $\{\bar{B}\}_m = b_m^{\text{S}}$. This completes the identification of the poles of the right hand side of Eq. (A.1) for the given iteration. Once these poles are known, the residues are identified as described next. Eq. (A.1) is evaluated at ω_i, $i = 1, ..., N_{\text{samp}}$ yielding an overdetermined system as in Eq. (A.4), where now $[\bar{\bar{A}}]_i = \left[\frac{1}{\mathrm{j}\omega_i+a_1} \dots \frac{1}{\mathrm{j}\omega_i+a_N} \quad 1 \quad \mathrm{j}\omega_i\right]$ and $\bar{X} = [b_1 \dots b_N \quad d \quad f]^T$. Solving this system in the least squares sense yields the residues of the right hand side of Eq. (A.1) for the given iteration and completes the iteration. Poles obtained in one iteration are used as an initial guess in the next one and the iterations are repeated until a pre-set level of accuracy is obtained, i.e., an accurate representation for $F(\omega)$ is obtained. Note that $e^{\mathrm{j}\omega t}$ convention is used here.

B Appendix B: List of papers

Journal papers

1. I. E. Uysal, H. A. Ülkü, and H. Bağcı, "MOT Solution of the PMCHWT Equation for Analyzing Transient Scattering from Conductive Dielectrics", *IEEE Antennas and Wireless Propag. Lett.*, vol. 14 , 2014.

2. I. E. Uysal, H. A. Ülkü, and H. Bağcı, "Transient analysis of electromagnetic wave interactions on plasmonic nanostructures using a surface integral equation solver," *J. Opt. Soc. Am. A*, vol. 33, no. 9, pp. 1747–1759, Sep 2016.

3. I. E. Uysal, H. A. Ülkü, M. Sajjad, N. Singh, U. Schwingenschlögl, and H. Bağcı, "Quantum Corrected Time Domain Surface Integral Equation Solver", *Opt. Express*, (submitted).

Conference papers and abstracts

1. I. E. Uysal, H. A. Ülkü, M. Sajjad, N. Singh, U. Schwingenschlögl, and H. Bağcı, "DFT-corrected Electromagnetic Analysis of Nanostructures", in *Antennas and Propagation USNC/URSI National Radio Science Meeting*, Fajardo, Puerto Rico, June 2016.

2. I. E. Uysal, H. A. Ülkü, and H. Bağcı, "Quantum-Corrected Plasmonic Field Analysis Using a Time Domain PMCHWT Integral Equation", in *Applied Computational Electromagnetics Society Conference*, Honolulu, Hawaii, March 2016.

3. I. E. Uysal, H. A. Ülkü, and H. Bağcı, "Transient analysis of plasmonic nanostructures using an MOT-PMCHWT solver", in *Antennas and Propagation USNC/URSI National Radio Science Meeting*, Vancouver, BC, Canada , July 2015.

4. I. E. Uysal, H. A. Ülkü, and H. Bağcı, "MOT Solution of the PMCHWT Equation for Analyzing Transient Scattering from Conductive Dielectrics", in *Antennas and Propagation USNC/URSI National Radio Science Meeting*, Vancouver, BC, Canada , July 2015.

5. I. E. Uysal, H. A. Ülkü, and H. Bağcı, "Analysis of transient plasmonic interactions using an MOT-PMCHWT integral equation solver", in *Antennas and Propagation USNC/URSI National Radio Science Meeting*, Memphis, TN, July 2014.

6. I. E. Uysal, H. A. Ülkü, and H. Bağcı, "MOT Solution of Time Domain PMCHWT Integral Equation for Lossy Dielectric Scatterers", in *Applied Computational Electromagnetics Society Conference*, Jacksonville, Florida, March 2014.

7. I. E. Uysal, H. A. Ülkü, and H. Bağcı, "A PMCHWT Surface Integral Equation Solver for Analyzing Transient Plasmonic Interactions", in *Progress In Electromagnetics Research Symposium*, Stockholm, Sweden, August 2013.